

CHAPTER 2

Description of the Reanalysis Systems

Chapter Leads:

Jonathon S. Wright (Tsinghua University, China)

Masatomo Fujiwara (Hokkaido University, Japan)

Craig Long (National Oceanic and Atmospheric Administration, USA)

Co-authors:

James Anstey (Environment & Climate Change Canada, University of Victoria, Canada)

Gilbert P. Compo (University of Colorado, USA)

Rossana Dragani (European Centre for Medium-Range Weather Forecasts, UK)

Wesley Ebisuzaki (National Oceanic and Atmospheric Administration, USA)

Yayoi Harada (Japan Meteorological Agency, Japan)

Chiaki Kobayashi (Japan Meteorological Agency, Japan)

Will McCarty (National Aeronautics and Space Administration, USA)

Andrea Molod (National Aeronautics and Space Administration, USA)

Kazutoshi Onogi (Japan Meteorological Agency, Japan)

Steven Pawson (National Aeronautics and Space Administration, USA)

Adrian Simmons (European Centre for Medium-Range Weather Forecasts, UK)

David Tan (European Centre for Medium-Range Weather Forecasts, UK)

Krzysztof Wargan (National Aeronautics and Space Administration, USA)

Jeffrey S. Whitaker (National Oceanic and Atmospheric Administration, USA)

Cheng-Zhi Zou (National Oceanic and Atmospheric Administration, USA)

29 **CHAPTER 2**
 30 **DESCRIPTION OF THE REANALYSIS SYSTEMS**
 31 **Contents**
 32

33	SUMMARY	2
34	2.1 INTRODUCTION	3
35	2.2 FORECAST MODELS	6
36	2.2.1 Summary of the basic information	6
37	2.2.2 Major physical parametrizations	10
38	2.2.3 Boundary and other specified conditions.....	17
39	2.2.3.1 Sea surface temperature and sea ice	18
40	2.2.3.2 Ozone.....	20
41	2.2.3.3 Aerosols.....	22
42	2.2.3.4 Carbon dioxide and other radiatively active gases.....	23
43	2.2.3.5 Solar cycle	24
44	2.3 ASSIMILATION SCHEMES	27
45	2.3.1 Basics of data assimilation.....	27
46	2.3.2 Data assimilation in reanalysis systems	31
47	2.4 OBSERVATIONAL DATA	34
48	2.4.1 Summary of the basic information	34
49	2.4.2 Summary of key upper air observations and known issues.....	45
50	2.4.2.1 Radiosonde data	47
51	2.4.2.2 Satellite data	49
52	2.4.2.3 Aircraft data.....	54
53	2.4.3 Water vapour.....	54
54	2.5 EXECUTION STREAMS.....	57
55	2.5.1 What is an "execution stream"?	57
56	2.5.2 Summary of stream execution.....	57
57	2.6 ARCHIVED DATA	61
58	ACKNOWLEDGMENTS	62
59	REFERENCES.....	63
60	APPENDIX A: LIST OF ACRONYMS	75
61	APPENDIX B: VERTICAL LEVELS OF THE MODELS.....	79
62		
63		
64		

65 SUMMARY

66 Information on key components of eleven global atmospheric reanalysis systems with output
67 data available in 2015 is summarized, including brief descriptions of the forecast models,
68 assimilation schemes, and observational data used in these systems. Details of the execution
69 streams and archived data products are also provided. Tables are used extensively to
70 facilitate comparison of different reanalysis systems, and are arranged so that readers
71 interested in one or more systems can easily find and compare relevant information. The
72 information in this chapter will be referred to in the interpretation of results presented in the
73 other chapters of this S-RIP report. This chapter is not intended to provide a complete
74 description of the reanalyses; readers requiring further details are encouraged to refer to the
75 cited literature and the online documentation provided for the reanalysis systems.

76

77 **2.1 INTRODUCTION**

78 An atmospheric reanalysis system consists of a global forecast model, input observations,
 79 and an assimilation scheme that blends input observations with short-range forecasts. These
 80 systems produce global atmospheric data that represents best estimates (analyses) of past
 81 atmospheric states. The information collected in these analyses is then propagated forward
 82 in time and space by subsequent forecasts. In this chapter, we provide summary descriptions
 83 of the key components of the eleven global atmospheric reanalysis systems listed in Table 2-
 84 1. Our descriptions of these systems are by necessity incomplete. Further details may be
 85 found in the cited literature, particularly the publications listed in Table 2-1, or in the
 86 technical documentation compiled and provided by the reanalysis centres. A list of the
 87 acronyms used in this chapter is provided in Appendix A.

88 We classify reanalysis systems according to their observational inputs and temporal
 89 coverage. The three classes of reanalysis systems include “full input” systems (which
 90 assimilate surface and upper-air conventional and satellite data), “conventional input”
 91 systems (which assimilate surface and upper air conventional data, but do not assimilate
 92 satellite data), and “surface input” systems (which assimilate surface data only). Some
 93 reanalysis centres also provide companion “AMIP-type” simulations, which do not
 94 assimilate any observational data and are constrained by applying observed sea surface
 95 temperatures, sea ice, and other boundary conditions on the atmospheric forecast model. We
 96 also broadly distinguish reanalyses of the “satellite era” (1979–present) and reanalyses that
 97 provide data for dates before January 1979, with the latter referred to as “extended”
 98 reanalyses.

100 Three reanalyses produced by ECMWF are considered: ERA-40, ERA-Interim, and ERA-
 101 20C. ERA-40 (Uppala et al., 2005) is an extended full input reanalysis covering 45 years
 102 from September 1957 through August 2002. No satellite data were assimilated for dates
 103 prior to January 1973; ERA-40 is therefore a conventional input reanalysis from September
 104 1957 through December 1972. ERA-40 represented an important improvement relative to
 105 the first generation of modern reanalysis systems and continues to be used in many studies
 106 that require long-term atmospheric data. ERA-Interim (Dee et al., 2011) is a full input
 107 reanalysis of the satellite era (1979–present) that applies several corrections and
 108 modifications to the system used for ERA-40. Major focus areas during the production of
 109 ERA-Interim included improving the representations of the hydrologic cycle and the
 110 stratospheric circulation relative to ERA-40, as well as improving the consistency of the
 111 reanalysis products in time. ERA-20C (Poli et al., 2016) is a surface input reanalysis of the
 112 twentieth century (1900–2010). ERA-20C directly assimilates only surface pressure and
 113 surface wind observations, and can therefore generate reanalyses of the atmospheric state
 114 that extend further backward in time. Data from ERA-20C extend up to 0.01 hPa, but the
 115 lack of upper-air observational constraints means that these data should be used with caution
 116 in the upper troposphere and above. We omit the earlier ECMWF reanalysis products FGGE
 117 (Bengtsson et al., 1982) and ERA-15 (Gibson et al., 1997).

119 Two reanalyses produced by JMA and cooperating institutions are considered: JRA-25 and
 120 JRA-55. JRA-25 (Onogi et al. 2007) was the first reanalysis produced using the JMA
 121 forecast model and data assimilation system, and was a joint effort by JMA and CRIEPI.
 122 This reanalysis originally covered 25 years from 1979 through 2004, and was extended an
 123 additional 10 years (through the end of January 2014) as JCDAS using an identical system.
 124 JRA-55 (Kobayashi et al., 2015) is a more recent reanalysis that extends from 1958 through

126 the present. JRA-55 is the first reanalysis system to apply a 4D-Var data assimilation
 127 scheme (see Section 2.3) to upper-air data during the pre-satellite era (ERA-20C has also
 128 used 4D-Var to assimilate surface observations during the pre-satellite era). Along with the
 129 JRA-55 reanalysis, JMA has provided two companion products: JRA-55C (Kobayashi et al.,
 130 2014), a reanalysis using only conventional (non-satellite) observations, and JRA-55AMIP,
 131 an ensemble of forecast model simulations without data assimilation. At the time of this
 132 writing, these companion products only extend through December 2012, although
 133 extensions to later dates are planned for both.
 134

135 Two reanalyses produced by NASA are considered: MERRA and MERRA-2. MERRA
 136 (Rienecker et al., 2011) was conceived by NASA GMAO as a reanalysis of the satellite era
 137 (starting in January 1979), with particular focus on leveraging the large amounts of data
 138 produced by NASA's Earth Observing System (EOS) satellite constellation and improving
 139 the representations of the water and energy cycles relative to earlier reanalyses. MERRA
 140 production was discontinued after February 2016. Motivated by the inability of the MERRA
 141 system to ingest some recent data types, GMAO has developed the follow-on reanalysis
 142 MERRA-2 (Bosilovich et al., 2015). MERRA-2, which covers 1980–present, includes
 143 substantial upgrades to the model (Molod et al., 2015) and changes to the data assimilation
 144 system and input data (McCarty et al., 2016). Several new data sources are used that were
 145 not assimilated by MERRA, including hyperspectral radiances from IASI and CrIS,
 146 microwave radiances from ATMS, MLS temperature and ozone profiles, and GNSS-RO
 147 bending angles. One significant and unique feature of MERRA-2 is the assimilation of
 148 aerosol optical depth observations (Randles et al., 2016), with analysed aerosols fed back to
 149 the forecast model radiation scheme. An earlier NASA reanalysis (Schubert et al., 1993;
 150 Schubert et al., 1995) covering 1980–1995 was produced by NASA's DAO (now GMAO)
 151 using the GEOS-1 data assimilation system; this reanalysis is no longer publicly available,
 152 and is not included in the SRIP intercomparison.
 153

154 Four reanalyses produced by NOAA/NCEP and cooperating organizations are considered:
 155 NCEP–NCAR R1, NCEP–DOE R2, CFSR/CFSv2, and NOAA–CIRES 20CR. NCEP–
 156 NCAR R1 (Kalnay et al., 1996; Kistler et al., 2001) was the first modern reanalysis system
 157 with extended temporal coverage (1948–present). This system, which uses a modified 1995
 158 version of the NCEP forecast model, remains in widespread use. The NCEP–DOE R2
 159 covers the satellite era (1979–present) using essentially the same model structure, but
 160 corrects some important errors and limitations (Kanamitsu et al., 2002). More recently,
 161 NCEP has produced CFSR using a 2007 version of the NCEP forecast model (Saha et al.,
 162 2010). CFSR contains a number of improvements relative to R1 and R2 in both the forecast
 163 model and data assimilation system, including higher horizontal and vertical resolutions,
 164 more sophisticated model physics, and the ability to assimilate satellite radiances directly
 165 (rather than temperature retrievals). CFSR is also the first coupled global reanalysis of the
 166 atmosphere–ocean–sea ice system. Production of CFSR was transitioned to a newer version
 167 of the NCEP data assimilation system (CFSv2; Saha et al., 2014) on 1 January 2011. This
 168 transition from CFSR to CFSv2 should not be confused with the transfer of CFSv2
 169 production from NCEP EMC to NCEP operations, which occurred at the start of April 2011.
 170 The data assimilation system used in CFSv2 has a different horizontal resolution and
 171 includes minor changes to physical parametrizations, but is intended to serve as a
 172 continuation of CFSR. We therefore treat CFSR/CFSv2 as a paired system, including brief
 173 descriptions of differences between the original and updated systems where relevant.
 174 NOAA–CIRES 20CR (Compo et al., 2011) is the first reanalysis to span more than 100
 175 years. Like ERA-20C, 20CR is a surface input reanalysis. Unlike ERA-20C, which uses a

176 4D-Var approach to assimilate both surface pressure and surface winds, 20CR uses an EnKF
 177 approach (see Section 2.3) and assimilates only surface pressure. The forecast model used in
 178 20CR is similar in many ways to that used in CFSR, but with much coarser vertical and
 179 horizontal grids. Because of its relatively coarse vertical resolution (see Appendix B) and
 180 the lack of direct observational inputs in the upper atmosphere, output from 20CR should be
 181 used with care, particularly in the upper troposphere and above.
 182

183 The influence of observational data on reanalysis products differs by variable (see, e.g., the
 184 variable classification proposed by Kistler et al., 2001). Atmospheric temperatures,
 185 horizontal winds, and geopotential heights are strongly influenced by the assimilation of
 186 observational data even in earlier reanalysis systems, although these variables may be
 187 determined mainly by the forecast model in regions or periods where observations are sparse.
 188 Observational constraints on tropospheric water vapour are weaker but still influential, and
 189 some recent reanalysis systems assimilate data that establish constraints on ozone, total
 190 water, precipitation, and/or aerosol optical depth. Variables that are largely determined by
 191 the forecast model or surface boundary conditions (such as surface fluxes and tendency
 192 terms for heat, moisture, and momentum) are considered less reliable and should be used
 193 with caution and/or validated against independent estimates.
 194

195 The SPARC community has particular interest in upper tropospheric and stratospheric ozone
 196 and water vapour. This chapter briefly summarizes the treatment of these variables, with
 197 detailed intercomparisons deferred to Chapter 4. Many reanalysis systems simulate ozone
 198 using photochemistry schemes of varying complexity and assimilate satellite ozone
 199 retrievals during the period after 1979. Some reanalysis systems provide an ozone analysis
 200 but use a climatological ozone distribution for radiation calculations in the forecast model.
 201 Additional details regarding the treatment of ozone are provided in Table 2-9. Reanalysis
 202 estimates of stratospheric water vapour are rudimentary and often unreliable. Adjustments
 203 due to data assimilation are typically suppressed above a specified upper boundary that
 204 varies by reanalysis system, and are sometimes replaced by relaxation to a zonal mean
 205 climatology. Stratospheric air is dehydrated mainly at the tropical tropopause and
 206 transported and diffused from there, with few if any impacts from methane oxidation in the
 207 stratosphere (although some systems do include a representation of the effects of methane
 208 oxidation; see Table 2-18 for further details).
 209

210 Table 2-1. List of global atmospheric reanalysis systems considered in this report.

Reanalysis system	Reference	Description
ERA-40	Uppala et al. (2005)	Centre: ECMWF Coverage: September 1957 to August 2002
ERA-Interim	Dee et al. (2011)	Centre: ECMWF Coverage: January 1979 to present.
ERA-20C	Poli et al. (2016)	Centre: ECMWF Coverage: January 1900 to December 2010 Note: A companion ensemble of AMIP-style simulations (ERA-20CM; Hersbach et al., 2015) is also available.
JRA-25 / JCDAS	Onogi et al. (2007)	Centre: JMA and CRIEPI Coverage: January 1979 to January 2014 Note: January 2005 through January 2014 are from JCDAS, a real-time extension of JRA-25.
JRA-55	Kobayashi et al. (2015)	Centre: JMA

		Coverage: January 1958 to present Note: Two ancillary products are also available: JRA-55C (which assimilates only conventional observational data and covers November 1972 to December 2012; see Kobayashi et al., 2014) and JRA-55AMIP (which assimilates no observational data but uses the same boundary conditions as JRA-55).
MERRA	Rienecker et al. (2011)	Centre: NASA GMAO
MERRA-2	Bosilovich et al. (2015)	Coverage: January 1979 to February 2016 Centre: NASA GMAO
NCEP-NCAR R1	Kalnay et al. (1996); Kistler et al. (2001)	Coverage: January 1980 to present Centre: NOAA/NCEP and NCAR
NCEP-DOE R2	Kanamitsu et al. (2002)	Centre: NOAA/NCEP and the DOE AMIP-II project Coverage: January 1979 to present
CFSR / CFSv2	Saha et al. (2010) Saha et al. (2014)	Centre: NOAA/NCEP Coverage: January 1979 to present Note: Official data coverage by CFSR (CDAS-T382) extends through December 2010; production was migrated to the CFSv2 (CDAS-T574) analysis system starting from 1 January 2011. Although it has a different horizontal resolution (Table 2-2) and includes minor changes to physical parametrizations, CFSv2 can be considered as a continuation of CFSR for most purposes.
NOAA-CIRES 20CR v2	Compo et al. (2011)	Centre: NOAA and the University of Colorado CIRES Coverage: November 1869 to December 2012 Note: A new version covering 1851–2011 (20CR version 2c) has been completed and made available in 2015.

211

212

213

214 **2.2 FORECAST MODELS**215 **2.2.1 Summary of basic information**

216 Table 2-2 provides a summary of key information regarding the forecast models used in
 217 each reanalysis, including the analysis system, the horizontal grid, and the number of
 218 vertical levels. The information on horizontal grids provides only a rough idea of the finest
 219 horizontal scales represented by the models. We describe the horizontal grid structures of
 220 models that use spectral dynamical cores (e.g., Machenhauer, 1979) using two separate
 221 notations. All of the models considered here use spectral dynamical cores except for
 222 MERRA and MERRA-2. Regular Gaussian grids are denoted by F_n and T_k . F_n refers to a

regular Gaussian grid with $2n$ latitude bands and (in most cases) $4n$ longitude bands, while T_k indicates horizontal truncation at wave number k in the spectral dynamical core. The longitude grid spacing in a standard F_n regular Gaussian grid is $90^\circ/n$, so that the geographical distance between neighbouring grid cells in the east–west direction shrinks toward the poles. R1, R2, and 20CR use modified regular Gaussian grids with $4(n+1)$ longitude bands and longitude spacings of $90^\circ/(n+1)$. Linear reduced Gaussian grids (Hortal and Simmons, 1991; Courtier and Naughton, 1994) are denoted by N_n and T_{Lk} , where the latter again indicates truncation at horizontal wave number k . The number of latitude bands in the N_n reduced Gaussian grid is also $2n$, but the number of longitudes per latitude circle decreases from the equator (where it is $4n$) toward the poles. Longitude grid spacing in reduced Gaussian grids is therefore quasi-regular in distance rather than degrees (Table 2-2). More details on Gaussian grids are available at <https://software.ecmwf.int/wiki/display/FCST/Gaussian+grids> (accessed 28 August 2016). Unlike the other reanalysis systems discussed in this chapter, MERRA and MERRA-2 use regular latitude–longitude grids with finite volume dynamical cores (Lin, 2004).

Table 2-3 lists the model tops and describes special treatments applied in the uppermost layers of each model. Common special treatments include the use of a diffusive ‘sponge’ layer near the model top. Sponge layers are a concession to the finite ‘lid height’ that must be assumed in numerical models of the atmosphere, which is in reality unbounded at the top. The application of enhanced diffusion in a sponge layer damps upward propagating waves as they near the model top, thereby preventing unphysical reflection of wave energy at the model top that would in turn introduce unrealistic resonance in the model atmosphere (Lindzen et al., 1968). It is worth noting, however, that diabatic heating and momentum transfer associated with the absorption of wave energy by sponge layers and other simplified representations of momentum damping (such as Rayleigh friction) may still introduce spurious behaviour in model representations of middle atmospheric dynamics (Shepherd et al., 1996; Shepherd and Shaw, 2004). Most of the forecast models used by reanalysis systems include a sponge layer, but the formulation of this layer varies.

All of the reanalysis systems discussed in this chapter use hybrid $\sigma-p$ vertical coordinates (Simmons and Burridge, 1981), with the exception of NCEP-NCAR R1 and NCEP-DOE R2, which use σ vertical coordinates. The number of vertical levels ranges from 28 (R1, R2, and 20CR) to 91 (ERA-20C), and top levels range from 3 hPa (NCEP-NCAR R1 and NCEP-DOE R2) to 0.01 hPa (MERRA, MERRA-2, and ERA-20C). Figure 2-1 shows approximate vertical resolutions for the reanalysis systems in log-pressure altitude, assuming a scale height of 7 km and a surface pressure of 1000 hPa. A number of key differences are evident, including large discrepancies in the height of the top level (Figure 2-1a) and variations in vertical resolution through the upper troposphere and lower stratosphere (Figure 2-1b). These model grids differ from the isobaric levels on which many reanalysis products are provided. Vertical spacing associated with an example set of these isobaric levels (corresponding to ERA-40 and ERA-Interim) is included in Figure 2-1 for context. See Appendix B for lists of model levels and further details of the vertical grid.

Table 2-2. Basic details of the forecast models used in the reanalyses. Horizontal grid spacing is expressed in degrees for regular grids and in kilometres for reduced grids.

Reanalysis system	Model	Horizontal grid	Vertical grid
ERA-40	IFS Cycle 23r4 (2001)	N80: ~125 km (T _L 159)	60 (hybrid $\sigma-p$)

ERA-Interim	IFS Cycle 31r2 (2007)	N128: ~79 km (T _L 255)	60 (hybrid σ - p)
ERA-20C	IFS Cycle 38r1 (2012)	N80: ~125 km (T _L 159)	91 (hybrid σ - p)
JRA-25 / JCDAS	JMA GSM (2004)	F80: 1.125° (T106)	40 (hybrid σ - p)
JRA-55	JMA GSM (2009)	N160: ~55 km (T _L 319)	60 (hybrid σ - p)
MERRA	GEOS 5.0.2 (2008)	$\frac{1}{2}$ ° latitude, $\frac{2}{3}$ ° longitude	72 (hybrid σ - p)
MERRA-2	GEOS 5.12.4 (2015)	$\frac{1}{2}$ ° latitude, $\frac{5}{8}$ ° longitude	72 (hybrid σ - p)
NCEP-NCAR R1	NCEP MRF (1995)	F47: 1.875° (T62)	28 (σ)
NCEP-DOE R2	Modified MRF (1998)	F47: 1.875° (T62)	28 (σ)
CFSR	NCEP CFS (2007)	F288: 0.3125° (T382)	64 (hybrid σ - p)
CFSv2	NCEP CFS (2011)	F440: 0.2045° (T574)	64 (hybrid σ - p)
NOAA-CIRES 20CR v2	NCEP GFS (2008)	F47: 1.875° (T62)	28 (hybrid σ - p)

270

271

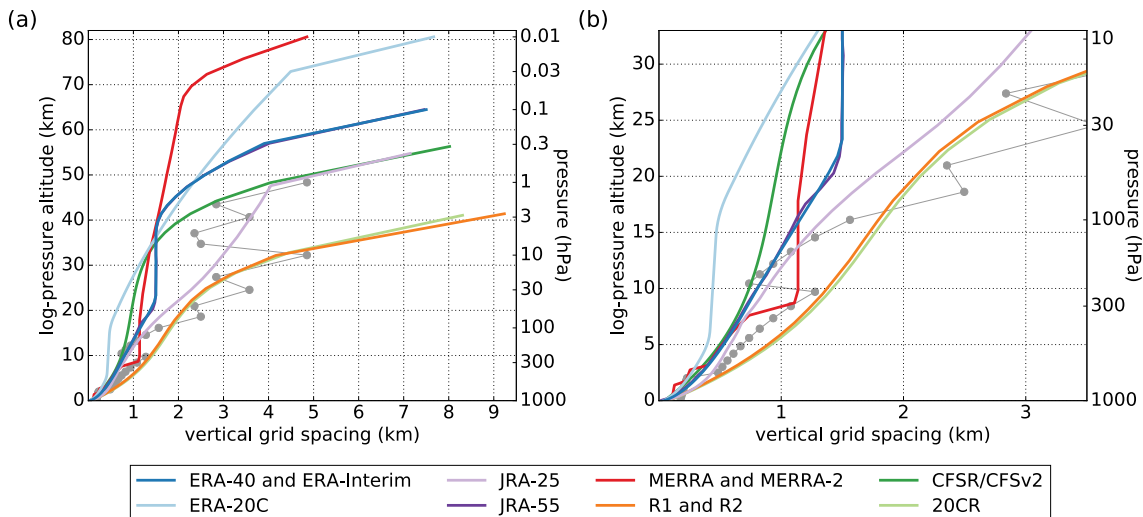
272

Table 2-3. Model top levels and special dynamical treatments applied in the uppermost model levels.

Reanalysis system	Top level	Special treatment of uppermost levels
ERA-40	0.1 hPa	A sponge layer is applied at pressures less than 10 hPa by adding an additional function to the horizontal diffusion terms. This function, which varies with wavenumber and model level, acts as an effective absorber of vertically-propagating gravity waves. Rayleigh friction is also implemented at pressures less than 10 hPa.
ERA-Interim	0.1 hPa	A sponge layer is applied at pressures less than 10 hPa by adding an additional function to the horizontal diffusion terms. This function, which varies with wavenumber and model level, acts as an effective absorber of vertically-propagating gravity waves. Rayleigh friction is also implemented at pressures less than 10 hPa.
ERA-20C	0.01 hPa	A sponge layer is applied at pressures less than 10 hPa by adding an additional function to the horizontal diffusion terms. This function, which varies with wavenumber and model level, acts as an effective absorber of vertically-propagating gravity waves. An additional first order ‘mesospheric’ sponge layer is implemented at pressures less than 1 hPa. As in ERA-40 and ERA-Interim, Rayleigh friction is still applied at pressures less than 10 hPa, but the coefficient is

		reduced in view of the inclusion of a non-orographic gravity wave drag parametrization (Table 2-6).
JRA-25 / JCDAS	0.4 hPa	A sponge layer is applied by gradually enhancing horizontal diffusion coefficients with increasing height at pressures less than 100 hPa. Rayleigh damping is applied to temperature deviations from the global average on each of the highest three layers, with relaxation timescales of 10 to 20 days.
JRA-55	0.1 hPa	A sponge layer is applied by gradually enhancing horizontal diffusion coefficients with increasing height at pressures less than 100 hPa. Rayleigh friction is also implemented at pressures less than 50 hPa.
MERRA	0.01 hPa	A sponge layer consisting of the nine uppermost model levels (pressures less than ~0.24 hPa) is implemented by increasing the horizontal divergence damping coefficient (see also Table 2-7). Advection at the top model level is reduced to first order.
MERRA-2	0.01 hPa	A sponge layer consisting of the nine uppermost model levels (pressures less than ~0.24 hPa) is implemented by increasing the horizontal divergence damping coefficient (see also Table 2-7). Advection at the top model level is reduced to first order.
NCEP-NCAR R1	3 hPa	No special treatment.
NCEP-DOE R2	3 hPa	No special treatment.
CFSR / CFSv2	~0.266 hPa	Linear Rayleigh damping with a time scale of 5 days is applied at pressures less than ~2 hPa. The horizontal diffusion coefficient also increases with scale height throughout the atmosphere.
NOAA-CIRES 20CR v2	~2.511 hPa	No special treatment.

273
274
275
276
277



278
279 Figure 2-1. Approximate vertical resolutions of the reanalysis forecast models for (a) the full
280 vertical range of the reanalyses and (b) the surface to 33 km (~10 hPa). Altitude and vertical
281 grid spacing are estimated using log-pressure altitudes ($z^* = H \ln[p_0/p]$), where the surface
282 pressure p_0 is set to 1000 hPa and the scale height H is set to 7 km. The grid spacing
283 indicating the separation of two levels is plotted at the altitude of the upper of the two levels,
284 so that the highest altitude shown in (a) indicates the height of the top level. Some
285 reanalyses use identical vertical resolutions; these systems are listed together in the legend.
286 Other reanalyses have very similar vertical resolutions when compared with other systems,
287 including JRA-55 (similar but not identical to ERA-40 and ERA-Interim) and 20CR (similar
288 but not identical to R1 and R2). Approximate vertical spacing associated with the isobaric
289 levels on which ERA-40 and ERA-Interim reanalysis products are provided (grey discs) is
290 shown in both panels for context.

291
292
293

294 2.2.2 Major physical parametrizations

295 Tables 2-4, 2-5, 2-6, and 2-7 briefly describe the radiative transfer, cloud, gravity wave drag,
296 and horizontal and vertical diffusion parametrizations used in the reanalysis forecast models.
297 Some of the effects of differences in these parametrizations will be explored in the later
298 chapters of this report. Note that the radiative transfer schemes used in the forecast model
299 may differ from the radiative transfer schemes used in the data assimilation system, which
300 are listed in Table 2-14. Other pertinent details include the treatment of incoming solar
301 radiation, surface boundary conditions, and radiatively active gases and aerosols, which are
302 summarized in section 2.2.3 (see also references in Table 2-1).

303
304 Table 2-4. Radiative transfer schemes used in the forecast models of the reanalysis systems.

ERA-40	Shortwave: Fouquart and Bonnel (1980) with four spectral intervals. Longwave: RRTM (Mlawer et al., 1997).
ERA-Interim	Shortwave: Updated version of Fouquart and Bonnel (1980). Longwave: RRTM (Mlawer et al., 1997). Note: The scheme is a revised version of that used in ERA-40, with more frequent radiation calculations (hourly rather than 3-

ERA-20C	hourly) as described by Dee et al. (2011). Shortwave: modified RRTM (Morcrette et al., 2008). Longwave: modified RRTM (Morcrette et al., 2008). Note: ERA-20C is the first ECMWF reanalysis to use the McICA approach to represent the radiative effects of clouds.
JRA-25 / JCDAS	Shortwave: Briegleb (1992) Longwave: line absorption based on the random band model of Goody (1952).
JRA-55	Shortwave: Briegleb (1992), updated to use the formulation of Freidenreich and Ramaswamy (1999) for shortwave absorption by O ₂ , O ₃ , and CO ₂ . Longwave: Chou et al. (2001).
MERRA	Shortwave: Chou and Suarez (1999). Longwave: Chou et al. (2001).
MERRA-2	Shortwave: Chou and Suarez (1999). Longwave: Chou et al. (2001).
NCEP-NCAR R1	Shortwave: GFDL (Lacis and Hansen, 1974). Longwave: GFDL (Fels and Schwarzkopf, 1975; Schwarzkopf and Fels, 1991). Note: Radiation calculations are performed every 3 hours on a 128×64 linear grid.
NCEP-DOE R2	Shortwave: Chou and Lee (1996). Longwave: GFDL (Fels and Schwarzkopf, 1975; Schwarzkopf and Fels, 1991; same as R1). Note: Radiation calculations are performed hourly on the full 192×94 Gaussian grid.
CFSR / CFSv2	Shortwave: RRTMG (Clough et al., 2005). Longwave: RRTMG (Clough et al., 2005). Note: The McICA approach for representing the radiative effects of clouds has been implemented in CFSv2, but not in CFSR.
NOAA-CIRES 20CR v2	Shortwave: Modified RRTMG (Clough et al., 2005). Longwave: Modified RRTMG (Clough et al., 2005). Note: The 20CR AGCM is very similar to the CFSR AGCM in most respects, including parametrizations, configuration, and treatment of radiation.

305

306 Table 2-5. Convective and non-convective cloud parametrizations used in the forecast
307 models of the reanalysis systems.

ERA-40	Convective: deep, shallow, and mid-level cumulus convection are parametrized using a bulk mass flux scheme based on that proposed by Tiedtke (1989). Each simulated convective cloud consists of a single pair of entraining/detraining plumes that represent updraught and downdraught processes. Non-convective: diagnosed using a prognostic cloud scheme (Tiedtke, 1993).
ERA-Interim	Convective: deep, shallow, and mid-level cumulus convection are parametrized using a bulk mass flux scheme based on that proposed by Tiedtke (1989), modified in several respects from those used in ERA-40. These changes result in improvements in the diurnal cycle of convection, increases in convective

	<p>precipitation efficiency and explicit distinctions among shallow, mid-level and deep convective clouds (Dee et al., 2011).</p> <p>Non-convective: diagnosed using a prognostic cloud scheme (Tiedtke, 1993), updated from ERA-40 to include a treatment for ice supersaturation at temperatures less than 250 K (Tompkins et al., 2007).</p>
ERA-20C	<p>Convective: deep, shallow, and mid-level cumulus convection are parametrized using a bulk mass flux scheme based on that proposed by Tiedtke (1989), similar to that used in ERA-Interim but with modified representations of entrainment and detrainment rates and a revised convective adjustment time scale.</p> <p>Non-convective: diagnosed using a prognostic cloud scheme (Tiedtke, 1993), updated from ERA-Interim to permit separate estimates of liquid and ice water in non-convective clouds.</p>
JRA-25 / JCDAS	<p>Convective: a prognostic mass-flux type Arakawa–Schubert cumulus scheme (Arakawa and Schubert, 1974).</p> <p>Non-convective: stratocumulus parametrization and cloud ice scheme as described by Kawai and Inoue (2006).</p>
JRA-55	<p>Convective: a prognostic mass-flux type Arakawa–Schubert cumulus scheme (Arakawa and Schubert, 1974), similar to that used by JRA-25/JCDAS but with a new triggering mechanism (Xie and Zhang, 2000).</p> <p>Non-convective: stratocumulus parametrization and cloud ice scheme as described by Kawai and Inoue (2006).</p>
MERRA	<p>Convective: a version of the relaxed Arakawa–Schubert cumulus scheme (Moorthi and Suarez, 1992).</p> <p>Non-convective: diagnosed using the scheme developed by Bacmeister et al. (2006).</p>
MERRA-2	<p>Convective: a version of the relaxed Arakawa–Schubert cumulus scheme (Moorthi and Suarez, 1992).</p> <p>Non-convective: diagnosed using the scheme developed by Bacmeister et al. (2006).</p> <p>Note: although the cloud parametrizations are the same as those used in MERRA, MERRA-2 applies new constraints on distributions of total water using the total water probability density functions proposed by Molod (2012).</p>
NCEP-NCAR R1	<p>Convective: deep convective clouds are simulated using a simplified Arakawa–Schubert convection scheme (Arakawa and Schubert, 1974); shallow convective clouds are simulated using a Tiedtke-type scheme (Tiedtke, 1989).</p> <p>Non-convective: diagnosed as a function of grid-scale relative humidity.</p>
NCEP-DOE R2	<p>Convective: deep convective clouds are simulated using a simplified Arakawa–Schubert convection scheme (Arakawa and Schubert, 1974); shallow convective clouds are simulated using a Tiedtke-type scheme (Tiedtke, 1989). These parametrizations have undergone minor tuning relative to those used by NCEP-NCAR R1.</p> <p>Non-convective: diagnosed using a relative humidity–cloud cover relationship, modified from that used by NCEP-NCAR R1.</p>

CFSR / CFSv2	Convective: deep convective clouds are simulated using a simplified Arakawa–Schubert convection scheme (Arakawa and Schubert, 1974; Moorthi et al. 2001); shallow convective clouds are simulated using a Tiedtke-type scheme (Tiedtke, 1983). Both schemes are updated relative to those used by R1 and R2 (Moorthi et al., 2010; Saha et al., 2010). Non-convective: a simple cloud physics parametrization with prognostic cloud condensate (Xu and Randall, 1996; Zhao and Carr, 1997).
NOAA-CIRES 20CR v2	Convective: deep convective clouds are simulated using a simplified Arakawa–Schubert convection scheme (Arakawa and Schubert, 1974; Moorthi et al. 2001); shallow convective clouds are simulated using a Tiedtke-type scheme (Tiedtke, 1989). Both schemes are updated relative to those used by R1 and R2 (Moorthi et al., 2010; Saha et al., 2010). Non-convective: a simple cloud physics parametrization with prognostic cloud condensate (Xu and Randall, 1996; Zhao and Carr, 1997).
308	
309	Table 2-6. Gravity wave drag parametrizations used in the forecast models of the reanalysis
310	systems.
ERA-40	The subgrid-scale orographic drag is parametrized using the scheme developed by Lott and Miller (1997). The representation of the orographic gravity wave source follows Miller (1989) and Baines and Palmer (1990), and accounts for three-dimensional variability in the amplitude and orientation of wave stress. Non-orographic gravity wave drag is represented as Rayleigh friction above the stratopause.
ERA-Interim	Essentially the same as in ERA-40. Subgrid-scale orographic drag is parametrized using the scheme developed by Lott and Miller (1997). The representation of orographic gravity wave source follows Miller (1989) and Baines and Palmer (1990), and accounts for three-dimensional variability in the amplitude and orientation of wave stress. Non-orographic gravity wave drag is represented as Rayleigh friction above the stratopause.
ERA-20C	Subgrid-scale orographic drag is parametrized using the scheme developed by Lott and Miller (1997), with slight modifications relative to ERA-40 and ERA-Interim that increase gravity wave activity. The representation of the orographic gravity wave source follows Miller (1989) and Baines and Palmer (1990). Non-orographic gravity wave drag is included using the parametrization proposed by Scinocca (2003); see also Orr et al. (2010).
JRA-25 / JCDAS	The orographic gravity wave drag parametrization consists of a long wave (wavelengths over 100 km) component and a short wave (wavelengths of ~10 km) component (Iwasaki et al., 1989a, 1989b). Long waves are assumed to propagate upward and break mainly in the stratosphere, where they exert drag (Palmer et al., 1986). Short waves are regarded as trapped and dissipating within the troposphere. Non-orographic gravity wave drag is not

	included.
JRA-55	Essentially the same as in JRA-25. The orographic gravity wave drag parametrization consists of a long wave (wavelengths over 100 km) component and a short wave (wavelengths of ~10 km) component (Iwasaki et al., 1989a, 1989b). Long waves are assumed to propagate upward and break mainly in the stratosphere, where they exert drag (Palmer et al., 1986). Short waves are regarded as trapped and dissipating within the troposphere. Non-orographic gravity wave drag is not included.
MERRA	MERRA includes parametrizations that compute momentum and heat deposition into the resolved flow by the breaking of orographic (McFarlane, 1987) and non-orographic (after Garcia and Boville, 1994) gravity waves.
MERRA-2	MERRA-2 includes parametrizations that compute momentum and heat deposition into the resolved flow by the breaking of orographic (McFarlane, 1987) and non-orographic (after Garcia and Boville, 1994) gravity waves. The scheme has been modified from that used in MERRA, with an increased latitudinal profile of the gravity wave drag background source at certain latitudes and increased intermittency (Molod et al., 2015).
NCEP-NCAR R1	An orographic gravity wave drag scheme based on Palmer et al. (1986), Pierrehumbert (1987), and Helfand et al. (1987) is included in the forecast model. Non-orographic gravity wave drag is not included.
NCEP-DOE R2	An orographic gravity wave drag scheme based on Palmer et al. (1986), Pierrehumbert (1987), and Helfand et al. (1987) is included in the forecast model. Non-orographic gravity wave drag is not included.
CFSR / CFSv2	The orographic gravity wave drag parametrization is based on the scheme proposed by Kim and Arakawa (1995). Sub-grid scale mountain blocking is represented using the scheme developed by Lott and Miller (1997). Although non-orographic gravity wave drag is not considered in CFSR, a simple representation of non-orographic gravity wave drag is included in CFSv2 via the parametrization proposed by Chun and Baik (1998).
NOAA-CIRES 20CR v2	The orographic gravity wave drag parametrization is based on the scheme proposed by Kim and Arakawa (1995). Sub-grid scale mountain blocking is represented using the scheme developed by Lott and Miller (1997). Non-orographic gravity wave drag is not considered.

311

312

313

Table 2-7. Representations of vertical and horizontal diffusion in the forecast models used by reanalysis systems.

ERA-40	Horizontal diffusion: Implicit linear fourth-order diffusion in spectral space. Vertical diffusion: Vertical diffusion in the free atmosphere and in the ABL under stable conditions is based on the revised Louis scheme (Louis, 1979; Beljaars, 1995) for positive Richardson numbers and on Monin–Obukhov similarity for negative Richardson numbers. Vertical diffusion in the ABL under
---------------	---

	unstable conditions is based on the non-local scheme proposed by Troen and Mahrt (1986). Turbulent fluxes in the surface layer are calculated using bulk formulae based on Monin–Obukhov similarity.
ERA-Interim	Horizontal diffusion: Implicit linear fourth-order diffusion in spectral space. Vertical diffusion: Vertical diffusion in the free atmosphere and in the ABL under stable conditions is based on the revised Louis scheme (Louis, 1979; Beljaars, 1995) for positive Richardson numbers and on Monin–Obukhov similarity for negative Richardson numbers. Vertical diffusion in the ABL under unstable conditions is based on an eddy-diffusivity mass-flux (EDMF) scheme (Köhler et al., 2011). Turbulent fluxes in the surface layer are calculated using bulk formulae based on Monin–Obukhov similarity.
ERA-20C	Horizontal diffusion: Implicit linear fourth-order diffusion in spectral space. Vertical diffusion: Vertical diffusion in the free atmosphere and in the ABL under stable conditions is based on the revised Louis scheme (Louis, 1979; Beljaars, 1995) for positive Richardson numbers and on Monin–Obukhov similarity for negative Richardson numbers. Vertical diffusion in the ABL under unstable conditions is based on an eddy-diffusivity mass-flux (EDMF) scheme (Köhler et al., 2011). Turbulent fluxes in the surface layer are calculated using bulk formulae based on Monin–Obukhov similarity.
JRA-25 / JCDAS	Horizontal diffusion: Implicit linear fourth-order diffusion in spectral space. Vertical diffusion: Vertical diffusion of momentum, heat, and moisture are represented using the turbulence closure scheme developed by Mellor and Yamada (1974). Surface turbulent fluxes are calculated using bulk formulae based on Monin–Obukhov similarity.
JRA-55	Horizontal diffusion: Implicit linear fourth-order diffusion in spectral space. Vertical diffusion: Vertical diffusion of momentum, heat, and moisture are represented using the turbulence closure scheme developed by Mellor and Yamada (1974). Surface turbulent fluxes are calculated using bulk formulae based on Monin–Obukhov similarity.
MERRA	Horizontal diffusion: Explicit second-order horizontal divergence damping is included in the dynamical core, with a dimensionless coefficient of 0.0075. Vertical diffusion: Vertical diffusion in the free atmosphere and in the boundary layer under stable conditions is based on a local gradient Richardson number closure (Louis et al., 1982), but a tuning parameter severely suppresses turbulent mixing at pressures less than ~900 hPa. Vertical diffusion in the boundary layer under unstable conditions is based on the non-local scheme proposed by Lock et al. (2000). A Monin–Obukhov-type

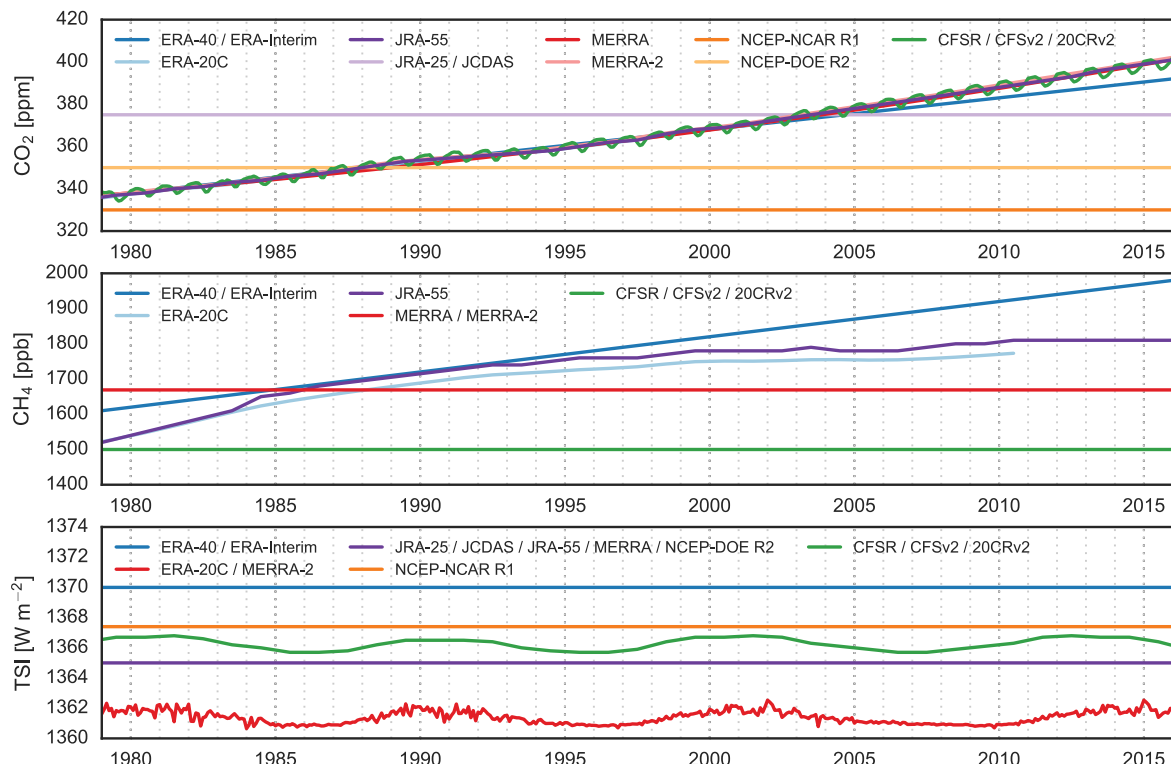
	parametrization is used for turbulent fluxes across the surface layer (Helfand and Schubert, 1995).
MERRA-2	<p>Horizontal diffusion: As in MERRA, an explicit second-order horizontal divergence damping with a dimensionless coefficient of 0.0075 is included. A second-order Smagorinsky divergence damping with a dimensionless coefficient of 0.2 is also applied in MERRA-2 (but not in MERRA).</p> <p>Vertical diffusion: Vertical diffusion in the free atmosphere and in the boundary layer under stable conditions is based on a local gradient Richardson number closure (Louis et al., 1982). The tuning parameter that suppressed turbulent mixing at pressures less than ~900 hPa in MERRA has been removed, but diffusion coefficients are still usually very small in the free atmosphere.</p> <p>Vertical diffusion in the boundary layer under unstable conditions is based on the non-local scheme proposed by Lock et al. (2000). A Monin–Obukhov-type parametrization is used for turbulent fluxes across the surface layer (Helfand and Schubert, 1995).</p>
NCEP-NCAR R1	<p>Horizontal diffusion: Implicit linear second-order diffusion in spectral space. Horizontal diffusion along model σ layers led to the occurrence of spurious “spectral precipitation”, particularly in mountainous areas at high latitudes. A special precipitation product was produced to correct this issue.</p> <p>Vertical diffusion: Local K diffusion (Louis et al., 1982) is applied in both the ABL and the free atmosphere with a uniform background diffusion coefficient.</p>
NCEP-DOE R2	<p>Horizontal diffusion: Implicit linear second-order diffusion in spectral space. Issues with spectral precipitation caused by horizontal diffusion are greatly reduced relative to R1.</p> <p>Vertical diffusion: Local K diffusion (Louis et al., 1982) is applied in the free atmosphere with a uniform background diffusion coefficient. Non-local diffusion is applied in the ABL (Hong and Pan, 1996).</p>
CFSR / CFSv2	<p>Horizontal diffusion: Implicit linear eighth-order diffusion in spectral space.</p> <p>Vertical diffusion: Local K diffusion (Louis et al., 1982) is applied in the free atmosphere with a background diffusion coefficient that decreases exponentially with pressure from a surface value of $1 \text{ m}^2 \text{ s}^{-1}$. Non-local vertical diffusion is applied in the ABL (Hong and Pan, 1996).</p>
NOAA-CIRES 20CR v2	<p>Horizontal diffusion: Implicit linear second-order diffusion in spectral space.</p> <p>Vertical diffusion: Local K diffusion (Louis et al., 1982) is applied in the free atmosphere with a background diffusion coefficient that decreases exponentially with pressure from a surface value of $1 \text{ m}^2 \text{ s}^{-1}$. Non-local vertical diffusion is applied in the ABL (Hong and Pan, 1996).</p>

317 2.2.3 Boundary and other specified conditions

318 This section describes the boundary and other specified conditions that can be regarded as
319 “externally supplied forcings” for each reanalysis system. These conditions comprise the
320 elements of the reanalysis that are not taken from the forecast model or data assimilation but
321 are used to produce the outputs. Figure 2-2 shows three examples of how externally-
322 specified boundary conditions may vary amongst reanalysis systems.
323

324 The factors that may be considered “external” vary somewhat among reanalyses because the
325 forecast and assimilation components have provided a progressively larger fraction of the
326 inputs (initial conditions) for the forecast model as reanalysis systems have developed.
327 Ozone is a prime example. As discussed below, all of the reanalysis systems except for
328 NCEP-NCAR R1, NCEP-DOE R2, and NOAA-CIRES 20CR (and JRA-55 and ERA-40 for
329 the period prior to 1978) assimilate satellite ozone measurements. Some of these reanalysis
330 systems (notably ERA-40, ERA-Interim, and ERA-20C) use ozone climatologies rather than
331 internally generated ozone fields for radiation calculations in the forecast model. Similarly,
332 MERRA-2 assimilates aerosol optical depths and uses internally generated aerosol fields for
333 the radiation calculations, while other systems use climatologies or neglect the role of
334 aerosols altogether. Moreover, CFSR is a coupled atmosphere–ocean–sea ice system, in
335 which the sea surface temperature (SST) and sea ice lower boundary conditions for the
336 atmospheric model are generated by an ocean model (although temperatures at the boundary
337 are relaxed every six hours to SST analyses similar to those used by other reanalysis
338 systems). This section summarizes the treatment of SST, sea ice, ozone, aerosols, trace
339 greenhouse gases (other than water vapour), and the solar cycle, with special notes where
340 necessary. Dynamical variables, water vapour, and internally generated ozone (i.e., variables
341 that are often directly constrained by the set of assimilated observations) are discussed and
342 evaluated in Chapters 3 and 4 of this report.

343
344
345



346
347 Figure 2-2. Time series of boundary conditions for CO₂ (top), CH₄ (center), and TSI
348 (bottom) used by the reanalysis systems. The CH₄ climatology used in MERRA and
349 MERRA-2 varies in both latitude and height; here a “tropospheric mean” value is calculated
350 as a mass- and area-weighted integral between 1000 and 288 hPa to facilitate comparison
351 with the “well-mixed” values used by most other systems. ERA-20C also applies rescalings
352 of annual mean values of both CO₂ and CH₄ that vary in latitude and height; here the base
353 values are shown. Time series of TSI neglect seasonal variations due to the ellipticity of the
354 Earth’s orbit, as these variations are applied similarly (but not identically) across reanalysis
355 systems. Additional information on CO₂ and CH₄ is provided in Table 2-11, and additional
356 information on TSI is provided in Table 2-12.
357

358 2.2.3.1 Sea surface temperature and sea ice

359 Table 2-8 summarizes the treatment of SST and sea ice distributions in the reanalysis
360 systems, including the names of SST and sea-ice datasets, special calibration or
361 preprocessing details (e.g., bias corrections, interpolations), and details of how the datasets
362 were produced.

363
364 Table 2-8. Treatment of sea surface temperature and sea ice.

ERA-40	Monthly data from the Met Office HadISST1 product was used before November 1981, replaced by weekly data from the NOAA–NCEP 2D-Var product from December 1981 through June 2001 and NOAA OISSTv2 from July 2001 through August 2002 (Fiorino, 2004). A special sea ice analysis and a method of specifying SST in grid boxes with partial ice-cover were used. Interpolation was used to produce daily values.
ERA-Interim	Monthly data from the Met Office HadISST1 product was used

	before November 1981, replaced by weekly data from the NOAA–NCEP 2D-Var product from December 1981 through June 2001 and NOAA OISSTv2 from July 2001 through December 2001. NCEP Real-Time Global sea surface temperatures (NCEP RTG) were used from January 2002 through January 2009. The Operational Sea Surface Temperature and Sea-Ice Analysis (OSTIA) has been used from February 2009 through the present. See also Dee et al. (2011).
ERA-20C	Daily gridded SST and sea ice are from HadISST version 2.1.0.0 (Titchner and Rayner, 2014) at 0.25° horizontal resolution. Daily fields have been obtained via cubic interpolation from monthly analyses, with the temporal average of daily fields constrained to match the analysed monthly mean.
JRA-25 / JCDAS	Daily COBE SSTs (Ishii et al., 2005) were used. COBE SSTs are based on the ICOADS and Kobe data collections, and do not include satellite data. Daily sea ice distributions prepared for COBE are based on reports by Walsh and Chapman (2001) for the Northern Hemisphere and Matsumoto et al. (2006) for the Southern Hemisphere.
JRA-55	Daily COBE SSTs (Ishii et al., 2005) were used. COBE SSTs are based on the ICOADS and Kobe data collections, and do not include satellite data. The COBE SST data include minor updates from those used for JRA-25/JCDAS. Daily sea ice distributions prepared for COBE are based on data reported by Walsh and Chapman (2001) for the Northern Hemisphere and Matsumoto et al. (2006) for the Southern Hemisphere after October 1978. Southern Hemisphere sea ice coverage before October 1978 is based on a climatology.
MERRA	Weekly NOAA OISST data at 1° resolution (Reynolds and Smith, 1994) are linearly interpolated in time to the model time steps.
MERRA-2	MERRA-2 uses monthly 1° gridded data (Taylor et al., 2000) prior to 1982, daily 0.25° gridded data (Reynolds et al., 2007) through March 2006, and daily 0.05° gridded data from OSTIA (Donlon et al., 2012) from April 2006.
NCEP-NCAR R1	SSTs are taken from the Met Office Global Ice and Sea Surface Temperature (GISST) data set for 1981 and earlier, and from the NOAA OISST data set from 1982 to the present. Sea ice cover is from Navy/NOAA Joint Ice Center analyses before 1978, from SMMR observations for 1978 through 1987, and from SSM/I observations for 1988 through the present. Snow cover is from the NESDIS weekly snow cover analysis (northern hemisphere only) for September 1998 and earlier, and from the US Air Force global snow cover analysis from October 1998 through the present.
NCEP-DOE R2	SSTs and sea ice cover for January 1979 through 15 August 1999 are taken from data prepared for AMIP-II and provided by the PCMDI at Lawrence Livermore National Laboratory. SSTs and sea ice cover for 16 August 1999 through December 1999 are from monthly NOAA OISST and monthly NCEP operational sea

	ice analyses, interpolated to daily resolution. SSTs and sea ice cover for January 2000 to present are from daily NOAA OISST and NCEP operational sea ice analyses.
CFSR / CFSv2	The atmospheric model is coupled to the GFDL MOM version 4 ocean model and a two-layer sea ice model. AVHRR and AMSR satellite infrared observations of SST are assimilated in the SST analysis, along with in situ data from ships and buoys. The sea (and lake) ice concentration analysis products assimilate different observational data depending on the period, including microwave satellite observations when available. Temperatures at the atmosphere–ocean boundary are relaxed every six hours to separate SST analyses, including the 1° gridded HadISST1.1 from January 1979 through October 1981 and versions 1 and 2 of the 0.25° gridded OI analyses described by Reynolds et al. (2007) from November 1981. Further details of the coupling procedure and SST/sea ice analysis have been provided by Saha et al. (2010).
NOAA-CIRES 20CR v2	HadISST1.1 monthly mean SST and sea ice data are interpolated to daily resolution. Sea ice concentrations were accidentally misspecified in coastal regions, as discussed by Compo et al. (2011).

365
366
367368 2.2.3.2 *Ozone*

369 Table 2-9 briefly summarizes the treatment of ozone in the reanalysis systems (detailed
 370 intercomparisons are deferred to Chapter 4). Some reanalysis systems assimilate satellite
 371 ozone measurements (from 1978/1979 onward) to produce an ozone analysis product, while
 372 some systems do not. Moreover, some systems that produce an ozone analysis use a
 373 climatological ozone distribution (rather than the ozone analysis) for radiation calculations
 374 in the forecast model. These distinctions are made explicit in Table 2-9. None of the
 375 reanalysis systems considered here assimilate data from ozonesondes.
 376

377 Table 2-9. Treatment of ozone. See also Chapter 4 of this report.

ERA-40	TOMS and SBUV ozone retrievals were assimilated from 1978 onward. Ozone in the model is described using a linearization of the ozone continuity equation, including photochemical sources and sinks (Cariolle and Déqué, 1986; Dethof and Hólm, 2004). The model does not account for heterogeneous chemistry, but does include an empirical ozone destruction term to account for chemical loss in polar stratospheric clouds. Model-generated ozone is not used in the radiation calculations, which instead assume the climatological ozone distribution reported by Fortuin and Langematz (1994).
ERA-Interim	Ozone retrievals are assimilated from TOMS (1979–present), SBUV (1979–present), GOME (1996–2002), MIPAS (2003–2004), SCIAMACHY (2003–2008), MLS (2008–present), and OMI (2008–present). The ozone scheme is an updated version of that used in ERA-40 (Cariolle and Teyssèdre, 2007; Dragani,

	2011). Model-generated ozone is not used in the radiation calculations, which instead assume the climatological ozone distribution reported by Fortuin and Langematz (1995).
ERA-20C	No ozone data are assimilated. The forecast model ozone parametrization is identical to that used in ERA-Interim. Model-generated ozone is not used in the radiation calculations, which instead use monthly three-dimensional ozone fields that evolve in time (Cionni et al., 2011).
JRA-25 / JCDAS	Daily ozone distributions were prepared in advance using the MRI-CCM1 offline chemical transport model with output “nudged” to satellite retrievals of total ozone. These distributions were provided to the forecast model for use in radiation calculations.
JRA-55	For 1979 and later, daily ozone distributions have been prepared in advance using the MRI-CCM1 offline chemical transport model with output “nudged” to satellite retrievals of total ozone. These distributions are provided to the forecast model for use in radiation calculations. This approach is similar to that used by JRA-25/JCDAS, but uses an updated chemical transfer model with 68 vertical levels rather than 45. For 1958–1978, a monthly mean climatology generated from the 1980–1984 ozone analyses was used.
MERRA	Version 8 SBUV ozone retrievals have been assimilated from October 1978 onward. The ozone parametrization is based on an empirical relationship between ozone and prognostic odd-oxygen that varies with height and the diurnal cycle (Rienecker et al., 2008). The forecast model uses analyzed ozone data in radiation calculations.
MERRA-2	Version 8.6 SBUV retrievals have been assimilated in reanalyses between 1980 and 2004. Starting from October 2004, these data have been replaced by retrieved MLS profiles (version 2.2 until May 2015 and version 4.2 afterwards) and OMI observations of total ozone. The ozone parametrization is based on an empirical relationship between ozone and prognostic odd-oxygen that varies with height and the diurnal cycle (Rienecker et al., 2008). The forecast model uses analyzed ozone data in radiation calculations.
NCEP-NCAR R1	Seasonal ozone climatologies reported by London (1962) and Hering et al. (1965) are used in radiation calculations. No ozone analysis is produced.
NCEP-DOE R2	The zonal mean ozone climatology published by Rosenfield et al. (1987) is used in radiation calculations, but the latitudinal orientation was reversed north-to-south. No ozone analysis is produced.
CFSR / CFSv2	Version 8 SBUV profiles and total ozone retrievals were assimilated without bias adjustment. Prognostic ozone is parametrized using concentration-dependent climatological production and destruction terms generated by a 2-dimensional chemistry model (McCormack et al., 2006). The forecast model uses analyzed ozone data for radiation calculations. Late 20 th

century levels of CFCs are included implicitly in the gas phase chemistry and ozone climatology used in the prognostic ozone parametrization.

**NOAA-CIRES 20CR
v2**

No ozone data are assimilated. Prognostic ozone is parametrized using concentration-dependent climatological production and destruction terms generated by a 2-dimensional chemistry model (McCormack et al., 2006), and is used by the forecast model for radiation calculations. Late 20th century levels of CFCs are included implicitly in the gas phase chemistry and ozone climatology used by the prognostic ozone parametrization.

378

379

380

381 2.2.3.3 *Aerosols*

382 Table 2-10 summarizes the treatment of stratospheric and tropospheric aerosols in the
 383 reanalysis systems. Some reanalysis systems consider tropospheric aerosols over continents
 384 and over oceans separately in the radiation scheme. Some reanalysis systems (but not all)
 385 account for changes in stratospheric aerosols due to volcanic eruptions. One reanalysis
 386 (MERRA-2) assimilates aerosol optical depths and uses analyzed aerosols in radiation
 387 calculations.
 388

389 Table 2-10. Treatment of aerosols.

ERA-40

Aerosols have been included in the radiation calculations using prescribed climatological aerosol distributions (Tanré et al., 1984). These distributions include annual mean geographical distributions for maritime, continental, urban and desert aerosol types, in addition to uniformly distributed tropospheric and stratospheric ‘background’ aerosol loading. No trends or temporal variations (such as variations due to volcanic eruptions) were included.

ERA-Interim

Aerosols are included in the radiation calculations using prescribed climatological aerosol distributions (Tegen et al., 1997). These distributions include annual mean geographical distributions for maritime, continental, urban and desert aerosol types, in addition to uniformly distributed tropospheric and stratospheric ‘background’ aerosol loading. The climatological annual cycles of tropospheric aerosols have been revised relative to those used by ERA-40, as have the optical thickness values for tropospheric and stratospheric background aerosols. There is no evolution of volcanic aerosols.

ERA-20C

The evolution of tropospheric aerosols is based on data prepared for CMIP5 (Lamarque et al., 2010; van Vuuren et al., 2011). Volcanic sulphates (Sato et al., 1993) and ash (Tanré et al., 1984) are also included in the stratosphere. A more detailed description of the aerosol fields used in ERA-20C and ERA-20CM has been provided by Hersbach et al. (2015).

JRA-25 / JCDAS

Aerosols are represented using two aerosol profiles, one over land and one over sea (WMO, 1986). Neither interannual nor

	seasonal variations are considered.
JRA-55	Aerosols are represented using two aerosol profiles, one over land and one over sea (WMO, 1986), with optical depths adjusted to a 2-dimensional monthly climatology (JMA, 2013). Interannual variations, such as those due to volcanic eruptions, are not considered.
MERRA	Aerosols are represented using a climatological aerosol distribution generated using the Goddard Chemistry, Aerosol, Radiation, and Transport (GOCART) model (Colarco et al., 2010).
MERRA-2	Aerosol optical depths from AVHRR, MODIS, MISR and AERONET are assimilated into the GEOS-5 Goddard Aerosol Assimilation System (GAAS; Buchard et al., 2015, 2016; Randles et al., 2016a, 2016b). The forecast model uses analyzed aerosols in radiation calculations for the entire production period. Additional details have been provided by Randles et al. (2016).
NCEP-NCAR R1	No aerosols.
NCEP-DOE R2	No aerosols.
CFSR / CFSv2	Aerosols are represented using a seasonally varying climatological global distribution of aerosol vertical profiles on a 5° grid (Koepke et al., 1997). Monthly zonal mean volcanic aerosols in four latitude bands (90–45°S, 45°S–equator, equator–45°N, 45–90°N) are specified based on data reported by Sato et al. (1993).
NOAA-CIRES 20CR v2	Aerosols are represented using a seasonally varying climatological global distribution of aerosol vertical profiles on a 5° grid (Koepke et al., 1997). Monthly zonal mean volcanic aerosols in four latitude bands (90–45°S, 45°S–equator, equator–45°N, 45–90°N) are specified based on data reported by Sato et al. (1993).

390
391
392393 2.2.3.4 *Carbon dioxide and other radiatively active gases*394 Table 2-11 summarizes the treatment of carbon dioxide and other radiatively active gases
395 (with the exception of water vapour) in the reanalysis systems (see also Fig. 2-2). Notes on
396 the treatment of water vapour are provided in Section 2.4.3.
397

398 Table 2-11. Treatment of carbon dioxide and other radiatively active gases.

ERA-40	CO ₂ , CH ₄ , N ₂ O, CFC-11, and CFC-12 are assumed to be well mixed globally. The concentrations of these gases were set to the observed 1990 values plus a linear trend as specified by IPCC (1996).
ERA-Interim	CO ₂ , CH ₄ , N ₂ O, CFC-11, and CFC-12 are assumed to be well mixed globally. The concentrations for these gases are set to observed 1990 values plus a linear trend as specified by IPCC (1996). The treatment is identical to that used by ERA-40.
ERA-20C	CO ₂ , CH ₄ , N ₂ O, CFC-11, and CFC-12 are specified according to

	CMIP5-recommended values (Meinshausen et al., 2011). The IPCC RCP3PD scenario is followed for 2006–2010. Greenhouse gases are not assumed to be globally well mixed; rather, they are rescaled to match specified seasonal cycles and zonal mean vertical distributions (Hersbach et al., 2015).
JRA-25 / JCDAS	A constant, globally uniform CO ₂ concentration of 375 ppmv was assumed. CH ₄ , N ₂ O, CFCs, and HCFCs were not considered.
JRA-55	Daily values of CO ₂ , CH ₄ , N ₂ O, CFC-11, CFC-12, and HCFC-22 are specified by interpolating from annual mean values. For CO ₂ , CH ₄ , and N ₂ O these annual mean values are valid on 1 July; for CFC-11, CFC-12, and HCFC-22 they are valid on 31 December. All species are assumed to be globally uniform. Data sources vary in time (Kobayashi et al., 2015; their Table 7).
MERRA	CO ₂ concentrations are assumed to be globally well mixed and are specified according to historical observed values. CH ₄ , N ₂ O, CFCs, and HCFCs are specified according to steady state monthly climatologies from the Goddard two-dimensional chemistry transport model (Rienecker et al., 2008). These monthly climatologies vary in both latitude and pressure, but do not contain interannual variability.
MERRA-2	Annual global mean CO ₂ concentrations follow the IPCC RCP4.5 scenario. CH ₄ , N ₂ O, CFCs, and HCFCs are specified according to steady state monthly climatologies from the Goddard two-dimensional chemistry transport model (Rienecker et al., 2008). These monthly climatologies vary in both latitude and pressure, but do not contain interannual variability.
NCEP-NCAR R1	A constant, globally uniform CO ₂ concentration of 330 ppmv is assumed. CH ₄ , N ₂ O, CFCs, and HCFCs are not considered.
NCEP-DOE R2	A constant, globally uniform CO ₂ concentration of 350 ppmv is assumed. CH ₄ , N ₂ O, CFCs, and HCFCs are not considered.
CFSR / CFSv2	Monthly mean 15°×15° distributions of CO ₂ concentrations derived from historical WMO Global Atmosphere Watch observations are used. Constant values of CH ₄ , N ₂ O, O ₂ , and four types of halocarbons are also included in the radiation calculations.
NOAA-CIRES 20CR v2	Monthly mean 15°×15° distributions of CO ₂ concentrations derived from historical WMO Global Atmosphere Watch observations are used for 1956 and later. Semi-annual averages of global mean CO ₂ concentrations based on ice core data are specified for the period before 1956. Constant values of CH ₄ , N ₂ O, O ₂ , and four types of halocarbons are also included in the radiation calculations.

399
400
401

402 2.2.3.5 *Solar cycle*

403 The solar cycle (i.e., changes in total solar irradiance, or TSI, with a period of ~11 years) is
404 an important driver of atmospheric variability. This variability is incorporated in reanalysis

systems in a variety of ways, including specified solar radiation at the TOA (boundary condition) and/or observations of temperature or ozone (data assimilation). Table 2-12 briefly summarizes the representation of the solar cycle in each reanalysis system (see also Fig. 2-2).

Table 2-12. Influence of solar cycle on the reanalysis systems.

ERA-40	The ~11-year solar cycle is not included in the TSI boundary condition, with the base irradiance assumed to be constant at 1370 W m^{-2} ; however, variations in this value due to changes in the distance between the Earth and the Sun have been incorporated as prescribed by Paltridge and Platt (1976). A programming error artificially increased the effective TSI by about 2 W m^{-2} relative to the specified value. Dee et al. (2011) reported that the impact of this error is mainly expressed as a warming of approximately 1 K in the upper stratosphere; systematic errors in other regions are negligible. The effects of the solar cycle are included in the assimilated upper-air temperatures, but are not included in the ozone passed to the forecast model (see Table 2-9).
ERA-Interim	The ~11-year solar cycle is not included in the TSI boundary condition, with the base irradiance assumed to be constant at 1370 W m^{-2} ; however, variations in this value due to changes in the distance between the Earth and the Sun have been incorporated as prescribed by Paltridge and Platt (1976). A programming error artificially increased the effective TSI by about 2 W m^{-2} relative to the specified value. Dee et al. (2011) reported that the impact of this error is mainly expressed as a warming of approximately 1 K in the upper stratosphere; systematic errors in other regions are negligible. The effects of the solar cycle are included in the assimilated upper-air temperatures, but are not included in the ozone passed to the forecast model (see Table 2-9).
ERA-20C	ERA-20C uses TSI variations provided for CMIP5 historical simulations by the SPARC SOLARIS-HEPPA working group with the TIM scaling applied, which take values ranging from 1360.2 to 1362.7 W m^{-2} between 1900 and 2008. These variations account for solar cycle changes through 2008 and repeat the final cycle (April 1996–June 2008) thereafter. Seasonal variations due to the ellipticity of the Earth’s orbit are also included.
JRA-25 / JCDAS	A constant base TSI of 1365 W m^{-2} was assumed, including seasonal effects due to the ellipticity of the Earth’s orbit (Spencer, 1971). Interannual variations in incoming solar radiation were not included in the TSI boundary condition, but were included in assimilated temperature and ozone observations.
JRA-55	A constant base TSI of 1365 W m^{-2} is assumed, including seasonal effects due to the ellipticity of the Earth’s orbit (Spencer, 1971). Interannual variations in incoming solar radiation are not included in the TSI boundary condition, but are

	included in assimilated temperature observations (for the whole period) and ozone observations (for 1979 and later).
MERRA	MERRA assumes a constant base TSI of 1365 W m^{-2} . Seasonal variations due to the ellipticity of the Earth's orbit are also included.
MERRA-2	MERRA-2 uses TIM-corrected TSI variations provided for CMIP5 historical simulations by the SPARC SOLARIS-HEPPA working group, which take values ranging from 1360.6 to 1362.5 W m^{-2} between 1980 and 2008. These variations account for solar cycle changes through 2008 and repeat the final cycle (April 1996–June 2008) thereafter. Seasonal variations due to the ellipticity of the Earth's orbit are also included.
NCEP-NCAR R1	R1 uses a constant TSI of 1367.4 W m^{-2} . The ~11-year solar cycle is not included in the TSI boundary condition, but variations due to changes in orbital geometry are accounted for. The effects of the solar cycle are included in the assimilated upper-air temperatures, but are not included in the ozone passed to the forecast model (see Table 2-9).
NCEP-DOE R2	R2 uses a constant TSI of 1365 W m^{-2} . The ~11-year solar cycle is not included in the TSI boundary condition, but variations due to changes in orbital geometry are accounted for. The effects of the solar cycle are included in the assimilated upper-air temperatures, but are not included in the ozone passed to the forecast model (see Table 2-9).
CFSR / CFSv2	Annual average variations in TSI were specified according to data prepared by H. van den Dool (personal communication, 2006), which take values ranging from 1365.7 to 1367.0 W m^{-2} . The solar cycle after 2006 is repeated forwards (e.g., insolation for 2007 is the same as that for 1996, that for 2008 is the same as that for 1997, and so on). The effects of the solar cycle are included in assimilated temperature and ozone observations; however, the prognostic ozone parametrization does not otherwise account for variations in incoming solar radiation.
NOAA-CIRES 20CR v2	Annual average variations in TSI were specified according to data prepared by H. van den Dool (personal communication, 2006), which take values ranging from 1365.7 to 1367.0 W m^{-2} . The solar cycle before 1944 is repeated backwards (e.g., insolation for 1943 is the same as that for 1954, that for 1942 is the same as that for 1953, and so on) and the solar cycle after 2006 is repeated forwards (as for CFSR). No upper-air observations were assimilated or included, and the prognostic ozone parametrization does not account for variations in incoming solar radiation.

414 **2.3 ASSIMILATION SCHEMES**415 **2.3.1 Basics of data assimilation**

416 This section provides a brief overview of data assimilation concepts and methods as
 417 implemented in current reanalysis systems. More detailed summaries have been provided by
 418 Krishnamurti and Bounoua (1996) and Bouttier and Courtier (1999). In this context, an
 419 analysis is a best estimate of the true state of the atmosphere at a given time t . Reanalysis
 420 systems use objective analysis methods that employ mathematical optimization (data
 421 assimilation) techniques to combine model-generated forecasts and observed data, given
 422 constraints that are intended to preserve consistency. The results should be reproducible,
 423 internally consistent, and spatially continuous.

424
 425 Data ingested into an analysis system may include observations and variables from a first
 426 guess background state (such as a previous analysis or forecast). Analysis systems are
 427 constructed to be consistent with known or assumed physical properties (such as smoothness,
 428 hydrostatic balance, geostrophic or gradient-flow balance, or more complex non-linear
 429 balances). Both the observations and the background state include important information,
 430 and neither should be considered as ‘truth’: both the model and observations include errors
 431 and uncertainties. An analysis system must therefore adopt a consistent and objective
 432 strategy for minimizing the differences between the analysis and the (unknown) true state of
 433 the atmosphere. Such strategies should on average reduce the errors and uncertainties
 434 associated with both observations and the first-guess background state. To this end, data
 435 assimilation algorithms often employ statistics to represent the range of potential
 436 uncertainties in the background state, observations, and any techniques used to convert
 437 between model and observational space (such as spatial interpolation techniques or vertical
 438 weighting functions), and ultimately aim to minimize these potential uncertainties.
 439

440 The analysis methods used by current reanalysis systems include variational methods (3D-
 441 Var and 4D-Var) and the ensemble Kalman filter (EnKF). Variational methods (e.g.
 442 Talagrand, 2010) minimize an objective cost function that penalizes differences between
 443 observations and the model background state, with consideration of associated uncertainties.
 444 Implementations of variational data assimilation may be applied to derive optimal states at
 445 discrete times (3D-Var), or to identify optimal state trajectories within finite time windows
 446 (4D-Var). In EnKF (e.g. Evensen, 2009), an ensemble of forecasts is used to define a
 447 probability distribution of background states (the prior distribution), which is then combined
 448 with observations and associated uncertainties to derive a probability distribution of analysis
 449 states (the posterior distribution). The optimal analysis state is determined by applying a
 450 Kalman filter (Kalman, 1960) to this posterior distribution (see also Evensen and van
 451 Leeuwen, 2000). One of the key advantages of 3D-Var, 4D-Var, and EnKF methods relative
 452 to many earlier implementations of data assimilation is the ability to account for nonlinear
 453 relationships between observed quantities and analysis variables. This ability to use
 454 nonlinear observation operators permits the direct assimilation of satellite radiance data
 455 without an intermediate retrieval step (Tsuyuki and Miyoshi, 2007), and underpins many of
 456 the recent advances in reanalysis development.
 457

458 Figure 2-3 shows simplified one-dimensional schematic representations of four data
 459 assimilation strategies used by current reanalysis systems (3D-Var, 3D-FGAT, 4D-Var, and
 460 EnKF). In the following discussion, we frequently refer to the assimilation increment, which
 461 is defined as the adjustment applied to the first guess (forecast) background state following

462 the assimilation of observational data (i.e., the difference between the analysis state and the
 463 first guess background state). We also use the term observation increment, which refers to
 464 the weighted contribution of a specific observation to the assimilation increment. The
 465 assimilation increment therefore reflects the combination of all observation increments
 466 within an assimilation window, where the assimilation window is the time period containing
 467 observations that influence the analysis. The assimilation window used in reanalyses is
 468 typically between 6 and 12 hours long, and is often (but not always) centred at the analysis
 469 time. Core differences among the data assimilation strategies used in current reanalysis
 470 systems can be understood in terms of how the assimilation increment is calculated and
 471 applied.

472 The 3D-Var method (Figure 2-3a) calculates and applies assimilation increments only at
 473 discrete analysis times. Observation increments within the assimilation window may either
 474 be treated as though they were all at the analysis time (which approximates the average
 475 observation time) or weighted by when they occurred (so that observations collected closer
 476 to the analysis time have a stronger impact on the assimilation increment). JRA-25 uses a
 477 3D-Var method for data assimilation under the former assumption, in which all observations
 478 within the assimilation window are treated as valid at the analysis time. In practice, many
 479 3D-Var systems estimate observation increments at observation times rather than analysis
 480 times (Figure 2-3b). This approach is referred to as 3D-FGAT (“first guess at the appropriate
 481 time”; Lawless, 2010). The implementation of 3D-FGAT in reanalysis systems varies. For
 482 example, R1 and R2 estimate observation increments using a linear interpolation between
 483 the initial and final states of the forecast before the analysis time and a constant extrapolated
 484 value after the analysis time (this approach is illustrated in Figure 2-3b). Other 3D-FGAT
 485 systems break each forecast into multiple piecewise segments of 30 minutes (ERA-40), one
 486 hour (CFSR), or three hours (MERRA and MERRA-2) in length. The observation
 487 increments are then calculated by interpolating to observation times within each piecewise
 488 segment.

489 MERRA and MERRA-2 include an additional step relative to other 3D-FGAT systems, and
 490 generate two separate sets of reanalysis products (designated “ANA” for analysis state and
 491 “ASM” for assimilated state) using an iterative predictor–corrector approach (Rienecker et
 492 al., 2011). The “ANA” products are analogous to the analyses produced by other 3D-FGAT
 493 systems, and are generated by using the data assimilation scheme to adjust the background
 494 state produced by a 12-h “predictor” forecast (from 9 h before the analysis time to 3 h after).
 495 The “ASM” products, which have no analogue among other 3D-FGAT reanalyses, are
 496 generated by conducting a 6-h “corrector” forecast centred on the analysis time and using
 497 incremental analysis update (IAU; Bloom, 1996) to apply the previously calculated
 498 assimilation increment gradually (at 30 minute intervals) rather than abruptly at the analysis
 499 time. The corrector forecast thus generates a more complete suite of atmospheric variables
 500 and tendency terms (the “ASM” products) that remains consistent with the assimilation
 501 increment while reducing wind and tracer imbalances relative to the 3D-FGAT analysis. The
 502 corrector forecast is then extended 6 h to generate the next predictor state. This iterative
 503 predictor–corrector procedure is illustrated in Figure 2-4.

504 Unlike 3D-Var and 3D-FGAT, which attempt to optimize the fit between assimilated
 505 observations and the atmospheric state at discrete analysis times, 4D-Var (Figure 2-3c)
 506 attempts to optimize the fit between assimilated observations and the time-varying forecast
 507 trajectory within the full assimilation window (e.g. Park and Županski, 2003). 4D-Var
 508 makes more complete use of observations collected between analysis times than 3D-Var or

512 3D-FGAT, and has been shown to substantially improve the resulting analysis (Talagrand,
513 2010). However, the computational resources required to run a 4D-Var analysis are much
514 greater than the computational resources required to run a 3D-Var or 3D-FGAT analysis,
515 and the full implementation of 4D-Var remains impractical at present. Current reanalysis
516 systems using 4D-Var (such as ERA-Interim, ERA-20C, and JRA-55) therefore apply the
517 simplified “incremental 4D-Var” approach described by Courtier et al. (1994). Under this
518 approach, the model state at the beginning of the assimilation window is iteratively adjusted
519 to obtain progressively better fits between the assimilated observations and the forecast
520 trajectory. This iterative adjustment process propagates information both forward and
521 backward in time, which substantially benefits the analysis but requires the derivation and
522 maintenance of an adjoint model. The latter is a difficult and time-consuming process, and is
523 a significant impediment to the implementation of 4D-Var. Incremental 4D-Var is tractable
524 (unlike full 4D-Var), but it is still computationally expensive, and is therefore usually
525 implemented in two nested loops for computational efficiency. Assimilation increments are
526 first tested and refined in an inner loop with reduced resolution and simplified physics, and
527 then applied in an outer loop with full resolution and full physics after the inner loop
528 converges.

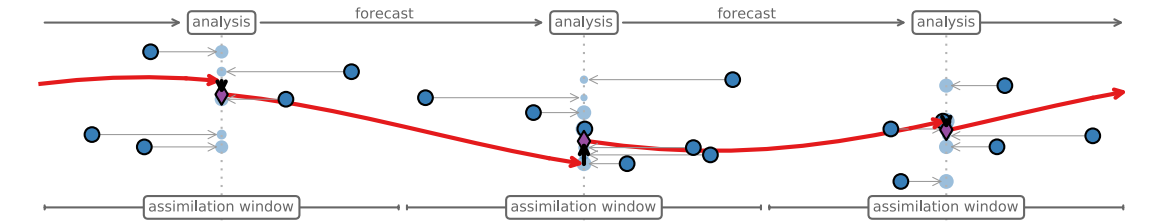
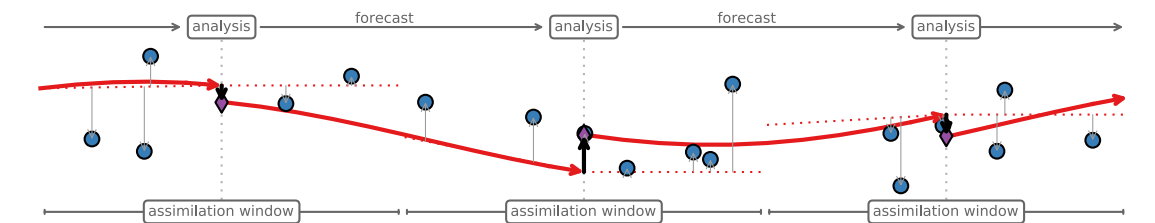
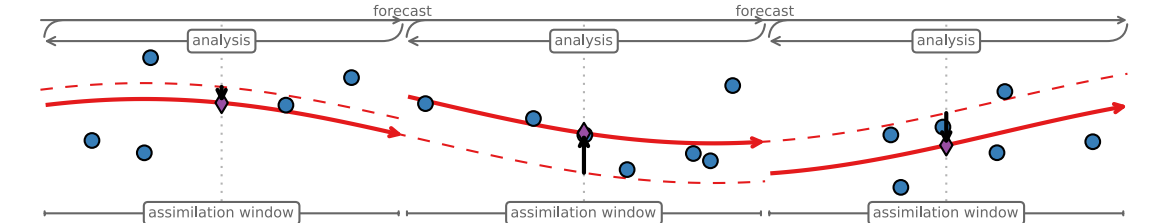
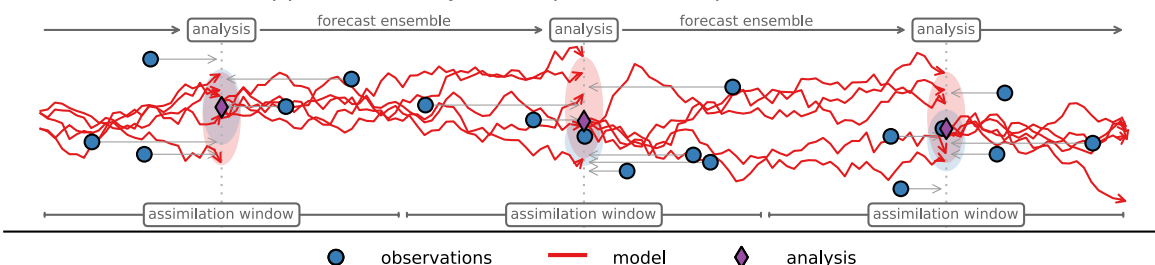
529

530 Most implementations of variational methods in reanalysis systems are based on single
531 deterministic forecasts. By contrast, EnKF (Figure 2-3d) uses an ensemble approach to
532 evaluate and apply assimilation increments. Major advantages of the ensemble Kalman filter
533 technique include ease of implementation (unlike 4D-Var, EnKF does not require an adjoint
534 model) and the generation of useful estimates of analysis uncertainties, which are difficult to
535 obtain when using variational techniques with single forecasts (the forthcoming ERA5 will
536 use 4D-Var in an ensemble framework, in part to address this issue). Whitaker et al. (2009)
537 found that in the case of a reanalysis that assimilates only surface pressure observations, the
538 performance of the 4D-Var and EnKF techniques is comparable, and that both 4D-Var and
539 EnKF give more accurate results than 3D-Var. 20CR uses an EnKF method for data
540 assimilation.

541

542 Additional details regarding these methods, including relative advantages and disadvantages,
543 have been discussed and summarized by Park and Županski (2003), Lorenc and Rawlins
544 (2005), Kalnay et al. (2007a; 2007b), Gustafsson (2007), and Buehner et al. (2010a; 2010b),
545 among others.

546

a 3D-Var (increments calculated and applied at analysis times)**b 3D-FGAT (increments estimated at observation times but applied at analysis times)****c 4D-Var (iteratively estimate increments for full window and adjust initial state)****d EnKF (increment applied as a Bayesian update to the posterior forecast ensemble)**

● observations — model ♦ analysis

547

548

549

550

551

552

553

554

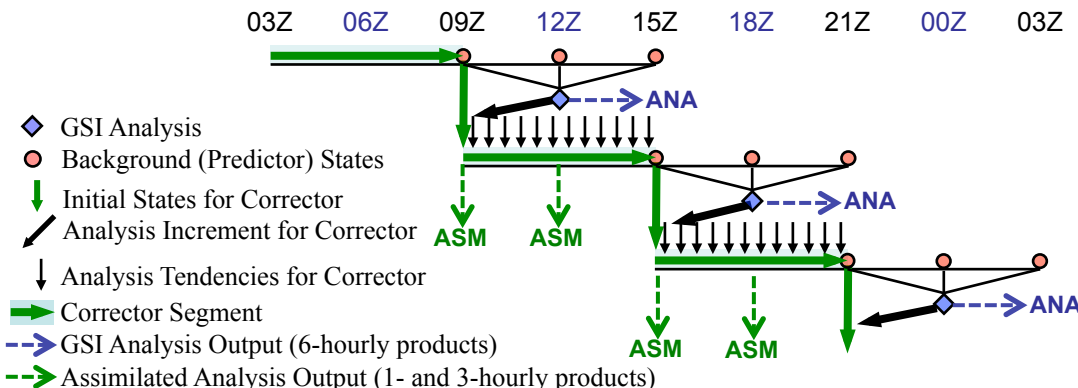
555

556

557

558

Figure 2-3. Simplified schematic representations of four data assimilation strategies used by current reanalyses: (a) 3D-Var; (b) 3D-FGAT; (c) incremental 4D-Var; and (d) EnKF. Blue circles represent observations, red lines represent the model trajectory, and purple diamonds indicate the analysis. The dotted red lines in (b) represent linearly interpolated/extrapolated first guesses used to estimate increments at observation times. The dashed red lines in (c) represent the initial forecasts, prior to iterative adjustments. These illustrations are conceptual, and should not be taken as exact depictions of the much more complex strategies used by reanalysis systems.



559
560 Figure 2-4. A schematic illustration of IAU as implemented in MERRA and MERRA-2
561 (modified from Rienecker et al., 2011). See text for details.
562
563
564

565 The assimilation of observational data can introduce spurious artefacts into reanalyses of the
566 state and variability of the upper troposphere, stratosphere, and mesosphere. For example,
567 data assimilation can act to smooth sharp vertical gradients in the vicinity of the tropopause.
568 The potential importance of this effect is illustrated by abrupt changes in vertical
569 stratification near the tropopause at the beginning of the satellite era in R1 (Birner et al.,
570 2006). Changes in data sources and availability can also lead to biases and artificial
571 oscillations in temperature in various regions of the stratosphere, particularly in the polar
572 and upper stratosphere where observations are sparse (Randel et al., 2004; Uppala et al.,
573 2005; Simmons et al., 2014; Lawrence et al., 2015). Information and errors introduced by
574 the input data and data assimilation system propagate upwards through the middle
575 atmosphere in both resolved waves and parametrized gravity wave drag (Polavarapu and
576 Pulido, 2016). The effects of this propagation can be either desirable or undesirable. The
577 abrupt application of assimilation increments can generate spurious gravity waves in
578 systems that use intermittent data assimilation techniques (Schoeberl et al., 2003), including
579 most implementations of 3D-Var, 3D-FGAT, and EnKF, and may also generate instabilities
580 that artificially enhance mixing and transport in the subtropical lower stratosphere (Tan et al.,
581 2004). Reanalyses of the stratosphere and mesosphere are therefore quite sensitive to the
582 details of the data assimilation scheme and input data at lower altitudes.
583
584
585

586 2.3.2 Data assimilation in reanalysis systems

587 Table 2-13 summarizes the assimilation schemes used in the reanalysis systems, which
588 include variations on the 3D-Var, 3D-FGAT, 4D-Var, and EnKF techniques.
589

590 Table 2-13. List of assimilation schemes used in the reanalysis systems.

ERA-40	3D-FGAT with a 6-h forecast step ending at the analysis time and a 6-h assimilation window centred on the analysis time. Analysis tendencies are calculated in 30-minute windows and then combined to construct the analysis increment.
---------------	---

ERA-Interim	Incremental 4D-Var atmospheric analysis with 12-h assimilation windows extending from 3 h before the 00 and 12 UTC analysis times to 3 h after the 06 and 18 UTC analysis times. Analysis increments are calculated on coarser grids that approach the model resolution over successive iterations. Separate six-hourly analyses are carried out for screen-level, land-surface and sea-state variables.
ERA-20C	Incremental 4D-Var analysis with 24-h assimilation windows extending from 09 UTC to 09 UTC. Assumed background error covariances are invariant in time, although a scaling is applied for consistency with time-varying background errors produced by an earlier 10-member ensemble pilot reanalysis that also assimilated only surface observations (Poli et al., 2013, 2016).
JRA-25 / JCDAS	3D-Var (not 3D-FGAT) with 6-h forecast steps. Observations from 3 hours before the analysis to 3 hours afterwards are considered.
JRA-55	Incremental 4D-Var with a 9-h forecast step that extends 3 h past the analysis time and a 6-h assimilation window centred on the analysis time. Analysis increments are calculated on a coarser T106/F80 inner grid (rather than the T _L 319/N160 outer grid used in the forecast model) to limit computational expense.
MERRA	Gridpoint statistical interpolation (GSI) plus incremental analysis update (IAU; Bloom et al., 1996), with 6-h assimilation windows centred on each analysis time. The IAU procedure (Figure 2-4) is a variation on 3D-FGAT that uses information from two forecast steps, a 12-h “predictor” forecast (from 9 h before the analysis time to 3 h after) and a 6-h “corrector” forecast (centred on the analysis time). Analysis tendencies are calculated at 30-minute intervals based on the portion of the predictor segment that overlaps the assimilation window, and then applied gradually to the corrector segment (rather than abruptly at the analysis time, as in standard 3D-FGAT). The midpoint of the corrector segment is then taken as the analysis, and the corrector forecast is extended 6 h to generate the next predictor state. The humidity variable used for the assimilation is pseudo-relative humidity, which is defined as the water vapour mixing ratio divided by the saturation mixing ratio of the background field (i.e., pseudo-RH does not change if no observations of moisture are assimilated, even with a non-zero analysis increment in temperature).
MERRA-2	GSI with IAU as in MERRA, but with updated background error specifications. The humidity variable used for the assimilation is a pseudo-relative humidity. Unlike MERRA, this variable is normalized by the background error standard deviation, which leads to a more Gaussian error distribution. A global constraint is imposed on the analysis increment of total water (Takacs et al., 2015).
NCEP-NCAR R1	Spectral statistical interpolation (SSI) in a 3D-FGAT configuration with a 6-hour assimilation window centred on each analysis time. For times before the analysis time, first guesses are based on linear interpolation between the initial and final model

	states. For times after the analysis time, first guesses are estimated as the first guess at the analysis time.
NCEP-DOE R2	Spectral statistical interpolation (SSI) in a 3D-FGAT configuration with a 6-hour assimilation window centred on each analysis time. For times before the analysis time, first guesses are based on linear interpolation between the initial and final model states. For times after the analysis time, first guesses are estimated as the first guess at the analysis time.
CFSR / CFSv2	Gridpoint statistical interpolation (GSI) with 9-h forecasts (from 6 h before to 3 h after each analysis time) and 6-h assimilation windows (centred on each analysis time). The implementation of GSI in CFSR is a form of 3D-FGAT with hourly first guesses, but it does not include the incremental analysis update (IAU) procedure used by MERRA.
NOAA-CIRES 20CR v2	Ensemble Kalman filter (EnKF) with a 6-h window centred on each analysis time. Observations from 3 hours before the analysis to 3 hours afterwards are used. The EnKF implementation in 20CR uses a window that straddles the analysis time, and is therefore technically an Ensemble Kalman Smoother (Compo et al., 2011).

591

592

593

594 The assimilation of observed satellite radiances by a reanalysis system requires the use of a
 595 radiative transfer scheme. This scheme typically differs from that used in the forecast model
 596 (Table 2-4). Table 2-14 lists the radiative transfer schemes used by each reanalysis system
 597 for assimilating satellite radiances.

598

599 Table 2-14. List of radiative transfer schemes used for assimilating satellite radiances.

ERA-40	RTTOV-5 is used for assimilating satellite radiances.
ERA-Interim	RTTOV-7 is used for assimilating satellite radiances.
ERA-20C	Satellite radiances are not assimilated (see also Table 2-16).
JRA-25 / JCDAS	RTTOV-6 is used for assimilating TOVS radiances and RTTOV-7 is used for assimilating ATOVS radiances.
JRA-55	RTTOV-9 is used for assimilating satellite radiances.
MERRA	The GLATOVS radiative transfer model is used for assimilating SSU radiances; the CRTM is used for assimilating all other satellite radiances.
MERRA-2	All radiances are assimilated using version 2.1.3 of the CRTM.
NCEP-NCAR R1	Satellite radiances are not assimilated (see also Table 2-16).
NCEP-DOE R2	Satellite radiances are not assimilated (see also Table 2-16).
CFSR / CFSv2	CFSR uses the CRTM developed at NOAA/NESDIS and the JCSDA for assimilating satellite radiances.
NOAA-CIRES 20CR v2	Satellite radiances are not assimilated (see also Table 2-16).

600

601

602

603 **2.4 OBSERVATIONAL DATA**604 **2.4.1 Summary of basic information**

605 This section provides information on key observational data assimilated in the reanalysis
 606 systems. Reanalysis systems assimilate observational data from a variety of sources. These
 607 sources are often grouped into two main categories: conventional data (e.g. surface records,
 608 radiosonde profiles, and aircraft measurements) and satellite data (e.g. microwave and
 609 infrared radiances, atmospheric motion vectors inferred from satellite imagery, and various
 610 retrieved quantities).

611
 612 The densities and distributions of both types of observational data have changed
 613 considerably over time. Figure 2-5 shows examples of the spatial distributions of
 614 observations assimilated by JRA-55 in the 1980s (00 UTC, 22 September 1983), while
 615 Figure 2-6 shows examples of the spatial distributions of observations assimilated by the
 616 same reanalysis system in the 2010s (00 UTC, 23 June 2010). These two sets of examples
 617 are representative of the distribution and number of observations assimilated in most recent
 618 reanalysis systems (with the notable exception of ERA-20C and 20CR, which do not
 619 assimilate upper-air observations). Figures 2-7 through 2-10 summarize the availability of
 620 different types of observations assimilated in five of the most recent reanalysis systems as a
 621 function of time. Figure 2-11 provides a more detailed look at how the availability of
 622 radiances observed by certain instruments changes as satellites are launched and retired.
 623 Common codes and terminology for assimilated observations are listed in Table 2-15.

624
 625 A number of key features are apparent in Figures 2-5 through 2-11. First, conventional in-
 626 situ data (such as surface, radiosonde, and aircraft data) are unevenly distributed in space.
 627 Second, satellite data (microwave and infrared sounder data, air motion vector data from
 628 geostationary and polar satellites, etc.) are often more evenly distributed but still
 629 inhomogeneous in space. Third, none of these datasets are continuous and homogeneous in
 630 time. For example, microwave and infrared sounders (i.e., the TOVS suite) were introduced
 631 in 1979, while advanced sounders (i.e., the ATOVS suite) were introduced in 1998. Such
 632 changes in the availability of observational data for assimilation have strong impacts on the
 633 quality of the reanalysis datasets that assimilate them, so that discontinuities in reanalysis
 634 data should be carefully evaluated and checked for coincidence with changes in the input
 635 observations. The quality of a given type of measurement is also not necessarily uniform in
 636 time; for example, virtually all radiosonde sites have adopted different instrument packages
 637 over time (see section 2.4.2.1), while TOVS and ATOVS data were collected using several
 638 different sounders on several different satellites with availability that changed over time (see
 639 Figure 2-11 and section 2.4.2.2). Finally, Figures 2-7 through 2-10 show that, although
 640 modern reanalysis systems assimilate observations from many common sources, different
 641 reanalysis systems assimilate different subsets of the available observations. Such
 642 discrepancies are particularly pronounced for certain categories of satellite observations and,
 643 like differences in the underlying forecast models, are an important potential source of inter-
 644 reanalysis differences.

645
 646 Table 2-15. List of codes/acronyms for selected observations assimilated by reanalysis
 647 systems.

SYNOP (conventional)	Surface meteorological observation reported by manned and automated weather stations.
-----------------------------	---

SHIP (conventional)	Surface meteorological observations reported by ships.
----------------------------	--

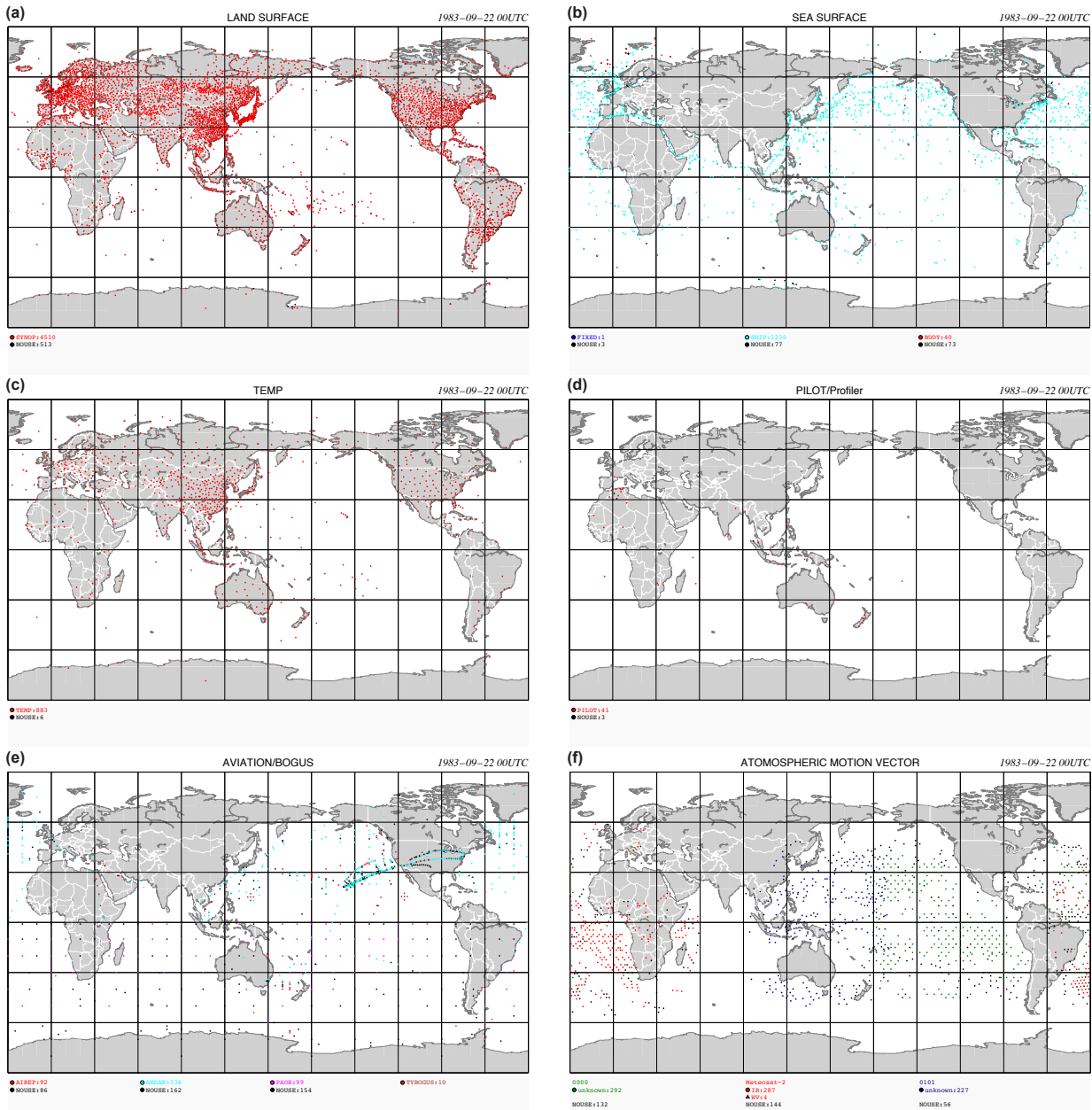
BUOY (conventional)	Surface meteorological observations reported by buoys.
PAOBS (conventional)	Surface pressure bogus data for the southern hemisphere. This is a product of human analysts in the Australian Bureau of Meteorology who estimate sea level pressure based on satellite imagery, conventional data and temporal continuity.
AMV (satellite)	Atmospheric motion vectors derived by tracing the movement of individual cloud or water vapour features in successive images from geostationary and polar-orbiting satellites.

648

649

650

651

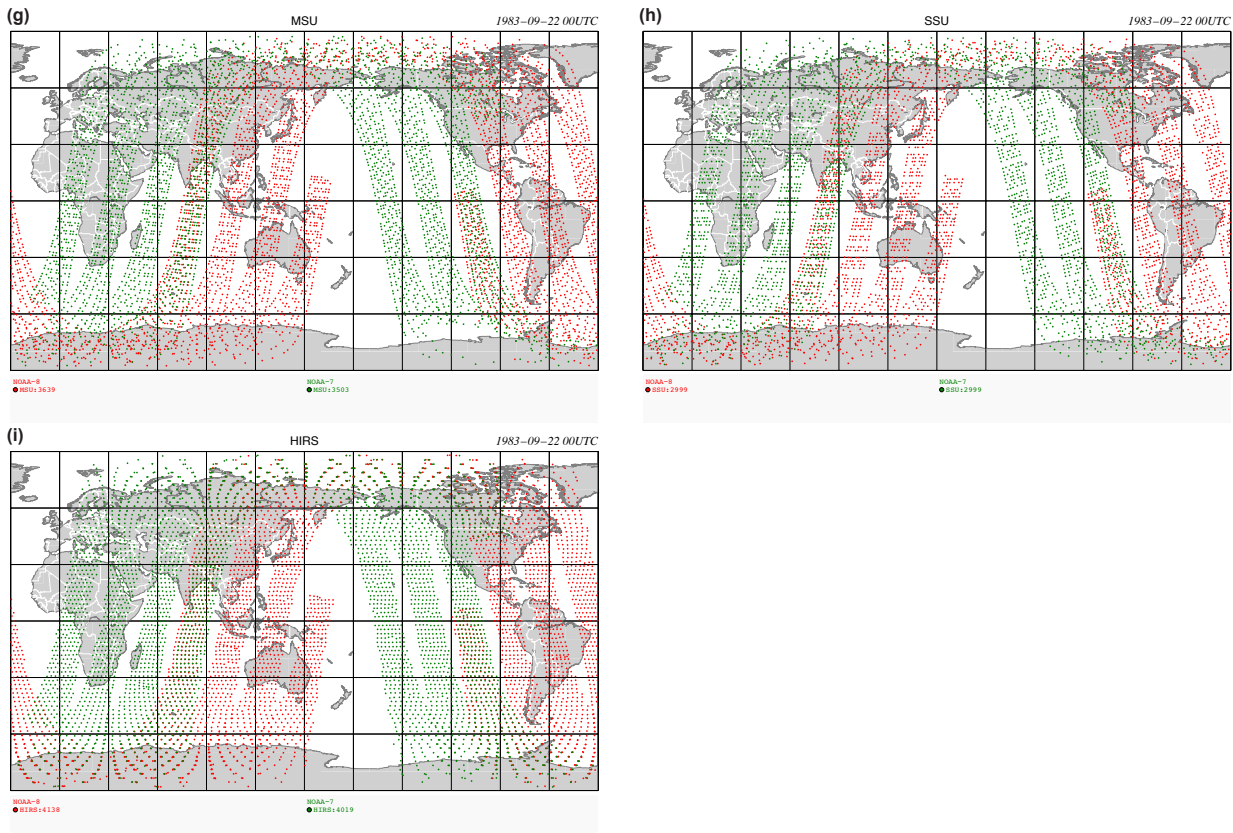


652

653 Figure 2-5. Observations assimilated by JRA-55 at 00UTC 22 September 1983 (± 3 hours):
 654 (a) land surface data, (b) sea surface data, (c) radiosonde profiles, (d) pilot balloons,
 655 (e) aircraft, PAOBS, and tropical cyclone wind retrievals, and (f) atmospheric motion vectors
 656 from METEOSAT, GMS, and GOES satellites.

657

658



659
660
661
662
663
664

Figure 2-5 (cont.) (g) Microwave temperature sounder radiances from NOAA satellites, (h) stratospheric temperature sounder radiances from NOAA satellites, and (i) infrared sounder radiances (sensitive to temperature and moisture) from NOAA satellites.

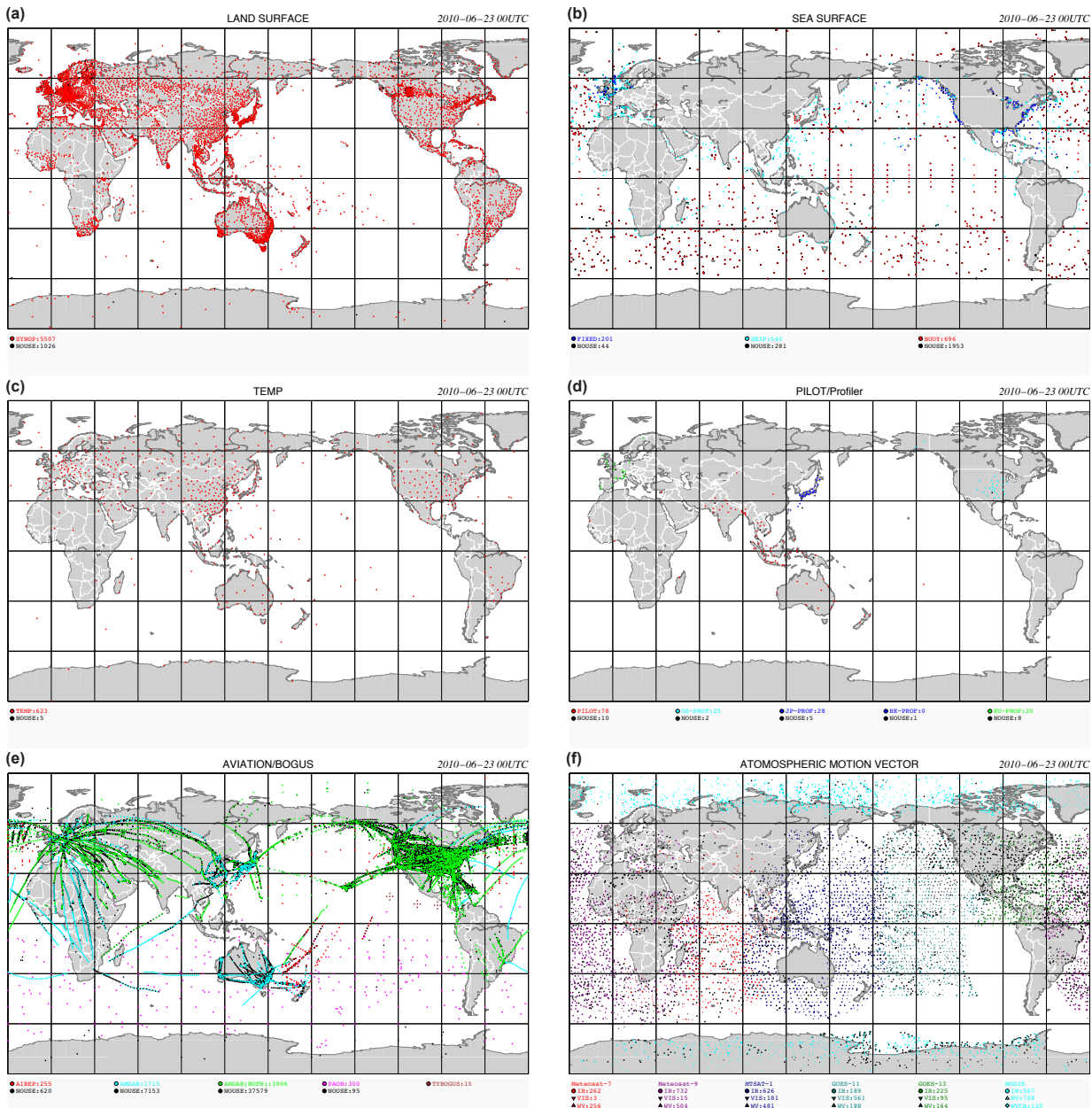
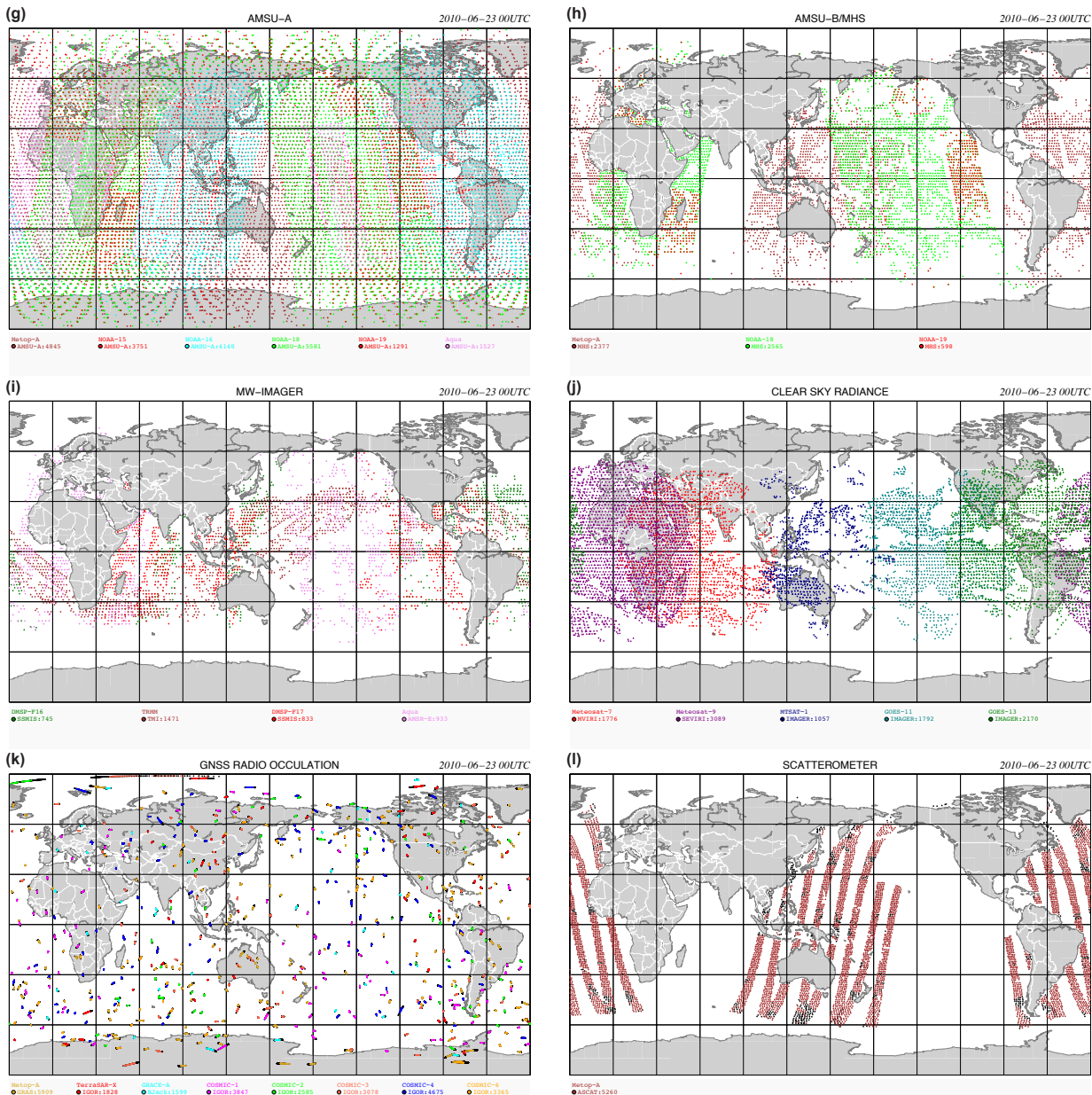
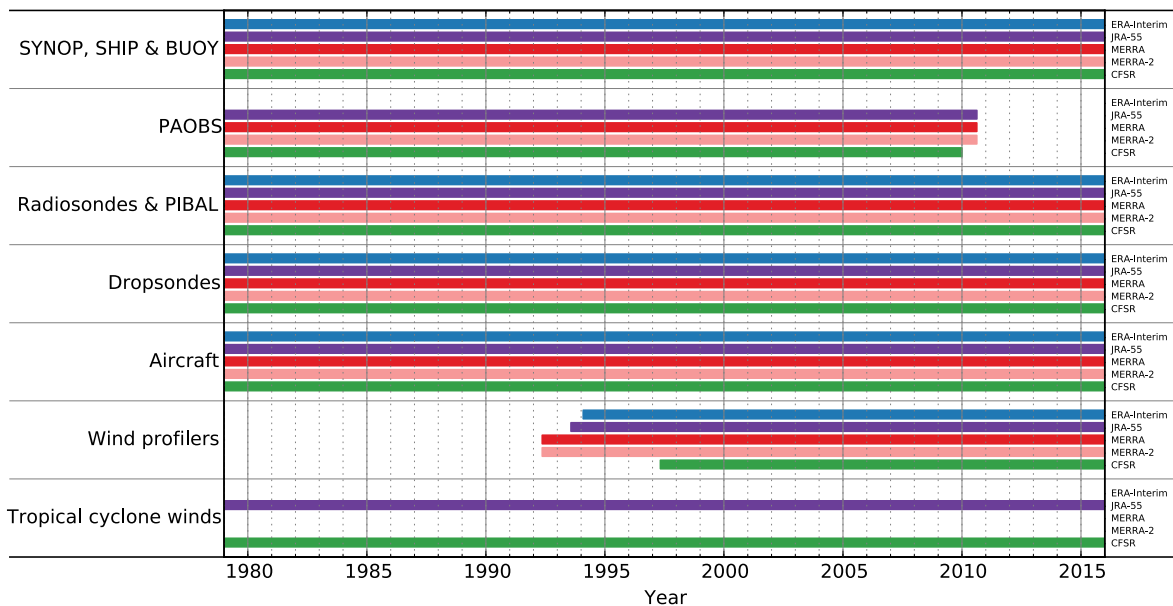


Figure 2-6. Observations assimilated by JRA-55 at 00UTC 23 June 2010 (± 3 hours): (a) land surface data, (b) sea surface data, (c) radiosonde profiles, (d) pilot balloons and wind profilers, (e) aircraft, PAOBS, and tropical cyclone wind retrievals, and (f) atmospheric motion vectors from the METEOSAT, MTSAT, GOES, Aqua, and Terra satellites.



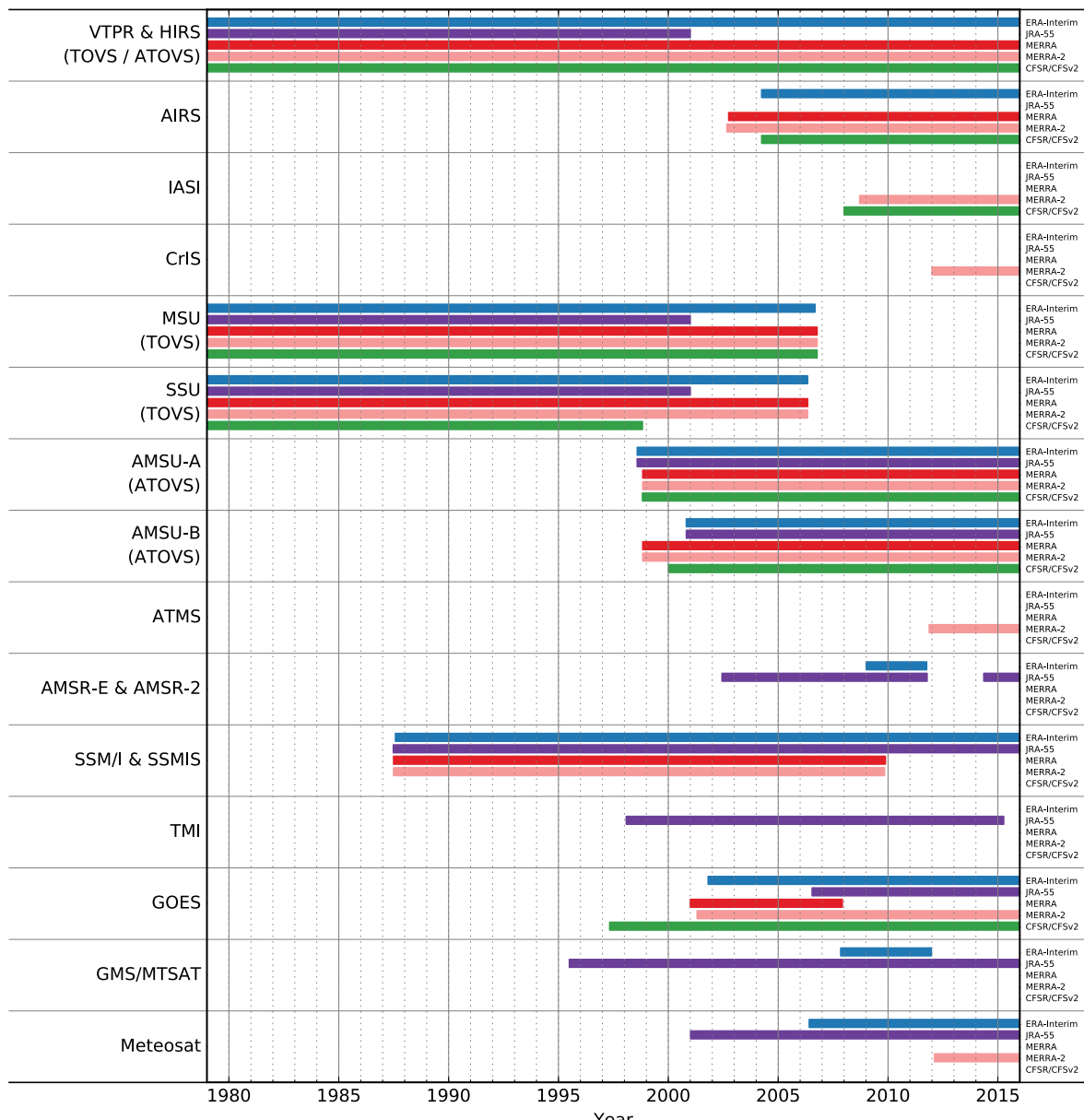
672
673
674
675
676
677
678
679
680
681

Figure 2-6 (cont.) (g) microwave temperature sounder radiances from the NOAA, MetOp, and Aqua satellites, (h) microwave humidity sounder radiances from NOAA and MetOp satellites, (i) microwave imager radiances (sensitive to moisture) from the DMSP, TRMM, and Aqua satellites, (j) clear-sky radiances from METEOSAT, MTSAT, and GOES satellites, (k) GNSS-RO refractive index data (sensitive to temperature and moisture) from the COSMIC, GRACE, MetOp, and TerraSAR-X satellites, and (l) ocean surface winds from MetOp (ASCAT scatterometer).



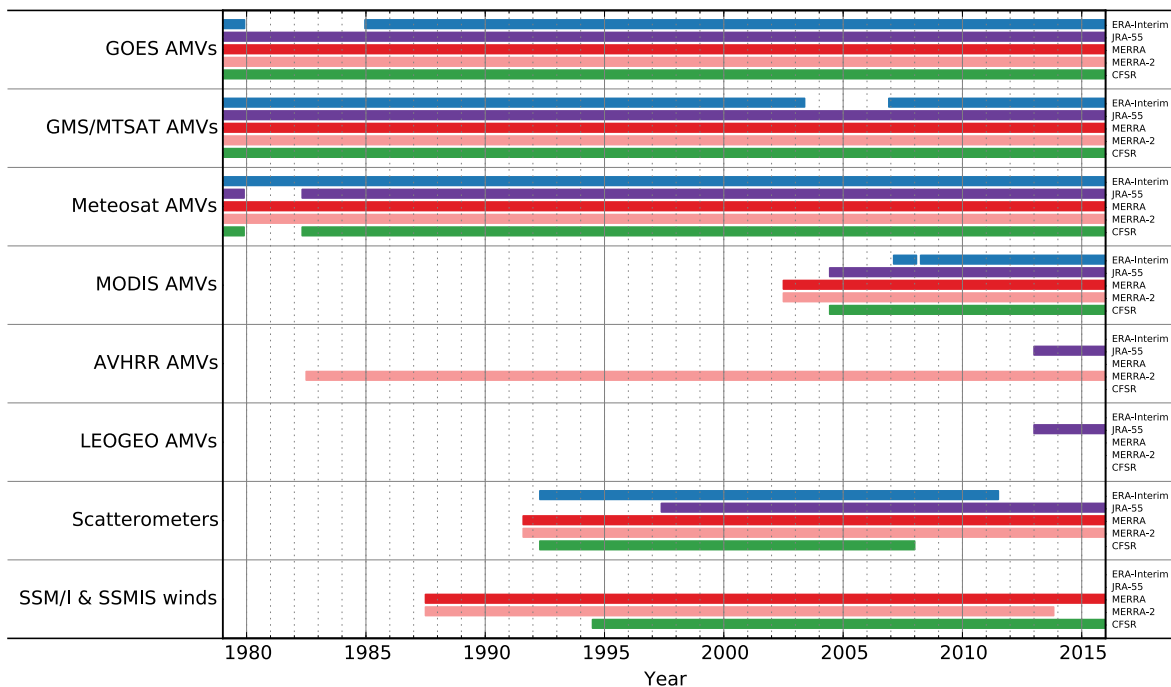
682
683
684
685
686
687
688

Figure 2-7. Availability of conventional observations assimilated by ERA-Interim (blue), JRA-55 (purple), MERRA (dark red), MERRA-2 (light red), and CFSR (green) reanalysis systems as a function of time. See Table 2-15 and Appendix A for acronym definitions.

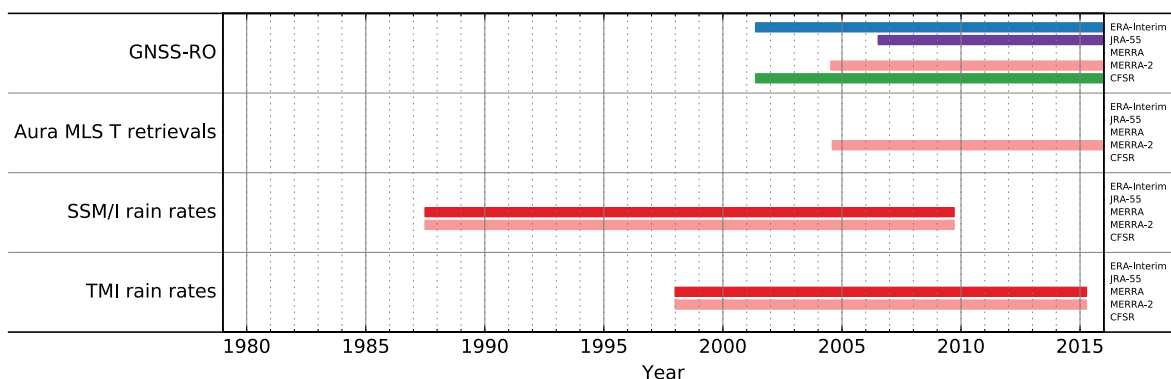


689
690
691
692

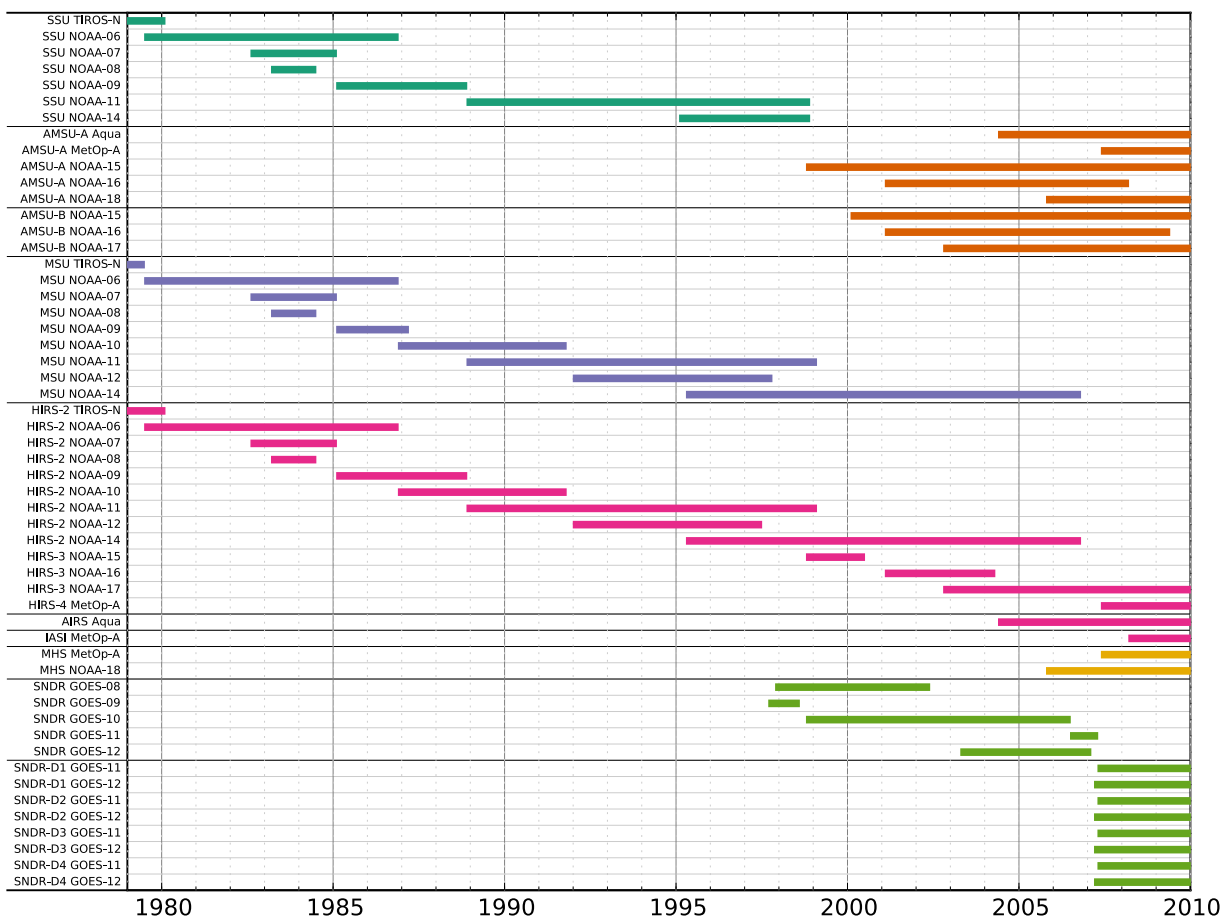
Figure 2-8. As in Figure 2-7, but for satellite radiances assimilated by the reanalysis systems.



693
694 Figure 2-9. As in Figure 2-7, but for AMVs and ocean surface wind products derived from
695
696
697
698
satellites and assimilated by the reanalysis systems.



699
700 Figure 2-10. As in Figure 2-7, but for other types of satellite observations assimilated by the
701
702
703
704
reanalysis systems. Timelines of satellite retrievals of total column ozone and ozone profiles
assimilated by the reanalysis systems are provided in Chapter 4 of this report (Figures 4-1
and 4-2).



705
706 Figure 2-11. Availability of satellite instruments with radiances assimilated by CFSR as a
707 function of time. Adapted from Saha et al. (2010).
708
709
710

711 Timelines of conventional data assimilated by reanalyses are quite consistent among modern
712 full input reanalyses (Figure 2-7), as well as the conventional input JRA-55C (not shown).
713 All of the reanalysis systems discussed in this chapter assimilate records of surface pressure
714 from manned and automated weather stations, ships, and buoys, while all but 20CR
715 assimilate at least some records of surface winds over oceans. All but ERA-Interim, ERA-
716 20C, 20CR, and JRA-55C assimilated synthetic surface pressure data for the Southern
717 Hemisphere (PAOBS) through at least 2009. PAOBS are subjective analyses of surface
718 pressure produced by the Australian BOM based on available observations and temporal
719 continuity, which are used to compensate for the scarcity of direct observations in the
720 Southern Hemisphere. The influence of these data in reanalysis systems has waned in recent
721 years, as the availability of direct observations covering the Southern Hemisphere has
722 expanded. All of the full input reanalyses and JRA-55C assimilate upper-air observations
723 made by radiosondes, dropsondes, and wind profilers. JRA-25, JRA-55, and JRA-55C
724 assimilate wind speed profiles in tropical cyclones, while 20CR assimilates records of
725 tropical cyclone central pressures. CFSR uses the NCEP tropical storm relocation package
726 (Liu et al., 1999) to relocate tropical storm vortices to observed locations. ERA-40, ERA-
727 Interim, MERRA, MERRA-2, NCEP-NCAR R1 and NCEP-DOE R2 have no special
728 treatment for tropical cyclones.
729

730 Timelines of satellite data assimilated by current reanalysis systems are more varied
 731 (Figures 2-8 through 2-10; see also Figures 4-1 and 4-2), but still include many
 732 commonalities. The core satellite data assimilated by most reanalyses are microwave and
 733 infrared radiances from a variety of instruments. All of the full input reanalyses (including
 734 NCEP-NCAR R1 and NCEP-DOE R2) also assimilate atmospheric motion vector (AMV)
 735 data derived from geostationary and polar-orbiting satellite imagery. Many of the more
 736 recent systems assimilate GNSS-RO data, while MERRA-2 assimilates temperature
 737 retrievals from Aura MLS at pressures 5 hPa and less. Timelines of satellite ozone retrievals
 738 assimilated by reanalyses are discussed in Chapter 4 of this report (Figures 4-1 and 4-2).
 739

740 Table 2-16 lists special features of each reanalysis system regarding observational data
 741 assimilated. Note that NCEP-NCAR R1 and NCEP-DOE R2 assimilated temperature
 742 retrievals from microwave and infrared sounders (e.g., Reale, 2001), while the other
 743 reanalysis systems (except for 20CR) assimilated radiance observations directly.
 744
 745
 746

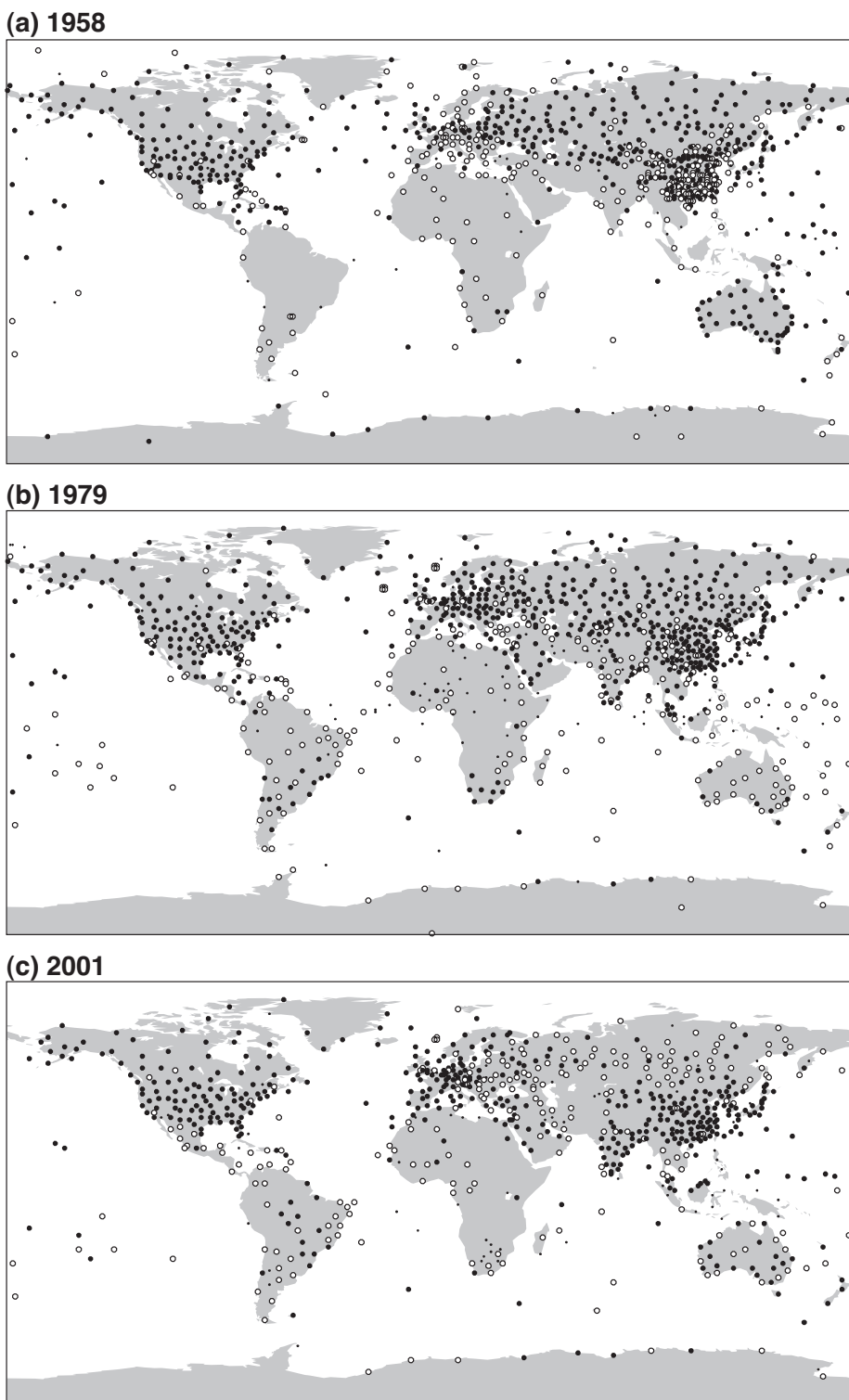
747 Table 2-16. Special features regarding observational data assimilated in each reanalysis
 748 system (see also Figures 2-7 through 2-10 for the five most recent full input reanalyses).

ERA-40	SSM/I total column water vapor and surface wind retrievals were assimilated.
ERA-Interim	GNSS-RO bending angles and AIRS radiances are assimilated. Unlike ERA-40, SSM/I radiances are assimilated directly (in place of TCWV and surface wind retrievals).
ERA-20C	ERA-20C assimilated surface pressure observations from ISPD (Cram et al. 2015) and surface pressure and surface wind observations from ICOADS (Woodruff et al., 2011). Reports that appear in both the ISPD and ICOADS databases are taken from ICOADS, with the ISPD report discarded.
JRA-25 / JCDAS	SSM/I total column water vapor retrievals were assimilated, as were wind profile retrievals in tropical cyclones.
JRA-55	GNSS-RO refractivity data are assimilated, as are wind profile retrievals in tropical cyclones.
MERRA	AIRS radiances are assimilated, as are rain rates from SSM/I and TMI.
MERRA-2	GNSS-RO bending angles are assimilated up to 30 km. AIRS radiances are assimilated, as are hyperspectral radiances observed by IASI, CrIS and ATMS. Version 3.3 MLS temperature retrievals are assimilated above 5 hPa. An adaptive bias correction scheme is applied to aircraft observations. Assimilated aerosol optical depths are also bias-corrected. Rain rates from SSM/I and TMI and satellite observations of AOD are assimilated.
NCEP-NCAR R1	Temperature retrievals from microwave and infrared sounders are assimilated, rather than radiances. The horizontal and vertical resolutions of temperature retrievals are downgraded to reduce the weight given to satellite data in recent analyses. Satellite moisture retrievals and SSM/I surface winds are not assimilated.
NCEP-DOE R2	Temperature retrievals from microwave and infrared sounders are assimilated, rather than radiances. The horizontal and vertical

	resolutions of temperature retrievals are downgraded to reduce the weight given to satellite data in recent analyses. Satellite moisture retrievals and SSM/I surface winds are not assimilated.
CFSR / CFSv2	GNSS-RO bending angles and AIRS radiances are assimilated. The NCEP tropical storm relocation package is applied to relocate tropical storm vortices to observed locations.
NOAA-CIRES 20CR v2	Only observations of surface pressure, sea level pressure, and tropical cyclone central pressure were assimilated. No upper-air or satellite data were assimilated.

749
750
751752 **2.4.2 Summary of key upper air observations and known issues**

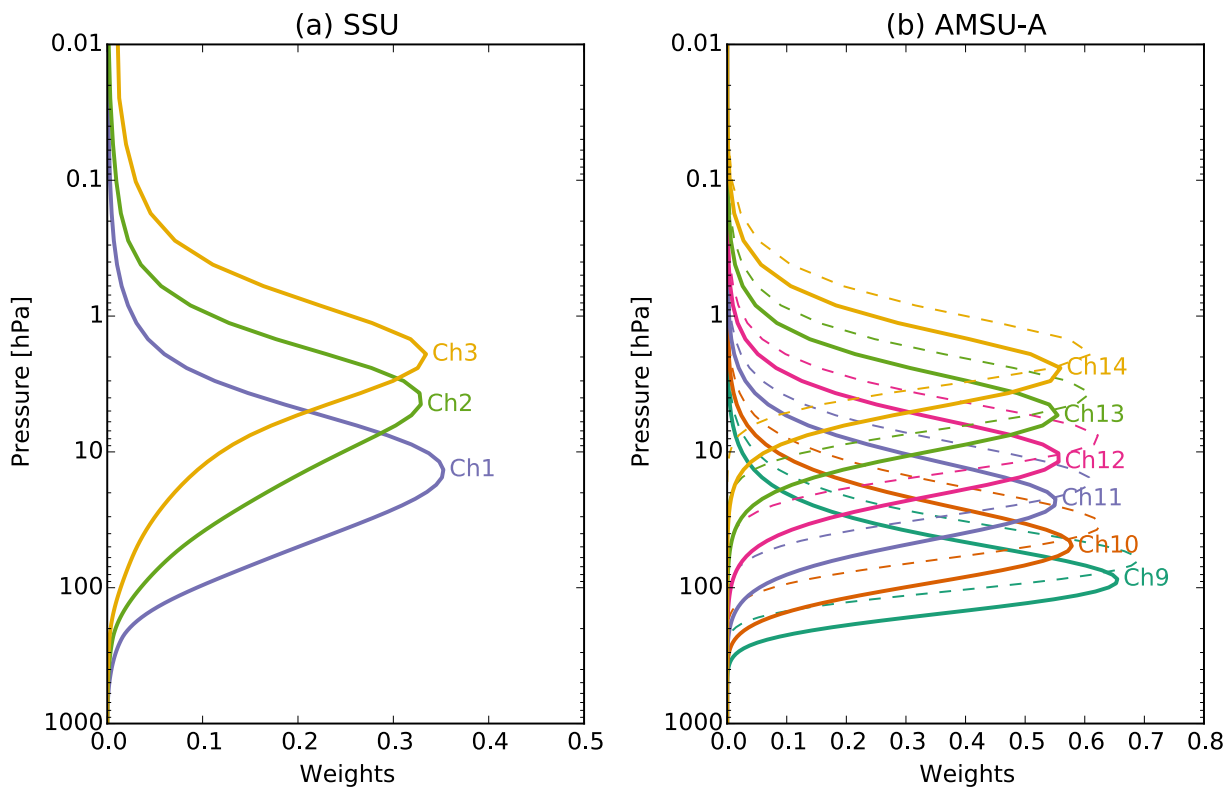
753 This section discusses a selection of upper air observational data that are assimilated in one
 754 or more of the reanalysis systems and are key for SPARC sciences. Radiosondes provide
 755 high vertical resolution profiles of temperature, horizontal wind, and humidity worldwide;
 756 however, most radiosonde stations are located in the Northern Hemisphere at middle and
 757 high latitudes over land (Figure 2-12). The typical vertical coverage of radiosonde data
 758 extends from the surface up to ~30 hPa for temperature and wind and from the surface up to
 759 300~200 hPa for humidity. Operational satellite radiance measurements provide constraints
 760 for temperature and moisture with more homogeneous spatial coverage, but at the cost of
 761 deep vertical weighting functions (e.g., Figure 2-13). Moreover, the majority of these
 762 measurements were not available before 1978. Both observing systems have known biases,
 763 as well as jumps and drifts in the time series that may cause the quality of reanalysis
 764 products to change over time. Bias corrections prior to and/or within the assimilation step
 765 are therefore essential for creating more reliable reanalysis products. In addition to
 766 radiosonde and satellite data, atmospheric motion vector (AMV) data created from
 767 geostationary and polar-orbiter satellite images and wind and temperature observations
 768 collected by aircraft are influential in the upper troposphere and lower stratosphere.
 769
 770
 771



772

773 Figure 2-12. Frequency of radiosonde reports assimilated by ERA-40 during (a) 1958, (b)
774 1979, and (c) 2001. Solid circles denote stations reporting three times every 2 days on
775 average, open circles denote stations reporting at least once every 2 days, and small dots
776 denote stations reporting at least once per week (from Uppala et al., 2005). ©Royal
777 Meteorological Society. Used with permission.
778
779

780



781

782

783

784

785

786

787

788

789

Figure 2-13. Vertical weighting functions of radiance measurements for (a) the Stratospheric Sounding Unit (SSU) instrument (1979–2005) channel 1 (centred at ~15 hPa), channel 2 (~5 hPa), and channel 3 (~1.5 hPa), and (b) the Advanced Microwave Sounding Unit A (AMSA) instrument (1998–present) temperature channels 9–14 at near nadir (1.67° , solid lines) and limb (48.33° , dashed lines) scan positions.

790

2.4.2.1 Radiosonde data

791

792

793

794

795

796

797

798

799

800

801

802

803

804

805

806

The main source of systematic errors in radiosonde temperature measurements is the effects of solar radiative heating and (to a lesser extent) infrared cooling on the temperature sensor (Nash et al., 2011). This issue, which is sometimes called the “radiation error”, can cause particularly pronounced warm biases in raw daytime stratospheric measurements. These biases may be corrected onsite in the ground data receiving system before reporting, and further corrections may be applied at each reanalysis centre before assimilation. The major issue with radiosonde humidity measurements is that the sensor response is too slow at cold temperatures (Nash et al., 2011). Recent advances in radiosonde instrumentation are beginning to improve this issue, particularly in the upper troposphere; however, radiosonde observations of humidity at pressures less than 300 hPa are typically not assimilated by reanalysis systems. Other issues include frequent (and often undocumented) changes in radiosonde instrumentation and observing methods at radiosonde stations, which may cause jumps in the time series of temperature and relative humidity. Several “homogenization” activities for radiosonde temperature data exist to support climate monitoring and trend analyses (see, e.g., Seidel et al., 2009). Although some of these activities have been effectively independent of reanalysis activities, cooperation between the two groups has

807 increased substantially in recent years. Particularly notable is the production of
 808 RAOBCORE (Haimberger et al., 2008, 2012), which was conducted with reanalysis
 809 applications in mind. One or more versions of RAOBCORE are used in ERA-Interim (v1.3),
 810 MERRA and MERRA-2 (v1.4 through 2005), and JRA-55 (v1.4 through 2005; v1.5
 811 thereafter). Further efforts on data rescue, reprocessing, homogenization, and uncertainty
 812 evaluation by the broader research community are likely to be an essential part of the next
 813 generation of reanalyses (e.g., ACRE and GRUAN; Allan et al., 2011; Bodeker et
 814 al., 2016).

815
 816 The following example describes a “homogenization” (or bias correction) of radiosonde
 817 temperature measurements for assimilation in a reanalysis system:

- 818 (1) Radiosonde temperatures are corrected for estimated biases from 1980 onwards;
- 819 (2) Stations are separated into groups representing different countries or regions
 (because stations within the same country often use the same type of radiosonde
 from the same manufacturer);
- 820 (3) Mean differences between background forecasts and observations are accumulated
 for each group of stations;
- 821 (4) The mean error for all groups is subtracted from the bias computed for each group to
 provide a correction for radiation effects;

822 This approach corrected for many daily and seasonal variations of the biases but did not
 823 account for variations in annual mean biases. Radiosonde temperature measurements
 824 homogenized using this approach were assimilated in both ERA-40 and JRA-25 (Andrae et
 825 al., 2004; Uppala et al., 2005; Onogi et al., 2007). The homogenizations applied to produce
 826 the RAOBCORE temperatures assimilated by many later reanalyses (including ERA-Interim,
 827 JRA-55, MERRA, and MERRA-2, as discussed above) have been conducted using updated
 828 versions of this procedure. Although radiosonde humidity measurements are also known to
 829 suffer from biases, current reanalysis systems do not include schemes to correct for biases in
 830 radiosonde humidities.

831 Major quality control criteria for radiosonde profiles (and other conventional data) include
 832 checks for completeness, physical and climatological consistency, and duplicate reports.
 833 Data may also be filtered using locally compiled blacklists or blacklists acquired from other
 834 data providers and reanalysis centres. Further information on the quality control criteria
 835 applied by different reanalysis is available in the text and supporting material of the
 836 publications listed in Table 2-1.

837 Radiosonde and other upper-air in situ data are also often shared among different reanalysis
 838 centres. For example, Rienecker et al. (2011) listed the sources for historical radiosonde,
 839 dropsonde, and PIBAL data used by MERRA as:

- 840 (1) NCEP–NCAR: Office Note 20, Office Note 29, NMC/NCEP/GTS ingest;
- 841 (2) ECMWF: ECMWF/FGGE, ECMWF/MARS/GTS ingest;
- 842 (3) JMA: Japan Meteorological Agency GTS ingest;
- 843 (4) NCAR: International archives from Argentina, Australia, Brazil, Canada, China,
 Dominica, France, India, Japan, NCDC, New Zealand, Russia, Singapore, South
 Africa, United Kingdom Research sets: PermShips, RemoteSites, Ptarmigan,
 Scherhaug, LIE, GATE and BAS;
- 844 (5) NCDC: U.S. military and academic sources, including TD52, TD53, TD54, TD90,
 USCNTRL, USAF, U.S. Navy, CCARDS and MIT.

845 These data sources overlap substantially with those used in ERA-40 and ERA-Interim
 846 (Uppala et al., 2005, their Appendix B; Tavolato and Isaksen, 2010), JRA-25 and JRA-55

(Onogi et al., 2007, their section 2.1a; Kobayashi et al., 2015, their Table A1), MERRA-2 (McCarty et al., 2016), NCEP-NCAR R1 (Kalnay et al., 1996, their Section 3a), and CFSR (Saha et al., 2010, their section “Conventional observing systems in the CFSR”); however, individual reanalyses may supplement standard data sets with data from unique sources. A detailed intercomparison of the conventional data used in each reanalysis is beyond the scope of this chapter; however, we note that at least four of the reanalyses (ERA-40, ERA-Interim, JRA-25, and JRA-55) use the ERA-40 ingest as a starting point, and that the ERA-40 ingest has much in common with the conventional data archives used by NCEP (R1, R2, and CFSR) and the NASA GMAO (MERRA and MERRA-2). More recent updates in data holdings at ECMWF, JMA, GMAO, and NCEP rely heavily on near-real-time data gathered from the WMO GTS, which also contributes to the use of a largely (but not completely) common set of conventional data among reanalysis systems.

869
870
871

872 2.4.2.2 Satellite data

873 Reanalysis systems assimilate data from several different types of satellite instruments, most
874 notably the microwave and infrared sounders in the TOVS suite (1979–2006 on several
875 satellites) and the ATOVS suite (1998–present on several satellites). The TOVS suite
876 included the Stratospheric Sounding Unit (SSU), the Microwave Sounding Unit (MSU), and
877 the High resolution Infrared Sounder-2 (HIRS/2). The ATOVS suite includes the Advanced
878 MSU-A (AMSU-A) and HIRS/3 (updated to HIRS/4 starting with NOAA-18). NCEP-
879 NCAR R1 and NCEP-DOE R2 assimilate temperature retrievals from these instruments (see,
880 e.g., Reale, 2001). All of the other full input reanalyses described in this chapter assimilate
881 microwave and infrared radiances from the TOVS and ATOVS suites. ERA-Interim,
882 MERRA, MERRA-2, and CFSR also assimilate radiances from AIRS, the first hyperspectral
883 infrared sounder with data assimilated in reanalyses (2002–present). MERRA-2 and CFSR
884 assimilate hyperspectral infrared radiances from IASI (2008–present), while MERRA-2 also
885 assimilates radiances from the hyperspectral infrared sounder CrIS and the most recent
886 generation of microwave sounder ATMS (late 2011–present). ERA-Interim, JRA-55,
887 MERRA-2, and CFSR assimilate data from GNSS-RO instruments (CHAMP: 2001–2008;
888 FORMOSAT-3/COSMIC: 2006–present; MetOp-A: 2008–present), in the form of bending
889 angles (ERA-Interim, MERRA-2 and CFSR) or refractivity at the tangent point (JRA-55)
890 rather than temperature or water vapour retrievals.
891

892 Satellite sounding instruments often have several channels with different vertical weighting
893 functions (see, e.g., Figure 2-13). Even when using the same satellite instrument, different
894 reanalysis systems may assimilate data from different sets of channels. Bias corrections and
895 quality control criteria for satellite radiances may also vary by channel. Table 2-17 lists
896 details of satellite data usage for five of the full input reanalysis systems considered in this
897 chapter.
898
899
900
901
902
903

904 Table 2-17. Overview of satellite data usage in five of the most recent full input reanalysis
 905 systems. Adapted and updated from <http://reanalyses.org/observations/satellite-1>. Refer to
 906 the website for source information and the latest version of this table (including information
 907 for JRA-25/JCDAS). See Appendix A for acronym definitions.

Instrument (observable)	CFSR / CFSv2	MERRA	MERRA-2	JRA-55	ERA-Interim
MSU (radiances)	Channels 1,2,3,4 Notes: NESDIS SNO corrected calibration coefficients applied (NOAA-10 to -14) Exclusions: <ul style="list-style-type: none">• More restrictive QC in tropics and over high terrain• Window test ch. 2	Channels 1,2,3,4 Notes: NESDIS SNO corrected calibration coefficients applied Exclusions: <ul style="list-style-type: none">• Snow, ice, mixed surfaces for ch. 1–2	Channels 2,3,4 Notes: NESDIS SNO corrected calibration coefficients applied Exclusions: <ul style="list-style-type: none">• Restrictive QC over snow, ice and mixed surfaces• Observation errors inflated over non-water surfaces	Channels 2,3,4 Exclusions: <ul style="list-style-type: none">• Land or rain for ch. 2• Land for ch. 3	Channels 2,3,4 Exclusions: <ul style="list-style-type: none">• Land or rain for ch. 2• Land for ch. 3
AMSU-A (radiances)	Channels 1–13, 15 Exclusions: <ul style="list-style-type: none">• Estimated cloud liquid water large for ch. 1–5, 15• Scattering index large for ch. 1–6, 15• Ch. 4 gross check large for ch. 1–5, 15• Ch. 6 gross check large for ch. 1–6, 15• High terrain for ch. 1–5, 15• Fit to emissivity or surface temp large for ch. 1–5, 15	Channels 1–15 Exclusions: <ul style="list-style-type: none">• Snow, ice, mixed surfaces for ch. 1–6, 15• No offset bias correct for ch. 14	Channels 4–14 Exclusions: <ul style="list-style-type: none">• Restrictive QC• Observation errors inflated for ch. 4–6 over non-water surfaces	Channels 4–14 Exclusions: <ul style="list-style-type: none">• Sea ice or land for ch. 4–5• High terrain for ch. 6–7• Rain for ch. 4–8	Channels 5–14 Exclusions: <ul style="list-style-type: none">• High terrain for ch. 5–6• Rain for ch. 5–7• No offset bias correct for ch. 14
AMSU-B / MHS (radiances)	Channels 1–5 Exclusions: <ul style="list-style-type: none">• Scattering index too large• Channel 1 fit too large• Any channel failing gross check• High terrain	Channels 1–5 Exclusions: <ul style="list-style-type: none">• Snow, ice, mixed surfaces for ch. 1, 2, 5	Channels 1–5 Exclusions: <ul style="list-style-type: none">• Restrictive gross check• Observation errors inflated for all channels over non-water surfaces	Channels 3–5 Exclusions: <ul style="list-style-type: none">• Land, sea-ice, rain	Channels 3–5 Exclusions: <ul style="list-style-type: none">• Sea ice, rain, high terrain for ch. 3–4• Land for ch. 5
SSM/I (radiances)		Channels 1–7 Exclusions: <ul style="list-style-type: none">• Land	Channels 1–7 Exclusions: <ul style="list-style-type: none">• All non-water surfaces	Channels 1,3,4,6 Exclusions: <ul style="list-style-type: none">• Land, rain	Channels 1–7 Exclusions: <ul style="list-style-type: none">• Land, rain
HIRS (radiances)	Channels 2–15 Exclusions: <ul style="list-style-type: none">• Over water wavenumbers > 2400 during day• High terrain• Above model top• Channels without signal over clouds• Surface sensing channels with large difference.	Channels 2–15 Exclusions: <ul style="list-style-type: none">• Land for ch. 5–8	Channels 2–12 Exclusions: <ul style="list-style-type: none">• Surface-sensitive channels• Observation errors inflated over non-water surfaces	Ch. 2–7,11,12,14,15 Exclusions: <ul style="list-style-type: none">• Land for ch. 4–7, 11,14,15• High terrain for ch. 12• Clouds for ch. 3 and above	Ch. 2–7,11,12,14,15 Exclusions: <ul style="list-style-type: none">• Clouds, land for ch. 4–7,11,14,15• High terrain for ch. 12
SSU (radiances)	Channels 1–3 Notes: <ul style="list-style-type: none">• All channels bias-corrected.	Channels 1–3 Notes: <ul style="list-style-type: none">• No offset bias correction for ch. 3	Channels 1–3 Notes: <ul style="list-style-type: none">• Only ch. 1–2 after onset of NOAA-15 AMSU-A (1 Nov 1998)• No offset bias correction for ch. 3	Channels 1–3	Channels 1–3 Notes: <ul style="list-style-type: none">• No offset bias correction for ch. 3
GEO	GOES sounder	GOES sounder	GOES, Meteosat	GOES,	GOES,

(radiances)	Notes: • $5^\circ \times 5^\circ$ 1993–2007 • $1^\circ \times 1^\circ$ 2007–present		(after early 2012)	METEOSAT, GMS, MTSAT imagers	METEOSAT, MTSAT imagers
SSM/I (retrievals)	• Surface wind speed over oceans	• Surface wind speed over oceans • Rain rate	• Surface wind speed over oceans • Rain rate	• Snow cover	• Total column water vapor (rainy areas over oceans)
Imager (upper-air winds)	GOES, METEOSAT, GMS, MTSAT, MODIS	GOES, METEOSAT, GMS, MTSAT, MODIS	GOES, METEOSAT, GMS, MTSAT, MODIS	GOES, METEOSAT, GMS, MTSAT, MODIS	GOES, METEOSAT, GMS, MTSAT, MODIS
Scatterometer (winds over ocean surface)	ERS, Quikscat, ASCAT	ERS, Quikscat	ERS, Quikscat, ASCAT	ERS, Quikscat, ASCAT	ERS, Quikscat
Ozone sensors (retrievals)	SBUV V8 retrievals	SBUV V8 retrievals	SBUV V8 retrievals, OMI, MLS (v2.2 switching to v4.2 after June 2015)	TOMS, OMI (nudging)	TOMS, SBUV, GOME, MIPAS, SCIAMACHY, MLS, OMI
Other notable elements	• AIRS • IASI • GNSS-RO • AMSR-E • Reprocessed ERS • Reprocessed GMS • AMSU-B (NOAA-15 only)	• TMI rain rate • AIRS • NOAA-15 AMSU-B	• TMI rain rate • AIRS • IASI • CrIS • GNSS-RO • NOAA-15 AMSU-B • ATMS • SEVIRI • MLS temperature retrievals (v3.3) above 5 hPa • AOD from MISR, MODIS, AVHRR and AERONET	• Reprocessed winds from GMS, GOES-9, MTSAT (revised) and METEOSAT • Reprocessed radiances from GMS, GOES-9, MTSAT • TMI (NASA) • AMSR-E (JAXA) • GNSS-RO • SSM/I-S • VTPR • Exclude HIRS from NOAA-15 and later	• GNSS-RO • AIRS • SSM/I-S • AMSR-E • HIRS NOAA-18

908

909

910 Radiances observed by the SSU instruments, which covered the period 1979–2005, represent an important archive of stratospheric temperatures (e.g., Wang et al., 2012; Zou et al., 2014; Nash and Saunders, 2015) and serve as a useful illustration of the types of issues that may be encountered in assimilating satellite data. The SSU is a pressure-modulated radiometer with an onboard CO₂ cell for spectral filtering at 15 μm. The calibration of SSU radiances is affected by the following known issues:

- 916 (1) Space-view anomalies due to electrical interference;
- 917 (2) CO₂ gas leakage and cell pressure changes;
- 918 (3) Changes in atmospheric CO₂ concentrations;
- 919 (4) Satellite orbital drift and diurnal sampling biases;
- 920 (5) Short overlap periods between successive instruments.

921 Raw radiance data from SSU include drifts and jumps in the time series due to these issues (e.g., Figure 2-14), which must be accounted for in the data assimilation system. Drifts and jumps of this type are not unique to SSU, and other long-term satellite radiance archives are also affected by issues specific to individual instruments. For example, Simmons et al. (2014; their Figure 13) have shown that estimated biases for certain MSU, HIRS, and AMSU-A channels can be of similar orders of magnitude to those for SSU, while trends in atmospheric CO₂ concentrations also cause long-term drifts in estimated biases for HIRS, AIRS, and IASI radiances. Biases in radiances observed by MSU and AMSU-A can be attributed mainly to inaccurate calibration offsets and non-linearity (Zou et al., 2006).

930

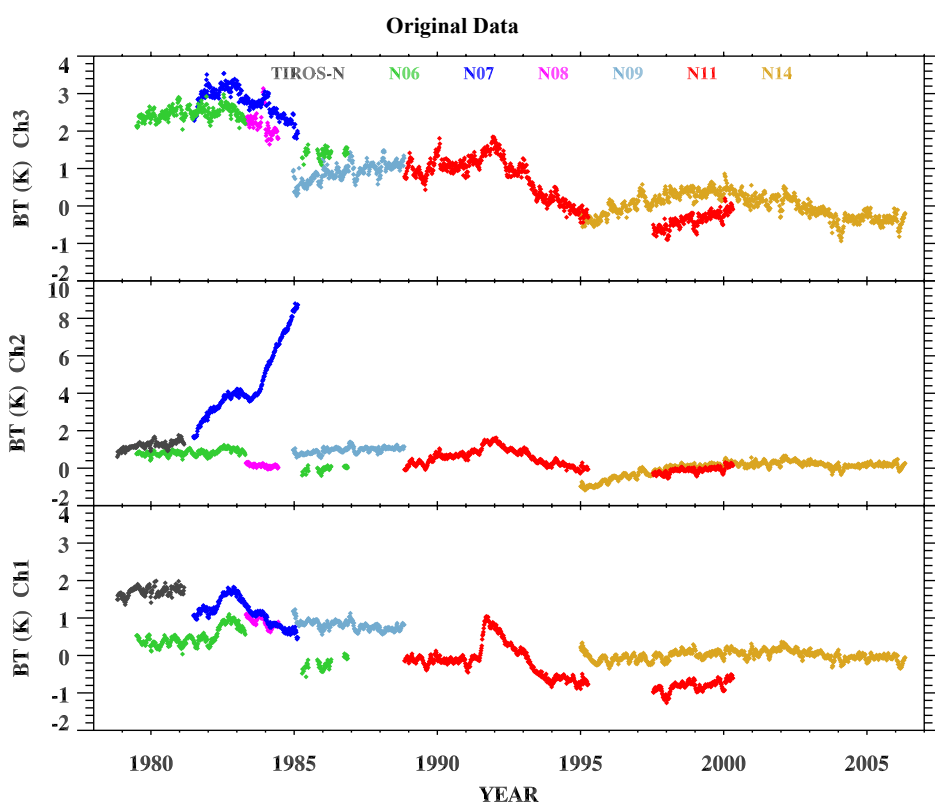
931

932 Post-launch inter-satellite calibration (or “homogenization”) efforts by the satellite remote sensing community, such as the WMO GSICS (Goldberg et al., 2011) have substantially

933 reduced inter-satellite differences in some cases, including MSU (Zou et al., 2006), AMSU-

934 A (Zou and Wang, 2011), and SSU (Zou et al., 2014). In practice, this type of inter-satellite
 935 calibration is usually performed by reanalysis systems internally via bias correction terms
 936 applied during the data assimilation step. It is therefore not strictly necessary for satellite
 937 data to be homogenized prior to its assimilation in a reanalysis system, although it is
 938 beneficial to assimilate data with biases as small as possible.
 939

940 The use of externally homogenized data has been found to improve some aspects of recent
 941 reanalyses. For example, homogenized MSU data (Zou et al., 2006) assimilated by CFSR,
 942 MERRA and MERRA-2 (Table 2-17) have been found to improve temporal consistency in
 943 bias correction patterns (Rienecker et al., 2011), and may have helped MERRA to produce a
 944 more realistic stratospheric temperature response following the eruption of Mount Pinatubo
 945 (Simmons et al., 2014). In situations where conventional data are unavailable or insufficient
 946 to provide a reference for satellite bias correction, such as SSU in the middle and upper
 947 stratosphere, homogenized radiance data may be even more effective in eliminating artificial
 948 drifts and jumps in the analysis state. Homogenized satellite radiance time series only
 949 represent a relatively small fraction of the satellite data ingested by current reanalysis
 950 systems (several of which do not assimilate homogenized data at all); however, the
 951 availability of homogenized satellite radiance time series is increasing and these data are
 952 likely to become more influential in future reanalysis efforts.
 953



954
 955 Figure 2-14. Global mean pentad brightness temperature anomalies based on raw SSU
 956 radiances from different satellites. Anomalies are calculated relative to the 1995–2005 mean
 957 NOAA-14 annual cycle (from Wang et al., 2012). ©American Meteorological
 958 Society. Used with permission.
 959
 960
 961

962 Bias corrections for assimilated satellite data often vary by satellite platform and/or
 963 reanalysis system. Although bias corrections are intended to limit the impacts of changing
 964 satellite biases within the reanalysis, these impacts may still manifest as spurious trends or
 965 discontinuities in the time series of temperature and other reanalysis variables. In older
 966 reanalyses that assimilated satellite radiances, such as ERA-40 and JRA-25, bias corrections
 967 were often (but not always) based on a fixed regression that spanned the lifetime of the
 968 instrument (Uppala et al., 2005; Onogi et al., 2007; Sakamoto and Christy, 2009). This
 969 approach, which occasionally required the reanalysis to be interrupted for manual retuning
 970 of bias correction terms, has been replaced by adaptive (or variational) bias correction
 971 schemes in recent reanalysis systems. Adaptive bias corrections for satellite radiances are
 972 based on differences between observed radiances and expected radiances calculated from
 973 model-generated background states. Some early implementations of adaptive bias
 974 corrections, such as that applied to TOVS data in JRA-25, left the reanalysis vulnerable to
 975 jumps and drifts inherited from the assimilated radiances (Sakamoto and Christy, 2009).
 976 These problems are addressed in the most recent reanalysis systems by defining
 977 observational “anchors” that are regarded as unbiased and are therefore allowed to
 978 contribute directly to the background state (Dee, 2005). A key example is the use of
 979 homogenized radiosonde data to anchor bias corrections for satellite radiances (e.g. Auligné
 980 et al., 2007). Versions of this approach have been implemented in ERA-Interim, JRA-55,
 981 MERRA, and MERRA-2. GNSS-RO observations (Section 5.3) are also useful for
 982 anchoring bias corrections (e.g. Poli et al., 2010), and have been used in this capacity in
 983 ERA-Interim, JRA-55, and MERRA-2; however, GNSS-RO data are only available after
 984 May 2001. The approach used in CFSR and CFSv2 (Derber and Wu, 1998; Saha et al.,
 985 2010) differs from that used in other systems, in that anchor observations are not used to
 986 adjust the background state prior to assimilation of satellite radiances. Instead, initial bias
 987 corrections are determined for each new satellite instrument via a three-month spin-up
 988 assimilation and then allowed to evolve slowly. The effects of satellite-specific drifts and
 989 jumps are kept small by assigning very low weights to the most recent biases between the
 990 observed and expected radiances, and by accounting for known historical variations in
 991 satellite performance as catalogued by multiple research centres. One byproduct of this
 992 procedure is an oscillating warm bias in CFSR in the upper stratosphere (see Chapter 3 of
 993 this report). This bias, which is intrinsic to the forecast model, largely disappears when a
 994 new execution stream is introduced, only to slowly return as the model bias is imprinted on
 995 the observational bias correction terms.
 996

997 A further example of the type of temporal discontinuities that can result from changes in
 998 satellite instrumentation is the cold bias (~2 K) in middle stratospheric temperature in JRA-
 999 25 between 1979 and 1998 (Onogi et al., 2007). This feature resulted from a known cold bias
 1000 in the radiative transfer model used by JRA-25. The SSU had only three channels sensitive
 1001 to stratospheric temperature (too few to correct the model bias). The AMSU-A instruments,
 1002 first launched in 1998, have more channels (i.e., higher vertical resolution) in the
 1003 stratosphere (see also Figure 2-13). Assimilation of the higher-resolution AMSU-A
 1004 radiances effectively corrected the model bias. The JRA-55 system uses an improved
 1005 radiative transfer model, and produces more realistic stratospheric temperatures during
 1006 1979–1998 (Ebita et al., 2011; Kobayashi et al., 2015).
 1007

1008 A final illustrative example concerns temperatures in the upper stratosphere. MERRA shows
 1009 artificial annual cycles in the upper stratosphere (Rienecker et al., 2011; their Figure 16),
 1010 which probably arise because the forward radiative transfer model used to assimilate SSU
 1011 radiances did not consider variations in atmospheric CO₂. These issues have been corrected

1012 in MERRA-2, which uses version 2.1.3 of the CRTM to assimilate SSU radiances. Several
 1013 reanalyses also show jumps in upper stratospheric temperature in or around 1998 (the sign
 1014 varies by vertical level and reanalysis) due to the introduction of AMSU-A, which includes
 1015 channels that peak higher in the stratosphere. See Chapter 3 of this report for further details
 1016 and additional examples.

1017
 1018
 1019

1020 **2.4.2.3 Aircraft data**

1021 Measurements made by aircraft, such as the AMDAR data collection, are influential inputs
 1022 in many atmospheric analyses and reanalyses (Petersen, 2016). Horizontal wind data from
 1023 aircraft are assimilated in all of the reanalysis systems but ERA-20C and 20CR, while
 1024 temperature data from aircraft are assimilated in all of the reanalysis systems except for
 1025 ERA-20C, JRA-55, JRA-25, and 20CR. In principle, aircraft data were assimilated from the
 1026 outset by ERA- 40 (September 1957; Uppala et al., 2005), JRA-55 (January 1958;
 1027 Kobayashi et al., 2015), and NCEP-NCAR R1 (January 1958; Kalnay et al., 1996; see also
 1028 Moninger et al., 2003), although many of the data from these early years do not meet the
 1029 necessary standards for assimilation. The volume of aircraft data suitable for assimilation
 1030 increased substantially after January 1973 (Uppala et al., 2005; Kobayashi et al., 2015).

1031
 1032 Aircraft temperature data have been reported to have a warm bias with respect to radiosonde
 1033 observations (Ballish and Kumar, 2008). This type of discrepancy among ingested data
 1034 sources can have important impacts on the analysis. For example, Rienecker et al. (2011)
 1035 and Simmons et al. (2014) have shown that an increase in the magnitude of the temperature
 1036 bias at 300 hPa in MERRA with respect to radiosondes in the middle to late 1990s coincides
 1037 with a large increase in the number of aircraft observations assimilated by the system.
 1038 Moreover, they conclude that differences in temperature trends at 200 hPa between MERRA
 1039 and ERA-Interim reflect the different impacts of aircraft temperatures in these two
 1040 reanalysis systems. MERRA-2 applies adaptive bias corrections to AMDAR observations
 1041 that may help to reduce the uncertainties associated with assimilating these data (McCarty et
 1042 al., 2016): after each analysis step the updated bias is estimated as a weighted running mean
 1043 of the aircraft observation increments from preceding analysis times. These adaptive bias
 1044 corrections are calculated and applied for each aircraft tail number in the database separately.

1045
 1046
 1047

1048 **2.4.3 Water vapour**

1049 The assimilation of radiosonde and satellite observations of humidity fields is problematic in
 1050 the upper troposphere and above, where water vapour mixing ratios are very low. The
 1051 impact of saturation means that humidity probability density functions are often highly non-
 1052 Gaussian (Ingleby et al., 2013). These issues are particularly pronounced in the vicinity of
 1053 the tropopause, where sharp temperature gradients complicate the calculation and
 1054 application of bias corrections for humidity variables during the assimilation step.
 1055 Reanalysis systems therefore often do not assimilate observations of water vapour provided
 1056 by radiosondes and/or microwave and infrared sounders (mostly in the form of radiances;
 1057 see Section 2.4.2.2) above a specified upper bound, which is typically between ~300 hPa

and \sim 100 hPa. In regions of the atmosphere that lie above this upper bound (i.e. the uppermost troposphere and stratosphere), the water vapour field is typically determined by the forecast model alone. In this case, water vapour in the stratosphere is determined mainly by transport from below, turbulent mixing, and dehydration in the vicinity of the tropical cold point tropopause (e.g., Gettelman et al., 2010). Table 2-18 provides brief descriptions of special treatments and caveats affecting reanalysis estimates of water vapour in the upper troposphere and stratosphere. A more detailed discussion and assessment of reanalysis estimates of water vapour is provided in Chapter 4 of this report.

Table 2-18. Notes on treatment of water vapour in the upper troposphere and stratosphere.

ERA-40	No adjustments due to data assimilation are applied in the stratosphere (above the diagnosed tropopause). Methane oxidation is included via a simple parametrization in the stratosphere.
ERA-Interim	The ERA-Interim system contains a parametrization that allows supersaturation with respect to ice in the cloud-free portions of grid cells with temperatures less than 250 K. The inclusion of this parametrization results in a substantial increase of relative humidity in the upper troposphere and stratospheric polar cap when compared with ERA-40 (Dee et al., 2011). No adjustments due to data assimilation are applied in the stratosphere (above the diagnosed tropopause). Methane oxidation is included via a simple parametrization in the stratosphere.
ERA-20C	ERA-20C does not assimilate any water vapour observations. Supersaturation with respect to ice is permitted in cloud-free portions of grid cells with temperatures less than 250 K, and methane oxidation is included via a simple parametrization in the stratosphere.
JRA-25 / JCDAS	Observations of humidity are not assimilated and analyses of moisture variables are not provided at pressures less than 100 hPa. Vertical correlations of humidity background errors are set to zero at pressures less than 50 hPa to prevent spurious analysis increments above this level. No moisture source due to methane oxidation is applied to water vapour in the stratosphere. The radiation scheme assumes a constant mixing ratio of 2.5 ppm in the stratosphere.
JRA-55	Analyses of moisture variables are not provided at pressures less than 100 hPa in the pressure-level analysis (anl_p), although analyses of moisture variables are provided for all model levels in the model-level analysis (anl_mdl). Observations of humidity are not assimilated at pressures less than 100 hPa, and vertical correlations of humidity background errors are set to zero at pressures less than 5 hPa to prevent spurious analysis increments above this level. No moisture source due to methane oxidation is applied to water vapour in the stratosphere. The radiation scheme uses climatological annual mean mixing ratios observed by HALOE and UARS MLS during 1991–1997 (without seasonal variations) in the stratosphere.
MERRA	The MERRA system tightly constrains stratospheric water vapour to a specified profile, which is based on zonal mean

	climatologies from HALOE and Aura MLS (Jiang et al., 2010; Rienecker et al., 2011). Water vapour above the tropopause does not undergo physically meaningful variations.
MERRA-2	Like MERRA, MERRA-2 tightly constrains stratospheric water vapour to a specified profile, which is based on zonal mean climatologies from HALOE and Aura MLS (Jiang et al., 2010; Rienecker et al., 2011). Water vapour above the tropopause does not undergo physically meaningful variations.
NCEP-NCAR R1	Analyses of moisture variables are not provided at pressures less than 300 hPa. Satellite humidity retrievals are not assimilated.
NCEP-DOE R2	Satellite humidity retrievals are not assimilated.
CFSR	Although there is no upper limit to assimilated GNSS-RO data, radiosonde humidities are only assimilated at pressures 250 hPa and greater. Moisture variables are provided in the stratosphere, but dehydration processes in the tropopause layer may yield negative values. Negative values are artificially replaced by very small positive values for the radiation calculations, but are not replaced in the analysis. CFSR does not include a parametrization of methane oxidation.
NOAA-CIRES 20CR v2	Moisture variables are provided in the stratosphere, but dehydration processes in the tropopause layer may yield negative values. Negative values are artificially replaced by very small positive values for the radiation calculations, but are not replaced in the analysis. 20CR does not include a parametrization of methane oxidation.

1068
1069
1070

1071 **2.5 EXECUTION STREAMS**1072 **2.5.1 What is an “execution stream”?**

1073 The production of reanalyses often must be completed under strict deadlines determined by
 1074 external factors. To meet these deadlines, most reanalyses have been executed in two or
 1075 more distinct “streams”, which are then combined. Discontinuities in the time series of some
 1076 analyzed variables may occur when streams are joined. These potential discontinuities
 1077 should be considered (along with the changes in assimilated observations described in
 1078 Section 2.4) when reanalysis variables are used for assessments of climate variability and/or
 1079 trends.

1080

1081

1082

1083 **2.5.2 Summary of stream execution**

1084 Table 2-19 and Figure 2-15 briefly summarize the streams used for generating each set of
 1085 reanalysis products. Refer to the reference papers listed in Table 2-1 for the procedures used
 1086 to transition between streams in creating the final data product, as different reanalysis
 1087 systems may use different approaches. Certain periods have been reprocessed to correct
 1088 errors in the input data. The reprocessed periods and associated potential discontinuities
 1089 listed in Table 2-19 and shown in Figure 2-15 may be incomplete, and are also likely to
 1090 change subsequent to the publication of this report. Users are therefore recommended to
 1091 contact the reanalysis centres directly if they encounter unexplained shifts or jumps in
 1092 reanalysis products.

1093

1094

1095

1096

Table 2-19. Information on the execution streams for each reanalysis system.

ERA-40	ERA-40 was planned for execution in three streams covering 1989–2002, 1957–1972, and 1972–1988. In practice, a small number of parallel-running sub-streams bridging gaps between the main streams had to be run in order to meet the production deadline.
ERA-Interim	ERA-Interim was carried out in two main streams, the first from 1989 to present and the second from 1979 to 1988. The period of the first stream covering January 1989 to August 1993 was rerun to include from the outset all changes made on the fly in the original production for this period; these changes were also included in the second main production stream. The second stream was extended to the end of 1989 to check consistency during the overlap period (see also discussion by Simmons et al., 2014).
ERA-20C	The reanalysis consists of 22 streams, all but the last of which are six years in length. The first stream starts on 1 January 1899 and extends through 31 December 1904. Each subsequent stream starts on 1 January in years ending in 4 or 9 and ends on 31 December of the next year ending in 4 or 9. The final stream starts on 1 January 2004 and extends seven years through the end of the reanalysis. The first year of each stream is discarded from the final product.

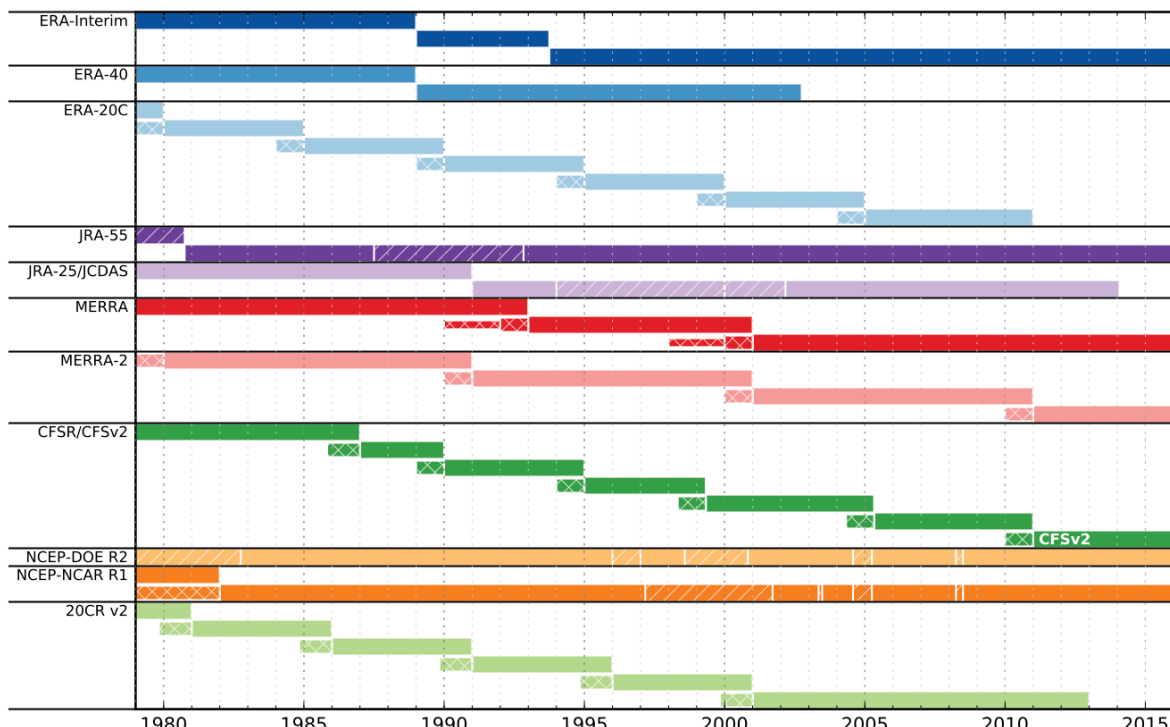
JRA-25 / JCDAS	JRA-25 was conducted in two main streams: the first covers January 1979–December 1990, and the second covers January 1991–January 2014. Note also the transition from JRA-25 (conducted jointly by JMA and CRIEPI) to JCDAS (conducted by JMA only) in January 2005. The execution of JCDAS was conducted entirely in real time. Two periods (January 1994–December 1999 and January 2000–January 2002) were recalculated and replaced to fix problems with data quality; these two periods may be considered as separate sub-streams in addition to the two main streams.
JRA-55	JRA-55 has been executed in two streams. Stream A covers January 1958 through August 1980, while stream B covers September 1980 through the present. Three periods have also been reprocessed after errors were identified: January to June 1958, December 1974 to August 1980 and June 1987 to September 1992 (see also Kobayashi et al., 2015; their Figure 7). JRA-55C has been executed in three streams: Stream A covers 1 November 1972 through 31 August 1980, Stream B covers 1 September 1980 through 31 August 2005, and Stream C covers 1 September 2005 through 31 December 2012. JRA-55AMIP has been executed in one continuous stream.
MERRA	MERRA was executed in three streams. Stream 1 covers January 1979–December 1992, stream 2 covers January 1993–December 2000, and stream 3 covers January 2001–present. Each stream was spun up in two stages: a 2-year analysis at $2^\circ \times 2.5^\circ$ followed by a 1-year analysis on the native MERRA grid (see Table 2-2).
MERRA-2	MERRA-2 was executed in four streams covering January 1980–December 1990, January 1991–December 2000, January 2001–December 2010, and January 2011–present. Each stream was spun up for one year on the full MERRA-2 system.
NCEP-NCAR R1	NCEP-NCAR R1 was run in three streams. The first stream, which produced data covering 1982–present, was started in December 1978. The second stream, covering 1958–1981 (post-IGY), was started second. For the third and final stream, which covers 1948–1957 (pre-IGY), the analyses were conducted at 03Z, 09Z, 15Z and 21Z (rather than 00Z, 06Z, 12Z and 18Z). There may be additional discontinuities involving updates. For example, the original analyses may have been affected by a problem with the sea ice boundary condition. A second simulation with an improved sea ice boundary condition may be run for a few months, and then replace the original analyses. Transitions between the original product and these “patches” may cause discontinuities.
NCEP-DOE R2	NCEP-DOE R2 was executed in one continuous stream; however, like NCEP-NCAR R1, there may be discontinuities involving updates.
CFSR	CFSR was produced by running six simultaneous streams covering the following periods: Stream 1: 1 December 1978 to 31 December 1986 Stream 2: 1 November 1985 to 31 December 1989

Stream 5: 1 January 1989 to 31 December 1994
 Stream 6: 1 January 1994 to 31 March 1999
 Stream 3: 1 April 1998 to 31 March 2005
 Stream 4: 1 April 2004 to 31 December 2009

A full 1-year overlap between the streams was used to address spinup issues concerning the deep ocean, the upper stratosphere and the deep soil. The entire CFSR thus covers 31 years (1979–2009) plus five overlap years. Each earlier stream is used to its end, so that the switch to the next stream occurs at the end of the overlap period. Model output from stream 4 was continued through the end of 2010, when the analysis system was updated to CFSv2 (with an increase in horizontal resolution from T382 to T574). For most applications, CFSR can be extended through the present using output from CFSv2.

NOAA-CIRES 20CR v2 20CR v2 was executed in 28 streams. With some exceptions, each stream typically produced five years of data with 14 months of spinup. The following text gives the data coverage provided by each stream (the streams are numbered sequentially), with the spin-up start year provided in parentheses: 1871–1875 (1869), 1876–1880 (1874), 1881–1885 (1879), 1886–1890 (1884), 1891–1895 (1889), 1896–1900 (1894), 1901–1905 (1899), 1906–1910 (1904), 1911–1915 (1909), 1916–1920 (1914), 1921–1925 (1919), 1926–1930 (1924), 1931–1935 (1929), 1936–1940 (1934), 1941–1945 (1939), 1946–1951 (1944), 1952–1955 (1949), 1956–1960 (1954), 1961–1965 (1959), 1966–1970 (1964), 1971–1975 (1969), 1976–1980 (1974), 1981–1985 (1979), 1986–1990 (1984), 1991–1995 (1989), 1996–2000 (1994), and 2001–2012 (1999). The spin-up start date for each stream was 00 UTC 1 November, the production start date was 00 UTC 1 January, and the production end date was 21 UTC 31 December.

1097
 1098
 1099



1100
1101 Figure 2-15. Summary of the execution streams of the reanalyses for the period 1979–2016.
1102 Hatching indicates known re-processed “patches”. The narrowest cross-hatched indicate
1103 known spin-up periods, while the medium-narrow cross-hatched sections indicate overlap
1104 periods. See also Table 2-19.
1105
1106
1107

1108 **2.6 ARCHIVED DATA**

1109 The original data at model resolution and model levels (Table 2-2) are converted by each
1110 reanalysis centre to data on regular horizontal grids (sometimes at multiple resolutions) and
1111 on pressure levels (see Appendix B) for public release. The converted data (and sometimes
1112 the original data) can typically be obtained via the reanalysis centre websites (see <http://s-rip.ees.hokudai.ac.jp/resources/links.html> for links). Some other institutes or projects, such
1113 as the NCAR Research Data Archive (RDA), have also constructed public archives of one or
1114 more of the reanalysis datasets. Such institutes may have used independent conversions for
1115 the data grid, levels, and/or units. Data users of a given public release should therefore
1116 always read the documentation for that release carefully.

1117
1118 It is particularly important to check unit information, as different reanalysis centres or public
1119 archives may use different units for the same variable. For example, temperature may be
1120 provided in units of °C or K. Some centres provide geopotential height in meters (or “gpm”),
1121 while others provide geopotential in m² s⁻². For water vapour, specific humidity (not volume
1122 mixing ratio) is provided in most cases, in units of either kg kg⁻¹ or g kg⁻¹. Some reanalyses
1123 do not provide vertical pressure velocity (ω , in Pa s⁻¹) and/or specific humidity data in the
1124 stratosphere. Ozone is provided as mass mixing ratio (not volume mixing ratio) in most
1125 cases, in units of either kg kg⁻¹ or mg kg⁻¹ (i.e., ppmm). Care is also recommended when
1126 using precipitation or other “flux” data, because the integration time period may not be
1127 explicitly documented in the data file. Precipitation data may also be divided into multiple
1128 categories (such as anvil, convective, and large-scale), the exact definitions of which vary by
1129 reanalysis.
1130

1131
1132 The file formats for archived data may include GRIB, GRIB2, NetCDF, and HDF. Grid
1133 boundaries and orientations, such as the starting point for longitude (0°E or 180°W), the
1134 order of latitudes (from the North Pole or from the South Pole), and the vertical orientation
1135 (from the surface or from the TOA) may also vary by reanalysis and/or data source.
1136

1137 Most reanalyses (with the exception of MERRA and MERRA-2) provide data below the
1138 surface (e.g., at 1000 hPa over the continents). These data are calculated via vertical
1139 extrapolation, and are provided for two reasons. First, they enable the use of a complete field
1140 when plotting or taking derivatives, and second, they allow data users to visualize variability
1141 over the whole globe (including features over mountains) using data from a single pressure
1142 surface. The extrapolation procedure may differ by variable and/or reanalysis system. For
1143 example, Yessad (2011) explained that the ECMWF analysis systems assume constant
1144 values for extrapolating horizontal wind and water-related variables, use surface
1145 temperatures for extrapolating geopotential, apply a complicated algorithm for extrapolating
1146 temperature, and assign vertical velocities below the surface a uniform value of zero. Users
1147 of data in the lower part of the troposphere should be aware of this feature, particularly in
1148 regions of complex topography.
1149

1150
1151
1152

1153 **ACKNOWLEDGMENTS**

1154 The materials contained in the tables and figures have been compiled from a variety of
1155 sources, for which we acknowledge the contributions of Santha Akella, Michael Bosilovich,
1156 Dick Dee, John Derber, Ron Gelaro, Yun-Tai Hou, Robert Kistler, Daryl Kleist, Shinya
1157 Kobayashi, Shrinivas Moorthi, Eric Nielsen, Saroja Polavarapu, Paul Poli, Bill Putman,
1158 Suranjana Saha, Jack Woollen, Fanglin Yang, and Valery Yudin. We thank Wenhao Dong,
1159 Suqin Duan, and Jacob Smith for providing helpful comments on advance drafts of this
1160 document.

1161

1162

1163

1164 REFERENCES

- 1165 Allan, P., P. Brohan, G. P. Compo, R. Stone, J. Luterbacher, and S. Brönnimann (2011), The
 1166 international Atmospheric Circulation Reconstructions over the Earth (ACRE) initiative,
 1167 *Bull. Amer. Meteor. Soc.*, 92, 1421–1425, doi: 10.1175/2011BAMS3218.1.
- 1168 Andrae, U., N. Sokka, and K. Onogi (2004), The radiosonde temperature bias corrections
 1169 used in ERA-40, *ECMWF ERA-40 Project Report Series*, 15, ECMWF, UK, 34 pp.
- 1170 Arakawa, A., and W. H. Schubert (1974), Interaction of a cumulus cloud ensemble with the
 1171 large-scale environment, part I, *J. Atmos. Sci.*, 31, 674–701.
- 1172 Auligné, T., A. P. McNally, D. P. and Dee (2007), Adaptive bias correction for satellite data
 1173 in a numerical weather prediction system, *Q. J. R. Meteorol. Soc.*, 133, 631–642, doi:
 1174 10.1002/qj.56.
- 1175 Bacmeister, J. T., M. J. Suarez, and F. R. Robertson (2006), Rain re-evaporation, boundary
 1176 layer–convection interactions, and Pacific rainfall patterns in an AGCM, *J. Atmos. Sci.*,
 1177 63, 3383–3403.
- 1178 Baines, P. G., and T. N. Palmer (1990), Rationale for a new physically based
 1179 parametrization of subgrid-scale orographic effects, *ECMWF Tech. Memo. No. 1699*, 11
 1180 pp.
- 1181 Ballish, B. A., and V. K. Kumar (2008), Systematic differences in aircraft and radiosonde
 1182 temperatures: Implications for NWP and climate studies, *Bull. Amer. Meteorol. Soc.*, 89,
 1183 1689–1708, doi:10.1175/2008BAMS2332.1.
- 1184 Beljaars, A. C. M. (1995), The impact of some aspects of the boundary layer scheme in the
 1185 ECMWF model, in *Proc. of ECMWF Seminar on Parametrization of Sub-grid Scale*
 1186 *Physical Processes*, pp. 125–161, Reading, 5–9 September 1994.
- 1187 Bengtsson, L., M. Kanamitsu, P. Källberg, and S. Uppala (1982), FGGE research activities
 1188 at ECMWF, *Bull. Amer. Meteor. Soc.*, 63, 277–303.
- 1189 Birner, T., D. Sankey, and T. G. Shepherd (2006), The tropopause inversion layer in models
 1190 and analyses, *Geophys. Res. Lett.*, 33, L14804, doi:10.1029/2006GL026549.
- 1191 Bloom, S., L. Takacs, A. DaSilva, and D. Ledvina (1996), Data assimilation using
 1192 incremental analysis updates, *Mon. Wea. Rev.*, 124, 1256–1271.
- 1193 Bodeker, G. E., S. Bojinski, D. Cimini, R. J. Dirksen, M. Haeffelin, J. W. Hannigan, D. F.
 1194 Hurst, T. Leblanc, F. Madonna, M. Maturilli, A. C. Mikalsen, R. Philipona, T. Reale, D.
 1195 J. Seidel, D. G. H. Tan, P. W. Thorne, H. Vömel, and J. Wang (2016), Reference upper-
 1196 air observations for climate: From concept to reality, *Bull. Amer. Meteor. Soc.*, 97, 123–
 1197 135, doi:10.1175/BAMS-D-14-00072.1.
- 1198 Bosilovich, M., S. Akella, L. Coy, R. Cullather, C. Draper, R. Gelaro, R. Kovach, Q. Liu, A.
 1199 Molod, P. Norris, K. Wargan, W. Chao, R. Reichle, L. Takacs, Y. Vikhlaev, S. Bloom,
 1200 A. Collow, S. Firth, G. Labow, G. Partyka, S. Pawson, O. Reale, S. D. Schubert, and M.
 1201 Suarez (2015), MERRA-2: Initial Evaluation of the Climate, *NASA Tech. Rep. Series on*
 1202 *Global Modeling and Data Assimilation*, NASA/TM-2015-104606, Vol. 43.
- 1203 Bouttier, F., and P. Courtier (1999), Data assimilation concepts and methods,
 1204 Meteorological Training Course Lecture Series, ECMWF 2002. [available at
 1205 <http://www.ecmwf.int/en/introductory-lectures-nwp>; accessed 19 May 2015].
- 1206 Briegleb, B. P. (1992), Delta-Eddington approximation for solar radiation in the NCAR
 1207 community climate model. *J. Geophys. Res.*, 97, 7603–7612.
- 1208 Buchard, V., A. M. da Silva, P. R. Colarco, A. Darmenov, C. A. Randles, R. Govinraraju, O.
 1209 Torres, J. Campbell, and R. Spurr (2015), Using the OMI aerosol index and absorption
 1210 aerosol optical depth to evaluate the NASA MERRA Aerosol Reanalysis, *Atmos. Chem.*
 1211 *Phys.*, 15, 5743–5760, doi:10.5194/acp-15-5743-2015.

- 1212 Buchard, V., C. A. Randles, A. M. da Silva, A. Darmenov, P. R. Colarco, R. Govindaraju, R.
 1213 Ferrare, J. Hair, A. J. Beyersdorf, L. D. Ziemka, and H. Yu (2016), The MERRA-2
 1214 Aerosol Reanalysis, 1980–onward, Part 2: Data assimilation, *J. Climate*, submitted.
- 1215 Buehner, M., P. L. Houtekamer, C. Charette, H. L. Miller and B. He (2010a),
 1216 Intercomparison of variational data assimilation and the ensemble Kalman filter for
 1217 global deterministic NWP. Part I: description and single-observation experiments, *Mon.*
 1218 *Wea. Rev.*, 138, 1550–1566.
- 1219 Buehner, M., P. L. Houtekamer, C. Charette, H. L. Miller and B. He (2010b),
 1220 Intercomparison of variational data assimilation and the ensemble Kalman filter for
 1221 global deterministic NWP. Part II: one-month experiments with real observations, *Mon.*
 1222 *Wea. Rev.*, 138, 1567–1586.
- 1223 Cariolle, D. and M. Déqué (1986), Southern hemisphere medium-scale waves and total
 1224 ozone disturbances in a spectral general circulation model, *J. Geophys. Res.*, 91, 10825–
 1225 10846.
- 1226 Cariolle, D. and H. Teyssèdre (2007), A revised linear ozone photochemistry
 1227 parameterization for use in transport and general circulation models: multi-annual
 1228 simulations, *Atmos. Chem. Phys.*, 7, 2183–2196, doi:10.5194/acp-7-2183-2007.
- 1229 Chou, M.-D., and K.-T. Lee (1996), Parameterizations for the absorption of solar radiation
 1230 by water vapor and ozone, *J. Atmos. Sci.*, 53, 1203–1208.
- 1231 Chou, M.-D., and M. J. Suarez (1999), A solar radiation parameterization for atmospheric
 1232 studies, *NASA Tech. Rep. Series on Global Modeling and Data Assimilation*,
 1233 NASA/TM-1999-104606, Vol. 15, 40 pp.
- 1234 Chou, M.-D., M. J. Suarez, X.-Z. Liang, and M. M.-H. Yan (2001), A thermal infrared
 1235 radiation parameterization for atmospheric studies, *NASA Tech. Rep. Series on Global*
 1236 *Modeling and Data Assimilation*, NASA/TM-2001-104606, Vol. 19, 56 pp.
- 1237 Chun, H.-Y, and J.-J. Baik (1998), Momentum flux by thermally induced internal gravity
 1238 waves and its approximation for large- scale models, *J. Atmos. Sci.*, 55, 3299–3310.
- 1239 Cionni, I., V. Eyring, J.-F. Lamarque, W. J. Randel, D. S. Stevenson, F. Wu, G. E. Bodeker,
 1240 T. G. Shepherd, D. T. Shindell, and D. W. Waugh (2011), Ozone database in support of
 1241 CMIP5 simulations: results and corresponding radiative forcing, *Atmos. Chem. Phys.*,
 1242 11, 11267–11292, doi:10.5194/acp-11-11267-2011.
- 1243 Clough, S. A., M. W. Shephard, E. J. Mlawer, J. S. Delamere, M. J. Iacono, K. Cady-Pereira,
 1244 S. Boukabara, and P. D. Brown (2005), Atmospheric radiative transfer modeling: A
 1245 summary of the AER codes, *J. Quant. Spectrosc. Radiat. Transfer*, 91, 233–244.
- 1246 Colarco, P. R., A. da Silva, M. Chin, and T. Diehl (2010), Global aerosol distributions in the
 1247 NASA GEOS-4 model and com- parisons to satellite and ground-based aerosol optical
 1248 depth. *J. Geophys. Res.*, 115, D14207, doi:10.1029/2009JD012820.
- 1249 Compo, G. P., J. S. Whitaker, P. D. Sardeshmukh, N. Matsui, R. J. Allan, X. Yin, B. E.
 1250 Gleason, R. S. Vose, G. Rutledge, P. Bessemoulin, S. Brönnimann, M. Brunet, R. I.
 1251 Cruthamel, A. N. Grant, P. Y. Groisman, P. D. Jones, M. C. Kruk, A. C. Kruger, G. J.
 1252 Marshall, M. Mauger1, H. Y. Mok, Ø. Nordli1, T. F. Ross, R. M. Trigo, X. L. Wang, S.
 1253 D. Woodruff, and S. J. Worley (2011), The twentieth century reanalysis project, *Q. J. R.*
 1254 *Meteorol. Soc.*, 137, 1–28, doi:10.1002/qj.776.
- 1255 Courtier, P., J.-N. Thépaut, and A. Hollingsworth (1994), A strategy for operational
 1256 implementation of 4D-Var, using an incremental approach, *Q. J. R. Meteorol. Soc.*,
 1257 120, 1367–1387, doi: 10.1002/qj.49712051912.
- 1258 Cram, T. A., G. P. Compo, X. Yin, R. J. Allan, C. McColl, R. S. Vose, J. S. Whitaker, N.
 1259 Matsui, L. Ashcroft, R. Auchmann, P. Bessemoulin, T. Brandsma, P. Brohan, M.
 1260 Brunet, J. Comeaux, R. Cruthamel, B. E. Gleason Jr, P. Y. Groisman, H. Hersbach, P.
 1261 D. Jones, T. Jónsson, S. Jourdain, G. Kelly, K. R. Knapp, A. Kruger, H. Kubota, G.

- 1262 Lentini, A. Lorrey, N. Lott, S. J. Lubker, J. Luterbacher, G. J. Marshall, M. Maugeri, C.
 1263 J. Mock, H. Y. Mok, Ø. Nordli, M. J. Rodwell, T. F. Ross, D. Schuster, L. Srnec, M. A.
 1264 Valente, Z. Vizi, X. L. Wang, N. Westcott, J. S. Woollen, and S. J. Worley (2015), The
 1265 International Surface Pressure Databank version 2, *Geosci. Data J.*, 2, 31–46,
 1266 doi:10.1002/gdj3.25.
- 1267 Dee, D. P. (2005), Bias and data assimilation, *Q. J. R. Meteorol. Soc.*, 131, 3323–3343, doi:
 1268 10.1256/qj.05.137.
- 1269 Dee, D. P., S. M. Uppala, A. J. Simmons, P. Berrisford, P. Poli, S. Kobayashi, U. Andrae, M.
 1270 A. Balmaseda, G. Balsamo, P. Bauer, P. Bechtold, A. C. M. Beljaars, L. van de Berg, J.
 1271 Bidlot, N. Bormann, C. Delsol, R. Dragani, M. Fuentes, A. J. Geer, L. Haimberger, S. B.
 1272 Healy, H. Hersbach, E. V. Hólm, L. Isaksen, P. Källberg, M. Köhler, M. Matricardi, A.
 1273 P. McNally, B. M. Monge-Sanz, J.-J. Morcrette, B.-K. Park, C. Peubey, P. de Rosnay, C.
 1274 Tavolato, J.-N. Thépaut and F. Vitart (2011), The ERA-Interim reanalysis:
 1275 Configuration and performance of the data assimilation system, *Q. J. R. Meteorol. Soc.*,
 1276 137, 553–597, doi:10.1002/qj.828.
- 1277 Dethof, A., and E. V. Hólm (2004), Ozone assimilation in the ERA-40 reanalysis project, *Q.
 1278 J. R. Meteorol. Soc.*, 130, 2851–2872, doi:10.1256/qj.03.196.
- 1279 Donlon, C., N. Rayner, I. Robinson, D. J. S. Poulter, K. S. Casey, J. Vazquez-Cuervo, E.
 1280 Armstrong, A. Bingham, O. Arino, C. Gentemann, D. May, P. LeBorgne, J. Piollé, I.
 1281 Barton, H. Beggs, C. J. Merchant, S. Heinz, A. Harris, G. Wick, B. Emery, P. Minnett,
 1282 R. Evans, D. Llewellyn-Jones, C. Mutlow, R. W. Reynolds, H. Kawamura (2007), The
 1283 global ocean data assimilation experiment high-resolution sea surface temperature pilot
 1284 project, *Bull. Amer. Meteor. Soc.*, 88, 1197–1213, doi:10.1175/BAMS-88-8-1197.
- 1285 Dragani, R. (2011), On the quality of the ERA-Interim ozone reanalyses: Comparisons with
 1286 satellite data, *Q. J. R. Meteorol. Soc.*, 137, 1312–1326, doi:10.1002/qj.821.
- 1287 Ebida, A., S. Kobayashi, Y. Ota, M. Moriya, R. Kumabe, K. Onogi, Y. Harada, S. Yasui, K.
 1288 Miyaoka, K. Takahashi, H. Kamahori, C. Kobayashi, H. Endo, M. Soma, Y. Oikawa, T.
 1289 Ishimizu (2011), The Japanese 55-year reanalysis “JRA-55”: An interim report, *Sci.
 1290 Online Lett. Atmos.*, 7, 149–152, doi:10.2151/sola.2011-038.
- 1291 Evensen, G., and P. J. van Leeuwen (2000), An Ensemble Kalman Smoother for nonlinear
 1292 dynamics, *Mon. Wea. Rev.*, 128, 1852–1867.
- 1293 Evensen, G. (2009), Data Assimilation: The Ensemble Kalman Filter, Springer, Berlin, 307
 1294 pp.
- 1295 Fels, S., and M. D. Schwarzkopf (1975), The simplified exchange approximation: A new
 1296 method for radiative transfer calculations. *J. Atmos. Sci.*, 32, 1475–1488.
- 1297 Fouquart, Y., and B. Bonnel (1980), Computation of solar heating of the Earth’s
 1298 atmosphere: a new parameterization, *Beitr. Phys.*, 53, 35–62.
- 1299 Fortuin, J. P., and U. Langematz (1995), An update on the current ozone climatology and on
 1300 concurrent ozone and temperature trends, *Proc. SPIE*, 2311, 207–216,
 1301 doi:10.1117/12.198578.
- 1302 Freidenreich, S. M., and V. Ramaswamy (1999), A new multiple-band solar radiative
 1303 parameterization for general circulation models, *J. Geophys. Res.*, 104, 31389–31409.
- 1304 Garcia, R. R., and B. A. Boville (1994), Downward control of the mean meridional
 1305 circulation and temperature distribution of the polar winter stratosphere, *J. Atmos. Sci.*,
 1306 51, 2238–2245.
- 1307 Gelaro, R., et al. (2016), The Modern-Era Retrospective Analysis for Research and
 1308 Applications, Version-2 (MERRA-2), *J. Climate*, submitted.
- 1309 Gettelman, A., M. I. Hegglin, S-W. Son, J. Kim, M. Fujiwara, T. Birner, S. Kremser, M.
 1310 Rex, J. A. Añel, H. Akiyoshi, J. Austin, S. Bekki, P. Braesike, C. Brühl, N. Butchart, M.
 1311 Chipperfield, M. Dameris, S. Dhomse, H. Garny, S. C. Hardiman, P. Jöckel, D. E.

- 1312 Kinnison, J. F. Lamarque, E. Mancini, M. Marchand, M. Michou, O. Morgenstern, S.
 1313 Pawson, G. Pitari, D. Plummer, J. A. Pyle, E. Rozanov, J. Scinocca, T. G. Shepherd, K.
 1314 Shibata, D. Smale, H. Teyssèdre, and W. Tian (2010), Multimodel assessment of the
 1315 upper troposphere and lower stratosphere: Tropics and global trends, *J. Geophys. Res.*,
 1316 115, D00M08, doi:10.1029/2009JD013638.
- 1317 Gibson, J. K., P. Kållberg, S. M. Uppala, A. Nomura, A. Hernandez, and E. Serrano (1997),
 1318 ERA description, *ERA-15 Rep. Series*, 1, 72 pp., 1997.
- 1319 Goldberg, M., G. Ohring, J. Butler, C. Cao, R. Datla, D. Doelling, V. Gärtner, T. Hewison,
 1320 B. Iacovazzi, D. Kim, T. Kurino, J. Lafeuille, P. Minnis, D. Renaut, J. Schmetz, D.
 1321 Tobin, L. Wang, F. Weng, X. Wu, F. Yu, P. Zhang, and T. Zhu (2011), The Global
 1322 Space-based Inter-Calibration System, *Bull. Amer. Meteor. Soc.*, 92, 467–475.
- 1323 Goody, R. M. (1952), A statistical model for water-vapour absorption, *Quart. J. Roy. Meteor.*
 1324 *Soc.*, 78, 165–169.
- 1325 Gustafsson, N. (2007), Discussion on ‘4D-Var or EnKF?’, *Tellus A*, 59, 774–777,
 1326 doi:10.1111/j.1600-0870.2007.00262.x.
- 1327 Haimberger, L., C. Tavolato, and S. Sperka (2008), Towards elimination of the warm bias in
 1328 historic radiosonde temperature records — some new results from a comprehensive
 1329 intercomparison of upper air data, *J. Climate*, 21, 4587–4606.
- 1330 Haimberger, L. and U. Andrae (2011), Radiosonde temperature bias correction in ERA-
 1331 Interim, ERA Report Series, Vol. 8, ECMWF, Reading, England, 19 pp. [Available at
 1332 http://old.ecmwf.int/publications/library/ecpublications/_pdf/era/era_report_series/RS_8.pdf; accessed 28 September 2015]
- 1333 Haimberger, L., C. Tavolato, and S. Sperka (2012), Homogenization of the global
 1334 radiosonde temperature dataset through combined comparison with reanalysis back-
 1335 ground series and neighboring stations, *J. Climate*, 25, 8108–8131.
- 1336 Helfand, H. M., J. C. Jusem, J. Pfäntner, J. Tenenbaum, and E. Kalnay (1987), The effect
 1337 of a gravity wave drag parameterization scheme on GLA fourth-order GCM forecasts,
 1338 *Collection of papers presented at the WMO/IUGG NWP Symposium*, Tokyo, 4–8
 1339 August 1986, 729–742.
- 1340 Helfand, H. M. and S. D. Schubert (1995), Climatology of the simulated Great Plains low-
 1341 level jet and its contribution to the continental moisture budget of the United States, *J.*
 1342 *Climate*, 8, 784–806.
- 1343 Hering, W. S., and T. R. Borden, Jr. (1965), Mean distributions of ozone density over North
 1344 America, 1963–1964, Tech. Rep. AFCRL-65-913, Air Force Cambridge Research
 1345 Laboratories.
- 1346 Hersbach, H., C. Peubey, A. Simmons, P. Berrisford, P. Poli, and D. Dee (2015), ERA-
 1347 20CM: a twentieth-century atmospheric model ensemble, *Q. J. R. Meteorol. Soc.*, 141,
 1348 2350–2375, doi: 10.1002/qj.2528.
- 1349 Hong, S.-Y. and H.-L. Pan (1996), Nonlocal boundary layer vertical diffusion in a medium-
 1350 range forecast model, *Mon. Wea. Rev.*, 124, 2322–2339.
- 1351 Ingleby, N. B., A. C. Lorenc, K. Ngan, F. Rawlins, and D. R. Jackson (2013), Improved
 1352 variational analyses using a nonlinear humidity control variable, *Q. J. R. Meteorol. Soc.*,
 1353 139, 1875–1887, doi:10/1002/qj.2073.
- 1354 IPCC (1996), Climate Change 1995: The Science of Climate Change. Contribution of
 1355 Working Group I to the Second Assessment Report of the Intergovernmental Panel on
 1356 Climate Change, Houghton, J.T., L.G. Meira Filho, B.A. Callander, N. Harris, A.
 1357 Kattenberg, and K. Maskell (eds.), Cambridge University Press, Cambridge, United
 1358 Kingdom and New York, NY, USA, 572 pp.
- 1359

- 1360 Ishii, M., A. Shouji, S. Sugimoto, and T. Matsumoto (2005), Objective analyses of sea-
 1361 surface temperature and marine meteorological variables for the 20th century using
 1362 ICOADS and the KOBE collection, *Int. J. Climatol.*, 25, 865–879.
- 1363 Iwasaki, T., S. Yamada, and K. Tada (1989a), A parameterization scheme of orographic
 1364 gravity wave drag with the different vertical partitionings, Part I: Impact on medium
 1365 range forecasts, *J. Meteor. Soc. Japan*, 67, 11–27.
- 1366 Iwasaki, T., S. Yamada, and K. Tada (1989b), A parameterization scheme of orographic
 1367 gravity wave drag with the different vertical partitionings, Part II: Zonally averaged
 1368 budget analyses based on transformed Eulerian-mean method. *J. Meteor. Soc. Japan*, 67,
 1369 29–41.
- 1370 Jiang, J. H., H. Su, S. Pawson, H.-C. Liu, W. G. Read, J. W. Waters, M. L. Santee, D. L. Wu,
 1371 M. J. Schwartz, N. J. Livesey, A. Lambert, R. A. Fuller, and J. N. Lee (2010), Five year
 1372 (2004–2009) observations of upper tropospheric water vapor and cloud ice from MLS
 1373 and comparisons with GEOS-5 analyses, *J. Geophys. Res.*, 115, D15103,
 1374 doi:10.1029/2009JD013256.
- 1375 JMA (2013), Outline of the operational numerical weather prediction at the Japan
 1376 Meteorological Agency. *WMO Technical Progress Report on the Global Data-
 1377 processing and Forecasting System (GDPFS) and Numerical Weather Prediction (NWP)
 1378 Research*, JMA, Japan, 188 pp. [Available at [http://www.jma.go.jp/jma/jma-eng/jma-
 1379 center/nwp/nwp-top.htm](http://www.jma.go.jp/jma/jma-eng/jma-center/nwp/nwp-top.htm)].
- 1380 Kalman, R. E. (1960), A new approach to linear filtering and prediction problems, *J. Basic
 1381 Eng.*, 82, 35–45.
- 1382 Kalnay, E., M. Kanamitsu, R. Kistler, W. Collins, D. Deaven, L. Gandin, M. Iredell, S. Saha,
 1383 G. White, J. Woollen, Y. Zhu, A. Leetmaa, R. Reynolds, M. Chelliah, W. Ebisuzaki, W.
 1384 Higgins, J. Janowiak, K. C. Mo, C. Ropelewski, J. Wang, R. Jenne, and D. Joseph
 1385 (1996), The NCEP/NCAR 40-year reanalysis project, *Bull. Am. Meteorol. Soc.*, 77(3),
 1386 437–471.
- 1387 Kalnay, E., H. Li, T., Miyoshi, S.-C. Yang, and J. Ballabrera-Poy (2007a), 4-D-Var or
 1388 ensemble Kalman filter?, *Tellus A*, 59, 758–773, doi:10.1111/j.1600-0870.2007.00261.x.
- 1389 Kalnay, E., H. Li, T., Miyoshi, S.-C. Yang, and J. Ballabrera-Poy (2007b), Response to the
 1390 discussion on “4-D-Var or EnKF?” by Nils Gustafsson, *Tellus A*, 59, 778–780,
 1391 doi:10.1111/j.1600-0870.2007.00263.x.
- 1392 Kanamitsu, M., W. Ebisuzaki, J. Woollen, S.-K. Yang, J. J. Hnilo, M. Fiorino, and G. L.
 1393 Potter (2002), NCEP-DOE AMIP-II reanalysis (R-2), *Bull. Am. Meteorol. Soc.*, 83(11),
 1394 1631–1643.
- 1395 Kawai, H. and T. Inoue (2006), A simple parameterization scheme for subtropical marine
 1396 stratocumulus, *Sci. Online Lett. Atmos.*, 2, 17–20.
- 1397 Kim, Y.-J., and A. Arakawa (1995), Improvement of orographic gravity wave
 1398 parameterization using a mesoscale gravity wave model, *J. Atmos. Sci.*, 83, 1875–1902.
- 1399 Kistler, R., W. Collins, S. Saha, G. White, J. Woollen, E. Kalnay, M. Chelliah, W. Ebisuzaki,
 1400 M. Kanamitsu, V. Kousky, H. van den Dool, R. Jenne, and M. Fiorino (2001), The
 1401 NCEP-NCAR 50-year reanalysis: Monthly means CD-ROM and documentation, *Bull.
 1402 Am. Meteorol. Soc.*, 82(2), 247–267.
- 1403 Kobayashi, C., H. Endo, Y. Ota, S. Kobayashi, H. Onoda, Y. Harada, K. Onogi, and H.
 1404 Kamahori (2014), Preliminary results of the JRA-55C, an atmospheric reanalysis
 1405 assimilating conventional observations only, *Sci. Online Lett. Atmos.*, 10, 78–82, doi:
 1406 10.2151/sola.2014-016.
- 1407 Kobayashi, S., Y. Ota, Y. Harada, A. Ebita, M. Moriya, H. Onoda, K. Onogi, H. Kamahori,
 1408 C. Kobayashi, H. Endo, K. Miyaoka, and K. Takahashi (2015), The JRA-55 reanalysis:

- 1409 General specifications and basic characteristics, *J. Meteor. Soc. Japan*, 93, 5–48,
 1410 doi:10.2151/jmsj.2015-001.
- 1411 Köhler, M., M. Ahlgrimm, and A. Beljaars (2011), Unified treatment of dry convective and
 1412 stratocumulus-topped boundary layers in the ECMWF model, *Q. J. R. Meteorol. Soc.*,
 1413 137, 43–57.
- 1414 Koepke, P., M. Hess, I. Schult, and E. P. Shettle (1997), Global Aerosol Data Set, Report No.
 1415 243, Max-Planck-Institut für Meteorologie, Hamburg, ISSN 0937-1060, 44 pp.
- 1416 Krishnamurti, T. N., and L. Bounoua (1996), *An Introduction to Numerical Weather
 1417 Prediction Techniques*, CRC Press, Florida, USA, 293 pp.
- 1418 Lacis, A. A., and J. E. Hansen (1974), A parameterization for the absorption of solar
 1419 radiation in the Earth's atmosphere. *J. Atmos. Sci.*, 31, 118–133.
- 1420 Lamarque, J.-F., T. C. Bond, V. Eyring, C. Granier, A. Heil, Z. Klimont, D. Lee, C. Liousse,
 1421 A. Mieville, B. Owen, M. G. Schultz, D. Shindell, S. J. Smith, E. Stehfest, J. Van
 1422 Aardenne, O. R. Cooper, M. Kainuma, N. Mahowald, J. R. McConnell, V. Naik, K.
 1423 Riahi, and D. P. van Vuuren, (2010), Historical (1850–2000) gridded anthropogenic and
 1424 biomass burning emissions of reactive gases and aerosols: methodology and application,
 1425 *Atmos. Chem. Phys.*, 10, 7017–7039, doi:10.5194/acp-10-7017-2010.
- 1426 Lawless, A. S. (2010), A note on the analysis error associated with 3D-FGAT, *Q. J. R.
 1427 Meteorol. Soc.*, 136, 1094–1098, doi: 10.1002/qj.619.
- 1428 Lawrence, Z. D., G. L. Manney, K. Minschwaner, M. L. Santee, and A. Lambert (2015),
 1429 Comparisons of polar processing diagnostics from 34 years of the ERA-Interim and
 1430 MERRA reanalyses, *Atmos. Chem. Phys.*, 15, 3873–3892, doi:10.5194/acp-15-3873-
 1431 2015.
- 1432 Lin, S.-J. (2004), A vertically Lagrangian finite-volume dynamical core for global models,
 1433 *Mon. Wea. Rev.*, 132, 2293–2307.
- 1434 Lindzen, R. S., E. S. Batten, and J. W. Kim (1968), Oscillations in atmospheres with tops,
 1435 *Mon. Wea. Rev.*, 96, 133–140.
- 1436 Liu, Q., T. Marchok, H. Pan, M. Bender, and S. Lord (1999), Improvements in hurricane
 1437 initialization and forecasting at NCEP with global and regional (GFDL) models, *NOAA
 1438 Tech. Proc. Bull.*, 472, National Weather Service, Office of Meteorology, Silver Spring,
 1439 MD, 1–7.
- 1440 Lock, A. P., A. R. Brown, M. R. Bush, G. M. Martin, and R. N. B. Smith (2000), A new
 1441 boundary layer mixing scheme. Part I: Scheme description and single-column model
 1442 tests, *Mon. Wea. Rev.*, 128, 3187–3199.
- 1443 London, J. (1962), Mesospheric dynamics, part III. The distribution of total ozone in the
 1444 Northern Hemisphere, Final Report, Dept. of Meteorology and Oceanography, New
 1445 York University, 99 pp.
- 1446 Lorenc, A. C. and Rawlins, F. (2005), Why does 4D-Var beat 3D-Var?, *Q. J. R. Meteorol.
 1447 Soc.*, 131, 3247–3257, doi: 10.1256/qj.05.85.
- 1448 Lott, F., and M. J. Miller (1997), A new subgrid-scale orographic drag parametrization: Its
 1449 formulation and testing, *Q. J. R. Meteorol. Soc.*, 123, 101–127.
- 1450 Louis, J. F. (1979), Parametric model of vertical eddy fluxes in the atmosphere, *Boundary
 1451 Layer Meteorol.*, 17, 187–202.
- 1452 Louis, J. F., M. Tiedtke, and J.-F. Geleyn (1982), A short history of the operational PBL
 1453 parametrization at ECMWF, in *Proc. ECMWF Workshop on Boundary Layer
 1454 Parametrization*, pp. 59–80, Reading, 25–27 November 1981.
- 1455 Machenhauer, B. (1979), The Spectral Method, in: Numerical Methods used in Atmospheric
 1456 Models, Vol. II, *GARP Publication Series*, 17, World Meteorological Organization,
 1457 Geneva, 121–275.

- 1458 Matsumoto, T., M. Ishii, Y. Fukuda, and S. Hirahara (2006), Sea ice data derived from
 1459 microwave radiometer for climate monitoring, *Proceedings of the 14th Conference on*
 1460 *Satellite Meteorology and Oceanography*, Atlanta, USA, P2.21.
- 1461 McCarty, W., L. Coy, R. Gelaro, D. Merkova, E. B. Smith, M. Sienkiewicz, and K. Wargan
 1462 (2016), MERRA-2 input observations: Summary and assessment, *NASA Tech. Rep.*
 1463 *Series on Global Modeling and Data Assimilation*, NASA/TM-2016-104606, Vol. 46.
- 1464 McCormack, J.P., S.D. Eckermann, D.E. Siskind, and T. McGee (2006), CHEM2D-OPP: A
 1465 new linearized gas-phase ozone photochemistry parameterization for high-altitude NWP
 1466 and climate models, *Atmos. Chem. Phys.*, 6, 4943–4972.
- 1467 McFarlane, N. A. (1987), The effect of orographically excited gravity-wave drag on the
 1468 circulation of the lower stratosphere and troposphere, *J. Atmos. Sci.*, 44, 1775–1800.
- 1469 Meinshausen, M., S. J. Smith, K. V. Calvin, J. S. Daniel, M. L. T. Kainuma, J.-F. Lamarque,
 1470 K. Matsumoto, S. A. Montzka, S. C. B. Raper, K. Riahi, A. M. Thomson, G. J. M.
 1471 Velders, and D. van Vuuren (2011), The RCP greenhouse gas concentrations and their
 1472 extension from 1765 to 2300, *Clim. Change*, 109, 213–241, doi: 10.1007/s10584-011-
 1473 0156-z.
- 1474 Mellor, G. L. and T. Yamada (1974), A hierarchy of turbulence closure models for planetary
 1475 boundary layers, *J. Atmos. Sci.*, 31, 1791–1806.
- 1476 Mellor, G. L. and T. Yamada (1982), Development of a turbulence closure model for
 1477 geophysical fluid problems, *Rev. Geophys. Space Phys.*, 20, 851–875.
- 1478 Miller, M. J., T. N. Palmer, and R. Swinbank (1989), Parametrization and influence of
 1479 subgrid-scale orography in general circulation and numerical weather prediction models,
 1480 *Meteorol. Atmos. Phys.*, 40, 84–109.
- 1481 Mlawer, E. J., S. J. Taubman, P. D. Brown, M. J. Iacono, and S. A. Clough (1997),
 1482 Radiative transfer for inhomogeneous atmospheres: RRTM, a validated correlated-k
 1483 model for the long wave, *J. Geophys. Res.*, 102, 16663–16682.
- 1484 Molod, A. (2012), Constraints on the profiles of total water PDF in AGCMs from AIRS and
 1485 a high-resolution model, *J. Climate*, 25, 8341–8352, doi:10.1175/JCLI-D-11-00412.1
- 1486 Molod, A., L. Takacs, M. Suarez, and J. Bacmeister (2015), Development of the GEOS-5
 1487 atmospheric general circulation model: Evolution from MERRA to MERRA-2, *Geosci.
 1488 Model Dev.*, 8, 1339–1356.
- 1489 Moninger, W. R., R. D. Mamrosh, and P. M. Pauley (2003), Automated meteorological
 1490 reports from commercial aircraft, *Bull. Amer. Meteor. Soc.*, 84, 203–216,
 1491 doi:10.1175/BAMS-84-2-203.
- 1492 Moorthi, S., and M. J. Suarez (1992), Relaxed Arakawa-Schubert: A parameterization of
 1493 moist convection for general-circulation models, *Mon. Wea. Rev.*, 120, 978–1002.
- 1494 Moorthi, S., H.-L. Pan, and P. Caplan (2001), Changes to the 2001 NCEP operational
 1495 MRF/AVN global analysis/forecast system, *Technical Procedures Bulletin 484*, NOAA
 1496 NWS, Silver Spring, MD, 14 pp. [<http://www.nws.noaa.gov/om/tpb/484.htm>]
- 1497 Moorthi, S., R. Sun, H. Xiao, and C. R. Mechoso (2010), Low-cloud simulation in the
 1498 Southeast Pacific in the NCEP GFS: Role of vertical mixing and shallow convection,
 1499 *NCEP Office Note 463*, 28 pp.
- 1500 Morcrette, J-J., H. W. Barker, J. N. S. Cole, M. J. Iacono, and R. Pincus (2008), Impact of a
 1501 new radiation package, McRad, in the ECMWF Integrated Forecasting System, *Mon.
 1502 Wea. Rev.*, 136, 4773–4798, doi: 10.1175/2008MWR2363.1.
- 1503 Nash, J., T. Oakley, H. Vömel, and W. Li (2011), WMO intercomparison of high quality
 1504 radiosonde systems, Yangjiang, China, 12 July–3 August 2010, Instruments and
 1505 Observing Methods Report No. 107, WMO/TD-No. 1580, 238 pp.

- 1506 Nash, J., and R. Saunders (2015), A review of Stratospheric Sounding Unit radiance
 1507 observations for climate trends and reanalyses, *Q. J. R. Meteorol. Soc.*, 141, 2103–2113,
 1508 doi:10.1002/qj.2505.
- 1509 Onogi, K., J. Tsutsui, H. Koide, M. Sakamoto, S. Kobayashi, H. Hatsushika, T. Matsumoto,
 1510 N. Yamazaki, H. Kamahori, K. Takahashi, S. Kadokura, K. Wada, K. Kato, R. Oyama,
 1511 T. Ose, N. Manojoji, and R. Taira (2007), The JRA-25 reanalysis, *J. Meteorol. Soc. Jpn.*,
 1512 85(3), 369–432, doi:10.2151/jmsj.85.369.
- 1513 Reale, A. L. (2001), NOAA operational sounding products from Advanced-TOVS polar
 1514 orbiting environmental satellites, NOAA Technical Report NESDIS 102, 59 pp.
- 1515 Rosenfield, J. E., M. R. Schoeberl, and M. A. Geller (1987), A computation of the
 1516 stratospheric diabatic circulation using an accurate radiative transfer model, *J. Atmos.
 1517 Sci.*, 44, 859–876.
- 1518 Palmer, T. N., G. J. Schutts, and R. Swinbank (1986), Alleviation of a systematic westerly
 1519 bias in general circulation and numerical weather prediction models through an
 1520 orographic gravity wave drag parametrization, *Quart. J. Roy. Meteor. Soc.*, 112, 1001–
 1521 1039.
- 1522 Paltridge, G. W., and C. M. R. Platt (1976), Radiative Processes in Meteorology and
 1523 Climatology, Elsevier, New York, 336 pp.
- 1524 Park, S. K., and D. Županski (2003), Four-dimensional variational data assimilation for
 1525 mesoscale and storm-scale applications, *Meteorol. Atmos. Phys.*, 82, 173–208,
 1526 doi:10.1007/s00703-001-0586-7.
- 1527 Petersen, R. A. (2016), On the impact and benefits of AMDAR observations in operational
 1528 forecasting — Part I: A review of the impact of automated aircraft wind and
 1529 temperature reports, *Bull. Amer. Meteorol. Soc.*, 585–602, doi:10.1175/BAMS-D-
 1530 00055.1.
- 1531 Pierrehumbert, R. T. (1986), An essay on the parameterization of orographic gravity wave
 1532 drag, *Seminar/Workshop 1986 Observation, Theory and Modelling of Orographic
 1533 Effects*, ECMWF Shinfield Park, Reading UK, 251–282.
- 1534 Polavarapu, S. M. and M. Pulido (2016), Stratospheric and mesospheric data assimilation:
 1535 The role of middle atmospheric dynamics, in: Data Assimilation for Atmospheric,
 1536 Oceanic and Hydrologic Applications, vol. 3, edited by: S. K. Park and L. Xu, in press,
 1537 Springer-Verlag, Berlin.
- 1538 Poli, P., S. B. Healy, and D. P. Dee (2010), Assimilation of Global Positioning System radio
 1539 occultation data in the ECMWF ERA–Interim reanalysis, *Q. J. R. Meteorol. Soc.*, 136,
 1540 1972–1990, doi: 10.1002/qj.722.
- 1541 Poli, P., H. Hersbach, D. Tan, D. Dee, J.-N. Thépaut, A. Simmons, C. Peubey, P. Laloyaux,
 1542 T. Komori, P. Berrisford, R. Dragani, Y. Trémolet, E. Hólm, M. Bonavita, L. Isaksen,
 1543 and M. Fisher (2013), The data assimilation system and initial performance of the
 1544 ECMWF pilot reanalysis of the 20th-century assimilating surface observations only
 1545 (ERA-20C), *ERA Report Series*, Vol. 14.
- 1546 Poli, P., H. Hersbach, D. P. Dee, P. Berrisford, A. Simmons, F. Vitart, P. Laloyaux, P., D. G.
 1547 H. Tan, C. Peubey, J.-N. Thépaut, Y. Trémolet, E. Hólm, M. Bonavita, L. Isaksen, and
 1548 M. Fisher (2016), ERA-20C: An atmospheric reanalysis of the 20th century, *J. Climate*,
 1549 29, 4083–4097, doi: 10.1175/JCLI-D-15-0556.1.
- 1550 Randel, W., P. Udelhofen, E. Fleming, M. Geller, M. Gelman, K. Hamilton, D. Karoly, D.
 1551 Ortland, S. Pawson, R. Swinbank, F. Wu, M. Baldwin, M.-L. Chanin, P. Keckhut, K.
 1552 Labitzke, E. Remsberg, A. Simmons, and D. Wu (2004), The SPARC intercomparison
 1553 of middle-atmosphere climatologies, *J. Climate*, 17, 986–1003.
- 1554 Randles, C. A., A. da Silva, V. Buchard, P. R. Colarco, A. Darmenov, A. Smirnov, B.
 1555 Holben, R. Ferrare, J. Hair, Y. Shinozuka, and C. J. Flynn (2016a), The MERRA-2

- 1556 Aerosol Reanalysis, 1980–onward, Part 1: System description and data assimilation
 1557 evaluation, *J. Climate*, submitted.
- 1558 Randles, C.A, A. M. da Silva, V. Buchard, A. Darmenov, P. R. Colarco, V. Aquila, H. Bian,
 1559 E. P. Nowottnick, X. Pan, A. Smirnov, H. Yu, and R. Govindaraju (2016b), The
 1560 MERRA-2 aerosol assimilation, *NASA Tech. Rep. Series on Global Modeling and Data*
 1561 *Assimilation*, NASA/TM-2016-104606.
- 1562 Reynolds, R. W., T. M. Smith, C. Liu, D. B. Chelton, K. S. Casey, and M. G. Schlax (2007),
 1563 Daily high-resolution blended analyses for sea surface temperature, *J. Climate*, 20,
 1564 5473–5496, doi:10.1175/2007JCLI1824.1.
- 1565 Rienecker, M. M., M. J. Suarez, R. Todling, J. Bacmeister, L. Takacs, H.-C. Liu, W. Gu, M.
 1566 Sienkiewicz, R.D. Koster, R. Gelaro, I. Stajner, and J.E. Nielsen (2008), The GEOS-5
 1567 Data Assimilation System—Documentation of versions 5.0.1 and 5.1.0, and 5.2.0.
 1568 *NASA Tech. Rep. Series on Global Modeling and Data Assimilation*, NASA/TM-2008-
 1569 104606, Vol. 27, 92 pp.
- 1570 Rienecker, M. M., M. J. Suarez, R. Gelaro, R. Todling, J. Bacmeister, E. Liu, M. G.
 1571 Bosilovich, S. D. Schubert, L. Takacs, G.-K. Kim, S. Bloom, J. Chen, D. Collins, A.
 1572 Conaty, A. da Silva, W. Gu, J. Joiner, R. D. Koster, R. Lucchesi, A. Molod, T. Owens,
 1573 S. Pawson, P. Pegion, C. R. Redder, R. Reichle, F. R. Robertson, A. G. Ruddick, M.
 1574 Sienkiewicz, and J. Woollen (2011), MERRA: NASA's modern-era retrospective
 1575 analysis for research and applications, *J. Clim.*, 24, 3624–3648, doi:10.1175/JCLI-D-
 1576 11-00015.1.
- 1577 Saha, S., S. Moorthi, H.-L. Pan, X. Wu, J. Wang, S. Nadiga, P. Tripp, R. Kistler, J. Woollen,
 1578 D. Behringer, H. Liu, D. Stokes, R. Grumbine, G. Gayno, J. Wang, Y.-T. Hou, H.-Y.
 1579 Chuang, H.-M. H. Juang, J. Sela, M. Iredell, R. Treadon, D. Kleist, P. Van Delst, D.
 1580 Keyser, J. Derber, M. Ek, J. Meng, H. Wei, R. Yang, S. Lord, H. van den Dool, A.
 1581 Kumar, W. Wang, C. Long, M. Chelliah, Y. Xue, B. Huang, J.-K. Schemm, W.
 1582 Ebisuzaki, R. Lin, P. Xie, M. Chen, S. Zhou, W. Higgins, C.-Z. Zou, Q. Liu, Y. Chen, Y.
 1583 Han, L. Cucurull, R. W. Reynolds, G. Rutledge, and M. Goldberg (2010), The NCEP
 1584 climate forecast system reanalysis, *Bull. Am. Meteorol. Soc.*, 91(8), 1015–1057,
 1585 doi:10.1175/2010BAMS3001.1.
- 1586 Saha, S., S. Moorthi, X. Wu, J. Wang, S. Nadiga, P. Tripp, D. Behringer, Y.-T. Hou, H.-Y.
 1587 Chuang, M. Iredell, M. Ek, J. Meng, R. Yang, M. P. Mendez, H. van den Dool, Q.
 1588 Zhang, W. Wang, M. Chen, and E. Becker (2014), The NCEP Climate Forecast System
 1589 version 2, *J. Climate*, 27, 2185–2208, doi:10.1175/JCLI-D-12-00823.1.
- 1590 Sakamoto, M. and J. R. Christy (2009), The influences of TOVS radiance assimilation on
 1591 temperature and moisture tendencies in JRA-25 and ERA-40, *J. Atmos. Ocean. Tech.*,
 1592 26, 1435–1455.
- 1593 Sato, M., J. E. Hansen, M. P. McCormick, and J. B. Pollack (1993), Stratospheric aerosol
 1594 optical depths, 1850–1990, *J. Geophys. Res.*, 98, 22987–22994, doi:10.1029/93JD02553.
- 1595 Schoeberl, M. R., A. R. Douglass, Z. Zhu, and S. Pawson (2003), A comparison of the lower
 1596 stratospheric age spectra derived from a general circulation model and two data
 1597 assimilation systems, *J. Geophys. Res.*, 108, 4113, doi:10.1029/2002JD002652.
- 1598 Schubert, S. D., J. Pfaendtner, and R. Rood (1993), An assimilated data set for Earth science
 1599 applications, *Bull. Am. Meteor. Soc.*, 74, 2331–2342.
- 1600 Schubert, S. D., C.-K. Park, C.-Y. Wu, W. Higgins, Y. Kondratyeva, A. Molod, L. L.
 1601 Takacs, M. Seabloom, and R. B. Rood (1995), A multiyear assimilation with the GEOS-1
 1602 system: Overview and results, *NASA Tech. Rep. Series on Global Modeling and Data*
 1603 *Assimilation*, NASA/TM-104606, Vol. 6, 201 pp..

- 1604 Schwarzkopf, M. D., and S. Fels (1991), The simplified exchange method revisited: An
 1605 accurate, rapid method for computation of infrared cooling rates and fluxes. *J. Geophys*
 1606 *Res.*, 96(D5), 9075–9096.
- 1607 Scinocca, J. F. (2003), An accurate spectral nonorographic gravity wave drag
 1608 parameterization for general circulation models, *J. Atmos. Sci.*, 60, 667–682.
- 1609 Shepherd, T. G., K. Semeniuk, and J. N. Koshyk (1996), Sponge layer feedbacks in middle-
 1610 atmosphere models, *J. Geophys. Res.*, 101, 23447–23464.
- 1611 Shepherd, T. G. and T. A. Shaw (2004), The angular momentum constraint on climate
 1612 sensitivity and downward influence in the middle atmosphere, *J. Atmos. Sci.*, 61, 2899–
 1613 2908.
- 1614 Seidel, D. J., F. H. Berger, H. J. Diamond, J. Dykema, D. Goodrich, F. Immler, W. Murray,
 1615 T. Peterson, D. Sisterson, M. Sommer, P. Thorne, H. Vömel, and J. Wang (2009),
 1616 Reference upper-air observations for climate: Rationale, progress, and plans, *Bull. Am.*
 1617 *Meteorol. Soc.*, 90, 361–369, doi:10.1175/2008BAMS2540.1.
- 1618 Simmons, A. J., and D. M. Burridge (1981), An energy and angular-momentum conserving
 1619 finite-difference scheme and hybrid vertical coordinates. *Mon. Wea. Rev.*, 109, 758–766.
- 1620 Simmons, A. J., P. Poli, D. P. Dee, P. Berrisford, H. Hersbach, S. Kobayashi, and C. Peubey
 1621 (2014), Estimating low-frequency variability and trends in atmospheric temperature
 1622 using ERA-Interim, *Q. J. R. Meteorol. Soc.*, 140, 329–353. doi:10.1002/qj.2317.
- 1623 Spencer, J. W. (1971), Fourier series representation of the position of the sun, *Search*, 2, 172
 1624 [available at <http://www.mail-archive.com/sundial@uni-koeln.de/msg01050.html>].
- 1625 Takacs, L. L., M. Suarez, and R. Todling (2015), Maintaining atmospheric mass and water
 1626 balance within reanalysis, *NASA Tech. Rep. Series on Global Modeling and Data*
 1627 *Assimilation*, NASA/TM-2014-104606, Vol. 37, 46 pp.
- 1628 Talagrand, O. (2010), Variational assimilation, in: *Data Assimilation: Making Sense of*
 1629 *Observations*, edited by: W. Lahoz, B. Khattatov, and R. Menard, 41–67, Springer-
 1630 Verlag, Berlin.
- 1631 Tan, W. W., M. A. Geller, S. Pawson, and A. da Silva (2004), A case study of excessive
 1632 subtropical transport in the stratosphere of a data assimilation system, *J. Geophys. Res.*,
 1633 109, D11102, doi:10.1029/2003JD004057.
- 1634 Tanré, D., J.-F. Geleyn, and J. M. Slingo (1984), First results of the introduction of an
 1635 advanced aerosol-radiation interaction in the ECMWF low resolution global model. Pp.
 1636 133–177 in *Aerosols and their Climatic Effects*, H. E. Gerber and A. Deepak (eds.), A.
 1637 Deepak Publishing: Hampton, VA, USA.
- 1638 Tavolato, C., and L. Isaksen (2010), Data usage and quality control for ERA-40, ERA-
 1639 Interim, and the operational ECMWF data assimilation system, *ERA Report Series*, No.
 1640 7, ECMWF, Reading, UK, 44 pp.
- 1641 Taylor, K. E., D. Williamson, and F. Zwiers (2000), The sea surface temperature and sea ice
 1642 concentration boundary conditions for AMIP II simulations, *Program for Climate*
 1643 *Model Diagnosis and Intercomparison (PCMDI) Report 60*, Lawrence Livermore
 1644 National Laboratory.
- 1645 Tegen, I., P. Hoorig, M. Chin, I. Fung, D. Jacob, and J. Penner (1997), Contribution of
 1646 different aerosol species to the global aerosol extinction optical thickness: Estimates
 1647 from model results, *J. Geophys. Res.*, 102, 23895–23915.
- 1648 Tiedtke, M. (1983), The sensitivity of the time-mean large-scale flow to cumulus convection
 1649 in the ECMWF model. *ECMWF Workshop on Convection in Large-Scale Models*,
 1650 Reading, UK, ECMWF, 297–316.
- 1651 Tiedtke, M. (1989), A comprehensive mass flux scheme for cumulus parameterization in
 1652 large-scale models. *Mon. Wea. Rev.*, 117, 1779–1800.

- 1653 Tiedtke, M. (1993), Representation of clouds in large-scale models, *Mon. Wea. Rev.*, 121,
1654 3040–3061.
- 1655 Titchner, H. A. and N. A. Rayner (2014), The Met Office Hadley Centre sea ice and sea
1656 surface temperature data set, version 2: 1. Sea ice concentrations, *J. Geophys. Res.*, 119,
1657 2864–2889, doi:10.1002/2013JD020316.
- 1658 Tompkins, A. M., K. Gierens, and G. Rädel (2007), Ice supersaturation in the ECMWF
1659 integrated forecast system, *Q. J. R. Meteorol. Soc.*, 133, 53–63.
- 1660 Troen, I. and Mahrt, L. (1986), A simple model of the atmospheric boundary layer;
1661 sensitivity to surface evaporation, *Boundary Layer Meteorol.*, 37, 129–148.
- 1662 Tsuyuki, T., and T. Miyoshi (2007), Recent progress of data assimilation methods in
1663 meteorology, *J. Meteorol. Soc. Jpn.*, 85B, 331–361, doi:10.2151/jmsj.85B.331.
- 1664 Uppala, S. M., P. W. Kållberg, A. J. Simmons, U. Andrae, V. Da Costa Bechtold, M.
1665 Fiorino, J. K. Gibson, J. Haseler, A. Hernandez, G. A. Kelly, X. Li, K. Onogi, S.
1666 Saarinen, N. Sokka, R. P. Allan, E. Andersson, K. Arpe, M. A. Balmaseda, A. C. M.
1667 Beljaars, L. Van De Berg, J. Bidlot, N. Bormann, S. Caires, F. Chevallier, A. Dethof, M.
1668 Dragosavac, M. Fisher, M. Fuentes, S. Hagemann, E. Hólm, B. J. Hoskins, L. Isaksen, P.
1669 A. E. M. Janssen, R. Jenne, A. P. McNally, J.-F. Mahfouf, J.-J. Morcrette, N. A. Rayner,
1670 R. W. Saunders, P. Simon, A. Sterl, K. E. Trenberth, A. Untch, D. Vasiljevic, P. Viterbo,
1671 and J. Woollen (2005), The ERA-40 re-analysis, *Q. J. R. Meteorol. Soc.*, 131(612),
1672 2961–3012.
- 1673 van Vuuren D. P., J. Edmonds, M. Kainuma, K. Riahi, A. Thomson, K. Hibbard, G. C. Hurtt,
1674 T. Kram, V. Krey, J.-F. Lamarque, T. Masui, M. Meinshausen, N. Nakicenovic, S. J.
1675 Smith, and S. K. Rose (2011), The representative concentration pathways: An overview,
1676 *Clim. Change*, 109, 5–31.
- 1677 Walsh, J. E., and W. L. Chapman (2001), 20th-century sea-ice variations from observational
1678 data, *Annals of Glaciology*, 33, 444–448.
- 1679 Wang, L., C.-Z. Zou, and H. Qian (2012), Construction of stratospheric temperature data
1680 records from Stratospheric Sounding Units, *J. Climate*, 25, 2931–2946,
1681 doi:10.1175/JCLI-D-11-00350.1.
- 1682 Wang, W. and C.-Z. Zou (2014), AMSU-A-only atmospheric temperature data records from
1683 the lower troposphere to the top of the stratosphere, *J. Atmos. Ocean. Tech.*, 31, 808–
1684 825, doi:10.1175/JTECH-D-13-00134.1.
- 1685 Whitaker, J. S., G. P. Compo, and J.-N. Thépaut (2009), A comparison of variational and
1686 ensemble-based data assimilation systems for reanalysis of sparse observations, *Mon.
1687 Wea. Rev.*, 137, 1991–1999.
- 1688 WMO (1986), *A preliminary cloudless standard atmosphere for radiation computation*,
1689 World Climate Programme (WCP), 112, 53 pp.
- 1690 Woodruff, S. D., S. J. Worley, S. J. Lubker, Z. Ji, J. E. Freeman, D. I. Berry, P. Brohan, E. C.
1691 Kent, R. W. Reynolds, S. R. Smith, and C. Wilkinson (2011), ICOADS release 2.5:
1692 Extensions and enhancements to the surface marine meteorological archive, *Int. J.
1693 Climatol.*, 31, 951–967, doi:10.1002/joc.2103.
- 1694 Xie, S., and M. Zhang (2000), Impact of the convection triggering function on single-
1695 column model simulations. *J. Geophys. Res.*, 105, 14983–14996.
- 1696 Xu, K. M., and D. A. Randall (1996), A semiempirical cloudiness parameterization for use
1697 in climate models. *J. Atmos. Sci.*, 53, 3084–3102.
- 1698 Yessad, K. (2011), FULL-POS in the Cycle 38 of ARPEGE/IFS, 76 pp. [search “full pos
1699 CY38” at <https://software.ecmwf.int/wiki/display/OIFS/OpenIFS+Home>].
- 1700 Zhao, Q. Y., and F. H. Carr (1997), A prognostic cloud scheme for operational NWP models.
1701 *Mon. Wea. Rev.*, 125, 1931–1953.

- 1702 Zou, C.-Z., M. D. Goldberg, Z. Cheng, N. C. Grody, J. Sullivan, C. Cao, and D. Tarpley
1703 (2006), Recalibration of microwave sounding unit for climate studies using simultaneous
1704 nadir overpasses, *J. Geophys. Res.*, 111, D19114, doi:10.1029/2005JD006798.
1705 Zou, C.-Z., and W. Wang (2011), Intersatellite calibration of AMSU-A observations for
1706 weather and climate applications, *J. Geophys. Res.*, 116, D23113,
1707 doi:10.1029/2011JD016205.
1708 Zou, C.-Z., H. Qian, W. Wang, L. Wang, and C. Long (2014), Recalibration and merging of
1709 SSU observations for stratospheric temperature trend studies, *J. Geophys. Res.*, 119,
1710 13180–13205, doi:10.1002/2014JD021603.
1711
1712
1713
1714

1715 APPENDIX A: LIST OF ACRONYMS

- 1716
 1717 3D-Var: 3-dimensional variational assimilation scheme
 1718 3D-FGAT: 3-dimensional variational assimilation scheme with first guess at appropriate
 1719 time
 1720 4D-Var: 4-dimensional variational assimilation scheme
 1721 ABL: atmospheric boundary layer
 1722 ACARS: Aircraft Communications Addressing and Reporting System
 1723 ACRE: Atmospheric Circulation Reconstructions over the Earth
 1724 AER: Atmospheric and Environmental Research
 1725 AERONET: Aerosol Robotic Network
 1726 AGCM: atmospheric general circulation model
 1727 AIRS: Atmospheric Infrared Sounder
 1728 AMDAR: Aircraft Meteorological Data Relay
 1729 AMIP: Atmospheric Model Intercomparison Project
 1730 AMSR: Advanced Microwave Scanning Radiometer
 1731 AMSR-E: Advanced Microwave Scanning Radiometer for EOS
 1732 AMSU: Advanced Microwave Sounding Unit
 1733 AMV: atmospheric motion vectors
 1734 AOD: aerosol optical depth
 1735 Aqua: a satellite in NASA's Earth Observing System (EOS) A-Train constellation
 1736 ASCAT: Advanced Scatterometer
 1737 ATMS: Advanced Technology Microwave Sounder
 1738 ATOVS: Advanced TIROS Operational Vertical Sounder
 1739 Aura: a satellite in NASA's Earth Observing System (EOS) A-Train constellation
 1740 AVHRR: Advanced Very High Resolution Radiometer
 1741 BAS: British Antarctic Survey
 1742 BOM: Bureau of Meteorology (Australia)
 1743 BUOY: Surface meteorological observation report from buoys
 1744 CCARDS: Comprehensive Aerological Reference Dataset, Core Subset
 1745 CFC: chlorofluorocarbon
 1746 CFS: Climate Forecast System of the NCEP
 1747 CHAMP: CHAllenging Minisatellite Payload
 1748 CIRES: Cooperative Institute for Research in Environmental Sciences (NOAA and
 1749 University of Colorado Boulder)
 1750 CMIP5: Coupled Model Intercomparison Project Phase 5
 1751 COBE: Centennial in-situ Observation-Based Estimates of variability of SST and marine
 1752 meteorological variables
 1753 COSMIC: Constellation Observing System for Meteorology, Ionosphere, and Climate
 1754 CrIS: Cross-track Infrared Sounder
 1755 CRIEPI: Central Research Institute of Electric Power Industry
 1756 CRTM: Community Radiative Transfer Model
 1757 CTM: chemical transport model
 1758 DAS: data assimilation system
 1759 DMSP: Defense Meteorological Satellite Program
 1760 DOE: Department of Energy
 1761 ECMWF: European Centre for Medium-Range Weather Forecasts
 1762 EMC: Ensemble Modeling Center
 1763 EnKF: Ensemble Kalman Filter assimilation scheme

- 1764 EOS: Earth Observing System of the NASA
 1765 ERA-15: ECMWF 15-year reanalysis
 1766 ERA-20C: ECMWF 20th century reanalysis
 1767 ERA-40: ECMWF 40-year reanalysis
 1768 ERA-CLIM: European Reanalysis of Global Climate Observations
 1769 ERA-Interim: ECMWF interim reanalysis
 1770 ERS: European Remote Sensing satellite
 1771 EUMETSAT: European Organisation for the Exploitation of Meteorological Satellites
 1772 FGGE: First GARP (Global Atmospheric Research Program) Global Experiment
 1773 FORMOSAT: The name given to the Republic of China Satellite (ROCSat) following a
 1774 public naming competition.
 1775 GAAS: Goddard Aerosol Assimilation System
 1776 GARP: Global Atmospheric Research Program
 1777 GATE: GARP (Global Atmospheric Research Program) Atlantic Tropical Experiment
 1778 GAW: Global Atmosphere Watch
 1779 GEO: geostationary satellites
 1780 GEOS: Goddard Earth Observing System Model of the NASA
 1781 GFDL: Geophysical Fluid Dynamics Laboratory of the NOAA
 1782 GFS: Global Forecast System of the NCEP
 1783 GISST: UKMO Global Ice and Sea Surface Temperature dataset
 1784 GLATOVS: Goddard Laboratory for Atmospheres TOVS (radiative transfer model)
 1785 GLDAS: Global Land Data Assimilation System
 1786 GMS: Geostationary Meteorological Satellite
 1787 GNSS-RO: Global Navigation Satellite System Radio Occultation (see also GPS-RO)
 1788 GOCART: Goddard Chemistry, Aerosol, Radiation, and Transport model
 1789 GODAS: NCEP Global Ocean Data Assimilation System
 1790 GOES: Geostationary Operational Environmental Satellite
 1791 GOME: Global Ozone Monitoring Experiment
 1792 GPS-RO: Global Positioning System Radio Occultation (see also GNSS-RO)
 1793 GRACE: Gravity Recovery and Climate Experiment
 1794 GRUAN: Global Climate Observing System Reference Upper Air Network
 1795 GSI: Gridpoint Statistical Interpolation assimilation scheme
 1796 GSICS: Global Space-based Inter-calibration System
 1797 GSM: Global Spectral Model of the JMA
 1798 GTS: Global Telecommunication System
 1799 HadISST: UKMO Hadley Centre Sea Ice and SST dataset
 1800 HALOE: Halogen Occultation Experiment
 1801 HCFC: hydrochlorofluorocarbon
 1802 HIRS: High-resolution Infrared Radiation Sounder
 1803 IASI: Infrared Atmospheric Sounding Interferometer
 1804 IAU: Incremental Analysis Update procedure
 1805 ICOADS: International Comprehensive Ocean-Atmosphere Data Set
 1806 IFS: Integrated Forecast System of the ECMWF
 1807 IGY: International Geophysical Year (July 1957–December 1958)
 1808 IPCC: Intergovernmental Panel on Climate Change
 1809 IPSD: International Surface Pressure Databank
 1810 IR: infrared (sounders)
 1811 JAXA: Japan Aerospace Exploration Agency
 1812 JCDAS: JMA Climate Data Assimilation System
 1813 JCSDA: Joint Center for Satellite Data Assimilation

- 1814 JMA: Japan Meteorological Agency
 1815 JRA-25: Japanese 25-year Reanalysis
 1816 JRA-55: Japanese 55-year Reanalysis
 1817 JRA-55AMIP: Japanese 55-year Reanalysis based on AMIP-type simulations
 1818 JRA-55C: Japanese 55-year Reanalysis assimilating Conventional observations only
 1819 LEO/GEO: Low Earth Orbit / Geostationary
 1820 LIE: Line Islands Experiment
 1821 MARS: Meteorological Archival and Retrieval System of the ECMWF
 1822 MERRA: Modern Era Retrospective-Analysis for Research
 1823 Met Office: see UKMO
 1824 METEOSAT: geostationary meteorological satellites operated by EUMETSAT
 1825 MetOp: A series of three polar orbiting meteorological satellites operated by the
 EUMETSAT
 1827 MHS: Microwave Humidity Sounder
 1828 MIPAS: Michelson Interferometer for Passive Atmospheric Sounding
 1829 MISR: Multiangle Imaging Spectroradiometer
 1830 MIT: Massachusetts Institute of Technology
 1831 MLS: Microwave Limb Sounder
 1832 MODIS: MODerate resolution Imaging Spectroradiometer
 1833 MOM: Modular Ocean Model
 1834 MRF: Medium Range Forecast Version of the NCEP Global Forecast System
 1835 MRI-CCM1: Meteorological Research Institute (JMA) Chemistry Climate Model, version 1
 1836 MSU: Microwave Sounding Unit
 1837 MTSAT: Multi-functional Transport Satellite
 1838 MW: microwave (sounders)
 1839 NASA: National Aeronautics and Space Administration
 1840 NCAR: National Center for Atmospheric Research
 1841 NCDC: National Climatic Data Center of the NOAA
 1842 NCEP: National Centers for Environmental Prediction of the NOAA
 1843 NCEP-CFSR: Climate Forecast System Reanalysis of the NCEP
 1844 NCEP-DOE R-2: Reanalysis 2 of the NCEP and DOE
 1845 NCEP-NCAR R-1: Reanalysis 1 of the NCEP and NCAR
 1846 NESDIS: National Environmental Satellite, Data, and Information Service
 1847 NIST: National Institute of Standards and Technology
 1848 NOAA: National Oceanic and Atmospheric Administration
 1849 NOAA-CIRES 20CR: 20th Century Reanalysis of the NOAA and CIRES
 1850 OISST: NOAA Optimum Interpolation Sea Surface Temperature
 1851 OMI: Ozone Monitoring Instrument
 1852 OSTIA: Operational Sea Surface Temperature and Sea-Ice Analysis
 1853 PAOBS: Bogus surface pressure data for the Southern Hemisphere produced by the
 Australian Bureau of Meteorology
 1855 PCMDI: Program of Climate Model Diagnosis and Intercomparison
 1856 PIBAL: Pilot Balloon
 1857 QBO: Quasi-Biennial Oscillation
 1858 QC: quality control
 1859 QuikSCAT: Quick Scatterometer
 1860 RAOBCORE: Radiosonde Observation Correction using Reanalyses
 1861 RO: radio occultation
 1862 RRTM: Rapid Radiative Transfer Model of the AER
 1863 RRTMG: Rapid Radiative Transfer Model for application to GCMs of the AER

- 1864 RTG: NCEP Real-Time Global sea surface temperature
 1865 RTTOV: Radiative Transfer for TOVS
 1866 S-RIP: SPARC Reanalysis Intercomparison Project
 1867 SBUV: Solar Backscatter Ultraviolet Radiometer
 1868 SCIAMACHY: SCanning Imaging Absorption spectrometer for Atmospheric
 CHartographY
 1870 SEVIRI: Spinning Enhanced Visible and Infrared Imager
 1871 SHIP: Surface meteorological observation report from ships
 1872 SIC: sea ice concentration
 1873 SMMR: Scanning Multichannel Microwave Radiometer
 1874 SNDR: Sounder (for radiance measurements by the GOES 8 to 12)
 1875 SNO: Simultaneous Nadir Overpass method
 1876 SOLARIS-HEPPA: Solar Influences for SPARC-High Energy Partical Precipitation in the
 Atmosphere
 1877 SPARC: Stratosphere-troposphere Processes And their Role in Climate (previously
 Stratospheric Processes And their Role in Climate)
 1880 SSM/I or SSMI: Special Sensor Microwave Imager
 1881 SSMIS: Special Sensor Microwave Imager Sounder
 1882 SST: sea surface temperature
 1883 SSU: Stratospheric Sounding Unit
 1884 SYNOP: Surface meteorological observation report from manned and automated weather
 stations
 1885 TD: tape deck ("TD" is a name of a rawinsonde dataset. For example, TD54 is a dataset of
 mandatory level data from rawinsondes during 1946-1972 prepared by the USAF. See
 <http://rda.ucar.edu/docs/papers-scanned/pdf/rj0187.pdf> (accessed 29 May 2015).
 1889 Terra: a satellite in NASA's Earth Observing System (EOS).
 1890 TerraSAR-X: a German satellite with a phased array Synthetic Aperture Radar (SAR)
 antenna at the X-band wavelength
 1892 TIM: Total Irradiance Monitor
 1893 TIROS: Television Infrared Observation Satellite
 1894 TIROS-N: Television InfraRed Operational Satellite - Next-generation
 1895 TMI: TRMM Microwave Imager
 1896 TOA: top of atmosphere
 1897 TOMS: Total Ozone Mapping Spectrometer
 1898 TOVS: TIROS Operational Vertical Sounder
 1899 TRMM: Tropical Rainfall Measuring Mission
 1900 UARS: Upper Atmosphere Research Satellite
 1901 UKMO: United Kingdom Meteorological Office (or Met Office)
 1902 USAF: U.S. Air Force
 1903 USCNTRL: U.S. controlled oceanweather stations
 1904 VTPR: Vertical Temperature Profile Radiometer
 1905 WMO: World Meteorological Organization
 1906
 1907
 1908

1909 APPENDIX B: VERTICAL LEVELS OF THE MODELS

1910 I) ERA-40 and ERA-Interim

1911 ERA-40 and ERA-Interim both use hybrid sigma-pressure (hybrid $\sigma-p$) vertical coordinates
 1912 (Simmons and Burridge, 1981), which are also sometimes referred to as eta (η) vertical
 1913 coordinates (see also http://rda.ucar.edu/datasets/ds627.0/docs/Eta_coordinate/). Both
 1914 systems use the same vertical resolution with 61 levels. The pressure on each level is
 1915 calculated as $p_k = A_k + B_k \times p_{\text{srf}}$, where p_{srf} is surface pressure. The following table provides
 1916 example pressures at layer interfaces ($k-1/2$) and layer midpoints (k) for a surface pressure
 1917 of 1013.25 hPa, from TOA to surface. Pressures at layer midpoints are defined as the
 1918 average of pressures at layer interfaces. Pressure levels in brackets are used for ERA-Interim
 1919 products but not for ERA-40 products.

k	Model Levels				Pressure Levels p (hPa)
	$A_{k-1/2}$ (hPa)	$B_{k-1/2}$	$p_{k-1/2}$ (hPa)	p_k (hPa)	
1	0.00	0.00000	0.00	0.10	
2	0.20	0.00000	0.20	0.29	
3	0.38	0.00000	0.38	0.51	
4	0.64	0.00000	0.64	0.80	
5	0.96	0.00000	0.96	1.15	1
6	1.34	0.00000	1.34	1.58	
7	1.81	0.00000	1.81	2.08	2
8	2.35	0.00000	2.35	2.67	3
9	2.98	0.00000	2.98	3.36	
10	3.74	0.00000	3.74	4.19	
11	4.65	0.00000	4.65	5.20	5
12	5.76	0.00000	5.76	6.44	7
13	7.13	0.00000	7.13	7.96	
14	8.84	0.00000	8.84	9.89	10
15	10.95	0.00000	10.95	12.26	
16	13.56	0.00000	13.56	15.19	
17	16.81	0.00000	16.81	18.81	20
18	20.82	0.00000	20.82	23.31	
19	25.80	0.00000	25.80	28.88	30
20	31.96	0.00000	31.96	35.78	
21	39.60	0.00000	39.60	44.33	
22	49.07	0.00000	49.07	54.62	50
23	60.18	0.00000	60.18	66.62	70
24	73.07	0.00000	73.07	80.40	
25	87.65	0.00008	87.73	95.98	100
26	103.76	0.00046	104.23	113.42	
27	120.77	0.00182	122.61	132.76	(125)
28	137.75	0.00508	142.90	154.00	150
29	153.80	0.01114	165.09	177.12	(175)
30	168.19	0.02068	189.15	202.09	200
31	180.45	0.03412	215.03	228.84	(225)
32	190.28	0.05169	242.65	257.36	250
33	197.55	0.07353	272.06	287.64	300
34	202.22	0.09967	303.22	319.63	
35	204.30	0.13002	336.04	353.23	(350)
36	203.84	0.16438	370.41	388.27	400
37	200.97	0.20248	406.13	424.57	
38	195.84	0.24393	443.01	461.90	(450)
39	188.65	0.28832	480.79	500.00	500
40	179.61	0.33515	519.21	538.591	(550)
41	168.99	0.38389	557.97	577.38	
42	157.06	0.43396	596.78	616.04	600
43	144.11	0.48477	635.31	654.27	(650)
44	130.43	0.53571	673.24	691.75	700
45	116.33	0.58617	710.26	728.16	
46	102.10	0.63555	746.06	763.20	(750), 775
47	88.02	0.68327	780.35	796.59	(800)
48	74.38	0.72879	812.83	828.05	(825)
49	61.44	0.77160	843.26	857.34	850
50	49.42	0.81125	871.42	884.27	(875)
51	38.51	0.84737	897.11	908.65	(900)
52	28.88	0.87966	920.19	930.37	925

53	20.64	0.90788	940.55	949.35	(950)
54	13.86	0.93194	958.15	965.57	
55	8.55	0.95182	972.99	979.06	(975)
56	4.67	0.96765	985.14	989.95	
57	2.10	0.97966	994.75	998.39	1000
58	0.66	0.98827	1002.02	1004.64	
59	0.07	0.99402	1007.26	1009.06	
60	0.00	0.99763	1010.85	1012.05	
	0.00	1.00000	1013.25		

1920 (*¹) The ERA-40 Archive, Per Källberg, Adrian Simmons, Sakari Uppala and Manuel
 1921 Fuentes, ECMWF ERA-40 Project Report Series, September 2004, Revised October 2007.
 1922
 1923
 1924
 1925 2) *ERA-20C*

1926 ERA-20C uses hybrid sigma–pressure (hybrid $\sigma-p$) vertical coordinates (Simmons and
 1927 Burridge, 1981) with 91 levels. The pressure on each level is calculated as $p_k = A_k + B_k \times p_{\text{srf}}$,
 1928 where p_{srf} is surface pressure. The following table provides example pressures at layer
 1929 interfaces ($k=1/2$) and layer midpoints (k) for a surface pressure of 1013.25 hPa, from TOA
 1930 to surface. Pressures at layer midpoints are defined as the average of pressures at layer
 1931 interfaces.

k	Model Levels			Pressure Levels	
	$A_{k-1/2}$ (hPa)	$B_{k-1/2}$	$p_{k-1/2}$ (hPa)	p_k (hPa)	p (hPa)
1	0	0	0	0.01	
2	0.02	0	0.02	0.03	
3	0.03980832	0	0.04	0.06	
4	0.07387186	0	0.07	0.10	
5	0.12908319	0	0.13	0.17	
6	0.21413612	0	0.21	0.28	
7	0.33952858	0	0.34	0.43	
8	0.51746601	0	0.52	0.64	
9	0.76167656	0	0.76	0.92	1
10	1.08715561	0	1.09	1.30	
11	1.50986023	0	1.51	1.78	2
12	2.04637451	0	2.05	2.38	
13	2.71356506	0	2.71	3.12	3
14	3.52824493	0	3.53	4.02	
15	4.50685791	0	4.51	5.09	5
16	5.66519226	0	5.67	6.34	7
17	7.01813354	0	7.02	7.80	
18	8.57945801	0	8.58	9.47	10
19	10.36166504	0	10.36	11.37	
20	12.37585449	0	12.38	13.50	
21	14.6316394	0	14.63	15.88	
22	17.13709595	0	17.14	18.52	
23	19.8987439	0	19.90	21.41	20
24	22.92155518	0	22.92	24.57	
25	26.20898438	0	26.21	27.99	
26	29.76302246	0	29.76	31.67	30
27	33.58425781	0	33.58	35.63	
28	37.67196045	0	37.67	39.85	
29	42.02416504	0	42.02	44.33	
30	46.63776367	0	46.64	49.07	50
31	51.50859863	0	51.51	54.07	
32	56.6315625	0	56.63	59.31	
33	61.99839355	0	62.00	64.80	
34	67.59727051	0	67.60	70.51	70
35	73.41469727	0	73.41	76.43	
36	79.4292627	0.000014	79.44	82.57	
37	85.64624023	0.000055	85.70	88.96	
38	92.08305664	0.000131	92.22	95.62	
39	98.73560547	0.000279	99.02	102.58	100
40	105.5888184	0.000548	106.14	109.89	
41	112.6248438	0.001	113.64	117.59	
42	119.8266211	0.001701	121.55	125.75	125
43	127.1389746	0.002765	129.94	134.40	

44	134.5322559	0.004267	138.86	143.59	
45	141.9200977	0.006322	148.33	153.35	150
46	149.2268555	0.009035	158.38	163.72	
47	156.3805371	0.012508	169.05	174.72	175
48	163.2956055	0.01686	180.38	186.38	
49	169.9062305	0.022189	192.39	198.76	200
50	176.1328125	0.02861	205.12	211.87	
51	181.910293	0.036227	218.62	225.77	225
52	187.1696875	0.045146	232.91	240.48	
53	191.8454492	0.055474	248.05	256.07	250
54	195.8751367	0.067316	264.08	272.56	
55	199.1979688	0.080777	281.05	290.02	
56	201.7539453	0.095964	298.99	308.48	300
57	203.4891602	0.112979	317.97	327.99	
58	204.341582	0.131935	338.02	348.62	350
59	204.2621875	0.152934	359.22	370.42	
60	203.1901172	0.176091	381.61	393.44	400
61	201.0703125	0.20152	405.26	417.73	
62	197.8535742	0.229315	430.21	443.34	450
63	193.4877539	0.259554	456.48	470.17	
64	187.9882227	0.291993	483.85	497.96	500
65	181.4129688	0.326329	512.07	526.46	
66	173.855957	0.362203	540.86	555.40	550
67	165.4458594	0.399205	569.94	584.49	
68	156.3356641	0.436906	599.03	613.50	600
69	146.6564551	0.475016	627.97	642.29	650
70	136.5321973	0.51328	656.61	670.73	
71	126.0838379	0.551458	684.85	698.70	700
72	115.4316699	0.589317	712.56	726.07	
73	104.7131055	0.626559	739.57	752.67	750
74	94.05222656	0.662934	765.77	778.40	775
75	83.5625293	0.698224	791.04	803.16	800
76	73.35164551	0.732224	815.28	826.81	825
77	63.53920898	0.764679	838.35	849.25	850
78	54.22802734	0.795385	860.15	870.38	875
79	45.5021582	0.824185	880.61	890.13	
80	37.43464355	0.85095	899.66	908.44	900
81	30.10146973	0.875518	917.22	925.22	925
82	23.56202637	0.897767	933.22	940.44	
83	17.84854614	0.917651	947.66	954.09	950
84	12.97656128	0.935157	960.52	966.17	
85	8.95193542	0.950274	971.82	976.67	975
86	5.76314148	0.963007	981.53	985.63	
87	3.36772369	0.973466	989.73	993.30	
88	1.62043427	0.982238	996.87	999.84	1000
89	0.54208336	0.989153	1002.80	1005.12	
90	0.06575628	0.994204	1007.44	1009.15	
91	0.0000316	0.99763	1010.85	1012.05	
	0	1	1013.25		

1932

1933

1934

1935

3) JRA-25/JCDAS

JRA-25 used a hybrid sigma-pressure (hybrid $\sigma-p$) vertical coordinate after Simmons and Burridge (1981). The pressure on each level is calculated as $p_k = A_k + B_k \times p_{\text{srf}}$, where p_{srf} is surface pressure. The following table provides example pressures at layer interfaces ($k-1/2$) and layer midpoints (k) for a surface pressure of 1013.25 hPa, from TOA to surface.

Pressures at layer midpoints are defined as the average of pressures at layer interfaces.

k	Model Levels			Pressure Levels	
	$A_{k-1/2}$ (hPa)	$B_{k-1/2}$	$p_{k-1/2}$ (hPa)	p_k (hPa)	p (hPa)
1	0.000000	0.000000	0.00	0.40	0.4
2	0.800000	0.000000	0.80	1.13	1
3	1.460000	0.000000	1.46	2.01	2
4	2.560000	0.000000	2.56	3.45	3
5	4.330000	0.000000	4.33	5.72	5
6	7.100000	0.000000	7.10	9.15	7
7	11.200000	0.000000	11.20	14.10	10

8	17.000000	0.000000	17.00	21.00	20
9	25.000000	0.000000	25.00	30.15	30
10	35.299999	0.000000	35.30	41.70	
11	48.099998	0.000000	48.10	55.55	50
12	62.634430	0.000366	63.01	71.53	70
13	76.105057	0.003895	80.05	89.60	
14	88.363998	0.010636	99.14	109.71	100
15	98.876595	0.021123	120.28	131.88	
16	107.299492	0.035701	143.47	156.10	150
17	113.447090	0.054553	168.72	182.38	
18	117.259979	0.077740	196.03	210.71	200
19	118.777374	0.105223	225.39	241.10	250
20	118.113609	0.136886	256.81	273.55	
21	115.438545	0.172561	290.29	308.05	300
22	110.961449	0.212039	325.81	344.09	
23	105.094887	0.253905	362.36	381.16	
24	98.151306	0.297849	399.95	419.76	400
25	90.192863	0.344807	439.57	460.40	
26	81.437820	0.394562	481.23	502.57	500
27	72.323532	0.445676	523.90	545.75	
28	63.056015	0.497944	567.60	589.95	600
29	53.811684	0.551188	612.30	635.16	
30	44.741348	0.605259	658.02	680.87	700
31	36.158020	0.658842	703.73	726.58	
32	28.130577	0.711869	749.43	771.77	
33	20.862747	0.763137	794.11	815.43	
34	14.485500	0.811514	836.75	856.55	850
35	9.064261	0.855936	876.34	894.10	
36	4.611954	0.895388	911.86	932.15	925
37	1.105610	0.938894	952.44	960.05	
38	0.000000	0.955000	967.65	977.79	
39	0.000000	0.975000	987.92	995.52	1000
40	0.000000	0.990000	1003.12	1008.18	
	0.000000	1.000000	1013.25		

1941

1942

1943

1944

4) JRA-55

JRA-55 uses a hybrid sigma–pressure (hybrid $\sigma-p$) vertical coordinate after Simmons and Burridge (1981). The pressure on each level is calculated as $p_k = A_k + B_k \times p_{\text{srf}}$, where p_{srf} is surface pressure. The following table provides example pressures at layer interfaces ($k-1/2$) and layer midpoints (k) for a surface pressure of 1013.25 hPa, from TOA to surface.

Pressures at layer midpoints are defined as the average of pressures at layer interfaces.

k	Model Levels			p_k (hPa)	Pressure Levels p (hPa)
	$A_{k-1/2}$ (hPa)	$B_{k-1/2}$ (hPa)	$p_{k-1/2}$ (hPa)		
1	0.000000	0.000000	0.00	0.10	
2	0.200000	0.000000	0.20	0.30	
3	0.390000	0.000000	0.39	0.52	
4	0.650000	0.000000	0.65	0.81	
5	0.970000	0.000000	0.97	1.17	1
6	1.360000	0.000000	1.36	1.59	
7	1.820000	0.000000	1.82	2.10	2
8	2.370000	0.000000	2.37	2.69	
9	3.010000	0.000000	3.01	3.39	3
10	3.770000	0.000000	3.77	4.23	
11	4.690000	0.000000	4.69	5.25	5
12	5.810000	0.000000	5.81	6.51	7
13	7.200000	0.000000	7.20	8.07	
14	8.930000	0.000000	8.93	9.99	10
15	11.050000	0.000000	11.05	12.38	
16	13.700000	0.000000	13.70	15.35	
17	17.000000	0.000000	17.00	19.03	20
18	21.050000	0.000000	21.05	23.58	
19	26.100000	0.000000	26.10	29.20	30
20	32.300000	0.000000	32.30	36.15	
21	40.000000	0.000000	40.00	44.75	
22	49.500000	0.000000	49.50	55.25	50

23	60.886730	0.000113	61.00	67.77	70
24	72.015690	0.002484	74.53	81.81	
25	82.262449	0.006738	89.09	97.13	100
26	91.672470	0.013328	105.18	114.24	
27	100.146151	0.022854	123.30	133.39	125
28	107.299494	0.035701	143.47	154.58	150
29	112.854041	0.052146	165.69	177.82	175
30	116.633554	0.072366	189.96	203.12	200
31	118.554343	0.096446	216.28	230.46	225
32	118.612531	0.124387	244.65	259.35	250
33	116.953716	0.155046	274.05	289.78	300
34	113.696478	0.189304	305.51	321.75	
35	109.126384	0.225874	337.99	355.26	350
36	103.294362	0.265706	372.52	390.30	400
37	96.561819	0.307438	408.07	426.36	
38	89.140822	0.350859	444.65	463.45	450
39	81.221598	0.395778	482.24	501.55	500
40	72.974699	0.442025	520.86	540.16	550
41	64.767182	0.488233	559.47	578.77	
42	56.718242	0.534282	598.08	617.38	600
43	48.918808	0.580081	636.69	655.48	650
44	41.629564	0.62437	674.27	693.06	700
45	34.688715	0.668311	711.85	729.63	750
46	28.474848	0.709525	747.40	764.16	775
47	22.948417	0.748052	780.91	797.16	800
48	17.909074	0.785091	813.40	828.63	825
49	13.4768	0.819523	843.86	858.07	850
50	9.597972	0.851402	872.28	884.97	875
51	6.346027	0.879654	897.66	908.82	900
52	3.649041	0.904351	919.98	930.13	925
53	1.33051	0.926669	940.28	949.41	950
54	0	0.946	958.53	965.63	
55	0	0.96	972.72	978.80	975
56	0	0.972	984.88	989.95	
57	0	0.982	995.01	998.56	1000
58	0	0.989	1002.10	1004.64	
59	0	0.994	1007.17	1008.69	
60	0	0.997	1010.21	1011.73	
61	0	1	1013.25		

1950

1951

1952

1953 5) MERRA and MERRA-2

1954 MERRA and MERRA-2 use identical hybrid sigma–pressure (hybrid $\sigma-p$) vertical
 1955 coordinates after Simmons and Burridge (1981). The pressure on each level is calculated as
 1956 $p_k = A_k + B_k \times p_{\text{srf}}$, where p_{srf} is surface pressure. The following table provides example
 1957 pressures at layer midpoints (k) for a surface pressure of 1013.25 hPa, from TOA to surface.
 1958 Pressures at layer midpoints are defined as the average of pressures at layer interfaces.
 1959 NASA GMAO is transitioning away from this vertical grid and recommends that data users
 1960 use the three-dimensional pressure fields provided with MERRA and MERRA-2 instead.

k	Model Levels			Pressure Levels p (hPa)
	A_k (hPa)	B_k	p_k (hPa)	
1	0.0100	0	0.01	
2	0.0200	0	0.02	
3	0.0327	0	0.03	
4	0.0476	0	0.05	
5	0.0660	0	0.07	
6	0.0893	0	0.09	0.1
7	0.1197	0	0.12	
8	0.1595	0	0.16	
9	0.2113	0	0.21	
10	0.2785	0	0.28	0.3
11	0.3650	0	0.37	0.4
12	0.4758	0	0.48	0.5
13	0.6168	0	0.62	0.7
14	0.7951	0	0.80	
15	1.0194	0	1.02	1

16	1.3005	0	1.30	
17	1.6508	0	1.65	
18	2.0850	0	2.08	2
19	2.6202	0	2.62	
20	3.2764	0	3.28	3
21	4.0766	0	4.08	4
22	5.0468	0	5.05	5
23	6.2168	0	6.22	
24	7.6198	0	7.62	7
25	9.2929	0	9.29	10
26	11.2769	0	11.28	
27	13.6434	0	13.64	
28	16.4571	0	16.46	
29	19.7916	0	19.79	20
30	23.7304	0	23.73	
31	28.3678	0	28.37	30
32	33.8100	0	33.81	
33	40.1754	0	40.18	40
34	47.6439	0	47.64	50
35	56.3879	0	56.39	
36	66.6034	0	66.60	70
37	78.5123	0	78.51	
38	92.3657	0	92.37	100
39	108.6630	0	108.66	
40	127.8370	0	127.84	
41	150.3930	0	150.39	150
42	176.9300	0	176.93	
43	201.1920	0.006960	208.24	200
44	216.8650	0.028010	245.25	250
45	224.3630	0.063720	288.93	300
46	223.8980	0.113602	339.01	350
47	218.7760	0.156224	377.07	
48	212.1500	0.200350	415.15	400
49	203.2590	0.246741	453.27	450
50	193.0970	0.294403	491.40	500
51	181.6190	0.343381	529.55	
52	169.6090	0.392891	567.71	550
53	156.2600	0.443740	605.88	600
54	142.9100	0.494590	644.05	650
55	128.6960	0.546304	682.24	
56	118.9590	0.581041	707.70	700
57	109.1820	0.615818	733.16	725
58	99.3652	0.650635	758.62	750
59	89.0999	0.685900	784.09	775
60	78.8342	0.721166	809.56	800
61	70.6220	0.749378	829.93	825
62	64.3626	0.770637	845.21	850
63	58.0532	0.791947	860.49	
64	51.6961	0.813304	875.78	875
65	45.3390	0.834661	891.06	
66	38.9820	0.856018	906.34	900
67	32.5708	0.877429	921.63	925
68	26.0920	0.898908	936.91	
69	19.6131	0.920387	952.20	950
70	13.1348	0.941865	967.48	
71	6.5938	0.963406	982.76	975
72	0.0480	0.984952	998.05	1000
	0	1	1013.25	

1961

1962

1963

1964

6) NCEP-NCAR R1 and NCEP-DOE R2

NCEP-NCAR R1 and NCEP-DOE R2 use a sigma vertical coordinate. The pressure on each level is calculated as $p_k = \sigma_k \times p_{\text{srf}}$, where p_{srf} is surface pressure. The following table provides example pressures at each level for a surface pressure of 1013.25 hPa, from TOA to surface.

k	Model Levels		Pressure Levels p (hPa)
	σ_k	p_k (hPa)	
1	0.00273	2.77	3

2	0.01006	10.19	10
3	0.01834	18.58	20
4	0.02875	29.13	30
5	0.04179	42.34	
6	0.05805	58.82	50
7	0.07815	79.19	70
8	0.10278	104.14	100
9	0.13261	134.37	
10	0.16823	170.46	150
11	0.21006	212.84	200
12	0.25823	261.65	250
13	0.31248	316.62	300
14	0.37205	376.98	400
15	0.43568	441.45	
16	0.50168	508.33	500
17	0.56809	575.62	
18	0.63290	641.29	
19	0.69426	703.46	700
20	0.75076	760.71	
21	0.80142	812.04	
22	0.84579	857.00	850
23	0.88384	895.55	
24	0.91592	928.06	925
25	0.94255	955.04	
26	0.96437	977.15	
27	0.98208	995.09	
28	0.99500	1008.18	1000
29	1.00000	1013.25	

1968

1969

1970

1971

7) CFSR

1972 CFSR uses a hybrid sigma–pressure (hybrid σ – p) vertical coordinate after Simmons and
 1973 Burridge (1981). The pressure on each level is calculated as $p_k = A_k + B_k \times p_{\text{sr}}$, where p_{sr} is
 1974 surface pressure. The following table provides example pressures at layer interfaces ($k-1/2$)
 1975 and layer midpoints (k) for a surface pressure of 1013.25 hPa, from TOA to surface.
 1976 Pressures at layer midpoints are defined as the average of pressures at layer interfaces.

k	Model Levels				Pressure Levels p (hPa)
	$A_{k-1/2}$ (hPa)	$B_{k-1/2}$	$p_{k-1/2}$ (hPa)	p_k (hPa)	
1	0.00000	0.000000	0.00	0.32	
2	0.64247	0.000000	0.64	1.01	1
3	1.37790	0.000000	1.38	1.80	2
4	2.21958	0.000000	2.22	2.70	3
5	3.18266	0.000000	3.18	3.73	
6	4.28434	0.000000	4.28	4.91	5
7	5.54424	0.000000	5.54	6.26	
8	6.98457	0.000000	6.98	7.81	7
9	8.63058	0.000000	8.63	9.57	10
10	10.51080	0.000000	10.51	11.58	
11	12.65752	0.000000	12.66	13.88	
12	15.10711	0.000000	15.11	16.50	
13	17.90051	0.000000	17.90	19.49	20
14	21.08366	0.000000	21.08	22.90	
15	24.70788	0.000000	24.71	26.77	
16	28.83038	0.000000	28.83	31.17	30
17	33.51460	0.000000	33.51	36.17	
18	38.83052	0.000000	38.83	41.84	
19	44.85493	0.000000	44.85	48.26	50
20	51.67146	0.000000	51.67	55.52	
21	59.37050	0.000000	59.37	63.71	
22	68.04874	0.000000	68.05	72.93	70
23	77.77150	0.000037	77.81	83.29	
24	88.32537	0.000431	88.76	94.89	100
25	99.36614	0.001636	101.02	107.87	
26	110.54853	0.004107	114.71	122.32	125
27	121.52937	0.008294	129.93	138.37	
28	131.97065	0.014637	146.80	156.11	150

29	141.54316	0.023556	165.41	175.63	175
30	149.93074	0.035442	185.84	197.00	200
31	156.83489	0.050647	208.15	220.26	225
32	161.97967	0.069475	232.37	245.44	250
33	165.11736	0.092167	258.51	272.50	
34	166.11603	0.118812	286.50	301.39	300
35	165.03144	0.149269	316.28	331.99	
36	161.97315	0.183296	347.70	364.14	350
37	157.08893	0.220570	380.58	397.64	400
38	150.56342	0.260685	414.70	432.25	
39	142.61435	0.303164	449.80	467.68	450
40	133.48671	0.347468	485.56	503.61	500
41	123.44490	0.393018	521.67	539.73	550
42	112.76348	0.439211	557.79	575.69	
43	101.71712	0.485443	593.59	611.17	600
44	90.57051	0.531135	628.74	645.84	650
45	79.56908	0.575747	662.94	679.44	
46	68.93117	0.618800	695.93	711.70	700
47	58.84206	0.659887	727.47	742.43	750
48	49.45029	0.698683	757.39	771.47	775
49	40.86614	0.734945	785.55	798.70	800
50	33.16217	0.768515	811.86	824.07	825
51	26.37553	0.799310	836.28	847.53	850
52	20.51150	0.827319	858.79	869.11	875
53	15.54789	0.852591	879.44	888.85	
54	11.43988	0.875224	898.26	906.80	900
55	8.12489	0.895355	915.34	923.06	925
56	5.52720	0.913151	930.78	937.72	
57	3.56223	0.928797	944.67	950.89	950
58	2.14015	0.942491	957.12	962.68	
59	1.16899	0.954434	968.25	973.21	975
60	0.55712	0.964828	978.17	982.58	
61	0.21516	0.973868	986.99	990.90	
62	0.05741	0.981742	994.81	998.27	1000
63	0.00575	0.988627	1001.73	1004.79	
64	0.00000	0.994671	1007.85	1010.55	
	0.00000	1.000000	1013.25		

1977

1978

1979

1980 8) NOAA-CIRES 20CR v2

The 20CR uses a hybrid sigma–pressure (hybrid σ – p) vertical coordinate after Simmons and Burridge (1981). The pressure on each level is calculated as $p_k = A_k + B_k \times p_{\text{srf}}$, where p_{srf} is surface pressure. The following table provides example pressures at layer interfaces ($k-1/2$) and layer midpoints (k) for a surface pressure of 1013.25 hPa, from TOA to surface.

Pressures at layer midpoints are defined as the average of pressures at layer interfaces.

k	Model Levels			Pressure Levels	
	$A_{k-1/2}$ (hPa)	$B_{k-1/2}$	$p_{k-1/2}$ (hPa)	p_k (hPa)	p (hPa)
1	0.00000	0.000000	0.00	2.83	
2	5.66898	0.000000	5.67	9.29	10
3	12.90533	0.000000	12.91	17.51	20
4	22.10979	0.000000	22.11	27.94	30
5	33.76516	0.000000	33.77	41.10	
6	48.44036	0.000000	48.44	57.61	50
7	66.78608	0.000000	66.79	78.15	70
8	89.13767	0.000379	89.52	103.47	100
9	113.43654	0.003933	117.42	134.33	150
10	136.71427	0.014326	151.23	171.39	
11	156.13564	0.034950	191.55	215.13	200
12	169.12130	0.068675	238.71	265.66	250
13	173.64658	0.117418	292.62	322.64	300,350
14	169.59994	0.180667	352.66	385.13	400
15	158.12926	0.256084	417.61	451.65	450
16	140.89535	0.340293	485.70	520.25	500,550
17	119.91428	0.429195	554.80	588.72	600
18	97.31807	0.518457	622.64	654.89	650
19	75.08532	0.604055	687.14	716.87	700

S-RIP 2015 Report: CHAPTER 2, DRAFT (28 November 2016)

20	54.81144	0.682747	746.60	773.25	750
21	37.57142	0.752347	799.89	823.16	800
22	23.89205	0.811785	846.43	866.32	850
23	13.81526	0.860975	886.20	902.86	900
24	7.01453	0.900581	919.53	933.27	
25	2.92577	0.931750	947.02	958.21	950
26	0.86457	0.955872	969.40	978.42	
27	0.11635	0.974402	987.43	994.63	1000
28	0.00009	0.988726	1001.83	1007.54	
	0.00000	1.000000	1013.25		

1986
1987

Filename: S-RIP.Chapter02_201610.docx
Folder: /Users/jswright/Library/Containers/com.microsoft.Word/Data/Documents
Template: /Users/jswright/Library/Group Containers/UBF8T346G9.Office/User
Content.localized/Templates.localized/Normal.dotm
Title:
Subject:
Author: Jonathon Wright
Keywords:
Comments:
Creation Date: 11/29/16 4:07:00 PM
Change Number: 2
Last Saved On: 11/29/16 4:07:00 PM
Last Saved By: Jonathon Wright
Total Editing Time: 0 Minutes
Last Printed On: 11/29/16 4:07:00 PM
As of Last Complete Printing
Number of Pages: 88
Number of Words: 31,505
Number of Characters: 178,882 (approx.)